INFORMATION TO USERS

This manuscript has been reproduced from the microfilm master. UMI films the text directly from the original or copy submitted. Thus, some thesis and dissertation copies are in typewriter face, while others may be from any type of computer printer.

The quality of this reproduction is dependent upon the quality of the copy submitted. Broken or indistinct print, colored or poor quality illustrations and photographs, print bleedthrough, substandard margins, and improper alignment can adversely affect reproduction.

In the unlikely event that the author did not send UMI a complete manuscript and there are missing pages, these will be noted. Also, if unauthorized copyright material had to be removed, a note will indicate the deletion.

Oversize materials (e.g., maps, drawings, charts) are reproduced by sectioning the original, beginning at the upper left-hand corner and continuing from left to right in equal sections with small overlaps. Each original is also photographed in one exposure and is included in reduced form at the back of the book.

Photographs included in the original manuscript have been reproduced xerographically in this copy. Higher quality 6" x 9" black and white photographic prints are available for any photographs or illustrations appearing in this copy for an additional charge. Contact UMI directly to order.

UMI

A Bell & Howell Information Company
300 North Zeeb Road, Ann Arbor MI 48106-1346 USA
313/761-4700 800/521-0600

Nonlinear Optical Spectroscopy and Microscopy of Model Random and Biological Media

By

Yici Guo

A dissertation submitted to the Graduate Faculty in Engineering in partial fulfillment of the requirements for the degree of Doctor of Philosophy, the City University of New York.

—1998—

This manuscript has been read and accepted for the Graduate Faculty in Engineering in satisfaction of the dissertation requirement for the degree of Doctor in Philosophy.

9/9/98
Date:

Chairman of the Examining Committee:
Dr. Robert R. Alfano, Distinguished Professor of Science and Engineering, Departments of Physics and Electrical Engineering,
The City College of The City University of New York.

9/9/98
Date:

Co-Chairman of the Examining Committee:
Dr. P. P. Ho, Professor, Department of Electrical Engineering,
The City College of The City University of New York.

9/14/98
Date:

Executive Officer:
Professor G. G. Lowen

Dr. H. E. Savage, Professor, New York Eye and Ear Infirmary.

Dr. Kai Shum, Professor, Department of Electrical Engineering, The City College of The City University of New York.

Dr. M. L. Steinberg, Professor, Department of Chemistry, The City College of The City University of New York.

Supervisory Committee

The City University of New York

Abstract

Nonlinear Optical Spectroscopy and Microscopy of Model Random and Biological Media

By

Yici Guo

Advisor: Professor R. R. Alfano

Co-Advisor: Professor P. P. Ho

Nonlinear optical (NLO) spectroscopy and microscopy applied to biomedical science are emerging as new and rapidly growing areas which offer important insight into basic phenomena. Ultrafast NLO processes provide temporal, spectral and spatial sensitivities complementary or superior to those achieved through conventional linear optical approaches. The goal of this thesis is to explore the potential of two fundamental NLO processes to produce noninvasive histological maps of biological tissues. Within the goal of the thesis, steady state intensity, polarization and angular measurements of second- and third- harmonic generations (SHG, THG) have been performed on model random scattering and animal tissue samples. The nonlinear optical effects have been evaluated using models. Conversion efficiencies of SHG and THG from animal tissue interfaces have been determined, ranging from 10^{-7} to 10^{-10}. The changes in the multiharmonic signals were found to depend on both local and overall histological structures of biological samples. The spectral signatures of two photon excitation induced fluorescence from intrinsic fluorophores have been acquired

and used to characterize the physical state and types of tissues. Two dimensional scanning SHG and TPF tomographic images have been obtained from *in vitro* animal tissues, normal and diseased human breast tissues, and resolved subsurface layers and histo-chemical distributions. By combining consecutive 2D maps, a 3D image can be produced. The structure and morphology dependence of the SH signal has been utilized to image and evaluate subsurface tumor progression depth. Second harmonic microscopy in model random and biological cells has been studied using a CCD camera to obtain direct images from subcellular structures. Finally, near infrared (NIR) NLO spectroscopy and microscopy based on SHG and TPF have demonstrated high spatial resolution, deeper penetration depth, low level photo-damaging and enhanced morphological sensitivity for the noninvasive characterization and visualization of biological systems. NIR radiation used in the NLO techniques offers a deeper penetration depth and low level photo-damage as compared with the conventional single photon excitation.

To my parents Hui Ying Yao and Zong Shan Guo

Acknowledgments

I would like to acknowledge my deep appreciation for the constant teaching, guidance and counsel of Professor Robert R. Alfano and Professor Ping Pei Ho during the course of this thesis work. I wish to thank Professor R. R. Alfano for giving me the opportunity to carry out and complete my thesis research. I thank him for bombarding me with new and exciting ideas. His sharp vision and broad knowledge in nonlinear optics, biophotonics and laser physics are the stimuli in this thesis work, resulting in most of the encouraging progress. I feel much gratitude towards Professor P. P. Ho for his guidance in defining my thesis topic and many discussions. I also wish to thank Dr. H. E. Savage of New York Eye and Ear Infirmary, Professor Kai Shum of Electrical Engineering Department, and Professor Mark L. Steinberg of Chemistry Department for serving on the supervisory committee. I wish to thank Dr. H. E. Savage for his expert contribution in sample preparation, histology, and interpretation of results to produce publications. Special thanks go to Professor M. L. Steinberg, Dr. P. G. Sacks, Mr. D. Harris and Professor R. Zuzolo for their valuable collaboration and supply of samples. I would like also to express my gratitude to the members of the Institute for Ultrafast Spectroscopy and Lasers; particularly, Dr. Feng Liu and Dr. Quan Zhen Wang for their great help in laser systems and experimental details. I thank Dr. N. Zhadin, Dr. L. Wang, Dr. S. K. Gayen, Dr. A. Katz, Dr. B. Xu and Ms. Liang for their help and discussions. The financial support of the Air Force Office of Scientific Research, New York State Science and Technology Foundation, and Mediscience Technology Corp. is also gratefully acknowledged.

I am deeply indebted to my family, my parents, my husband Bo and daughter Jennifer. I thank them for always being a source of deep understanding and strong support. This work is dedicated to them - for their love, patience and encouragement.

Table of Contents

List of Figures

List of Tables

Chapter 1

Introduction

1.1 Background

When a tissue is subjected to radiation of ultrashort laser pulses at single or multiple wavelengths, nonlinear optical phenomena can be observed in the post-interaction-generated light emissions. New frequency components, along with altered temporal and spatial profiles varying as functions of the incident light intensity are among the nonlinear phenomena that have been observed and studied. The underlying mechanism for generating these intensity-dependent light-wave features is the material's nonlinearity. The intense radiation from laser sources is powerful enough to perturb the electronic and vibrational configuration of the individual molecules inside the tissue medium. In response, the medium generates a series of polarization terms scaled in square, cubic, fourth and fifth powers with the applied electric field, resulting in nonlinear (higher than a linear proportion) contributions. Nonlinear polarization is the key element that relates the incident and generated light waves. It also forms the underlying physics of creating new frequencies, stimulated light scattering, wave-wave and wave-medium energy exchange, induced modulation on the index of refraction and many other nonlinear interactions. The diversity of the NLO phenomena have triggered intensive studies in solid state, liquid and gaseous materials mainly for the purpose of generating and controlling the properties of the outgoing waves from NLO materials.[1-3] Special efforts have also focused on utilizing NLO properties to study basic structure of matter, excitation and relaxation processes that occur on an ultrafast time

scale.[4-6] Many experimental techniques based on NLO effects have become standard probing methods, providing new or complementary information, high sensitivity and resolution, as well as novelty and potential applications in many scientific fields.[7,8]

This thesis focuses on optical multiharmonic generation (MHG) and two photon excitation of fluorescence in random scattering and biological media for forming subsurface histology maps. Being an unique category of matter-state, biological organelle, cell and tissue systems have not received widespread attention as targets for NLO studies. The nonlinear optical effects in these media have not been thoroughly treated and well understood when compared with the fully developed theories and experiments in other homogeneous materials. Investigations on purified biological molecules, in the nonlinear optical regime, have been successful in revealing structural and functional related characteristics of chromophores.[9,10] In these studies, the environmental effect, the interplay between structures, the variations of chemical composition and light scattering are absent or neglected. Actual biological tissues and organs are far more complex than synthesized models, where the low concentration and inhomogeneity of the target components impose difficulties in signal detection, data processing and interpretation of results.

The first investigation of optical harmonic generation in biological tissues began back two decades ago. In 1971, Fine and Hansen[11] first observed the phenomenon of second harmonic generation from a number of native collageneous tissues. Ultraviolet radiation was observed at twice the ruby laser frequency from the irradiated tissue samples. The harmonic emission was confirmed by its spectrum and temporal narrowing in the generated pulses. In 1978, Sheppard *et al.* proposed various types of scanning SH microscope and suggested their applications in biological studies.[12] Freund and Roth employed a transmission SHG microscopy in a rat-tail tendon system in

1981 and 1986 to clarify whether the polarity of connective tissue is structural or functional.[13,14] A variant of the same method was used by Bouevitch *et al.* in a reflection geometry to probe membrane potential changes in a dye-stained lipid bilayer.[15] A well defined correlation between SHG signal and membrane potential was observed. In 1990, Denk, Strickler and Webb demonstrated the first fluorescence image by using two photon excitation in biological samples.[16] Since then multi-photon microscopy has been recognized as a technique with improved penetration depth, less photo-toxity and inherent capability for optical sectioning.[17-19] In 1995, Piston and his co-workers achieved 3-D images of cellular metabolism in rabbit cornea through TPF of pyridine nucleotide with sub-micron lateral resolution.[19] Using the Z scan method, the third order nonlinear optical susceptibility $\chi^{(3)}$ (n_2) of human and rabbit vitreous humors was determined by Rockwell and coworkers.[20] More recently, TPF imaging of NAD(P)H was used to study metabolic state of *in vivo* human skin by Masters *et al.*[21] Three-photon fluorescence imaging of tryptophan and serotonin was demonstrated by Maiti and his co-workers from *in vitro* rat cell cultures.[22]

Since 1968, theoretical and experimental investigations have been conducted on optical harmonic generation in discrete model random medium. Kurtz and Perry studied SHG in various inorganic and organic crystalline powders.[23] The dependence of SH intensity $I(2\omega)$ on the average particle size was used to determine the phase-match ability and magnitude of second order nonlinear optical susceptibility $\chi^{(2)}$ tensor components. Agranovich theoretically calculated the weak localization effect in both linear and nonlinear regimes.[24] The spatial profile of the reflected SH wave from the discrete model random medium was predicted to be sensitive to the Anderson localization effect and the spatial structure of the incident field. Yoo and his colleagues experimentally studied the coherent interference between the scattered SH light and its

time reversed components in KH_2PO_4 (KDP) powders.[25] The negative result of observing the weak localization in the nonlinear regime indicated the basic and subtle differences between the linear and nonlinear optical processes that coexist in the random medium.

The connection between discrete random media and biological tissues is related in terms of their optical properties. On a macroscopic scale, both materials are disordered, and the changes in the index of refraction cause light to undergo multiple random scattering. On a microscopic scale, tissue specimens are often comprised of multiple constituents which give rise to heterogeneous responses. The continuous variation of the index of refraction strongly affects the temporal, spectral and spatial properties of light propagation in the system under study. This indicates the importance of incorporating both scattering and absorption effects in accessing and evaluating nonlinear optical properties in random media.

The initial NLO biomedical studies opened opportunities for many spectroscopy and imaging applications. Experimental and theoretical research conducted to date is mainly confined to multiphoton excited fluorescence processes. Second harmonic generation has been only studied in isolated transparent tissues. The symmetry dependence and interfacial sensitivities of SHG and surface SHG have not been explored in scattering media. Harmonic generation higher than the second order has not been reported. There exists a lack of SHG imaging applications in view of its structural sensitivities. This thesis is devoted to the advancement in NLO biomedical spectroscopy and imaging. The research emphasizes on second harmonic tomography for generating noninvasive histological maps to detect cancer.

1.2 Significance of Nonlinear Optical Studies in Biological Materials

The significance of NLO studies in biological tissues and cells arises from the following considerations:

(1) NLO processes offer sensitivities superior to conventional linear optical approaches for a better characterization of biological systems. In second harmonic generation, molecular orientation and symmetry sensitivities can be utilized to probe the morphological changes of microscopic structures. The coherent property of MHG may provide direct correlation with phase, intensity, direction and polarization changes of the light wave. In a two photon absorption process, different selection rule associated with parity concern allows one to probe a transition that is not accessible in a single-photon event. High spatial resolution and intrinsic optical sectioning capability can be achieved based on the quadratic intensity dependence of the NLO signals on the incident intensity. These features suggest potentials in various biomedical imaging and diagnostic applications.

(2) NLO techniques may gain advantages through the excitation processes. Multi-photon excitation eliminates UV illumination by using laser pulses in the visible to near infrared (NIR) spectral range. Light at longer wavelengths generates less scattering and absorption, thus penetrating deeper into the tissue. It is also known that visible or infrared light produces less photo bleaching and damage than UV light, thereby permitting one to achieve high discrimination against background signal from off-focus planes in image formation. The dependence of the NLO signal on a higher order of

the index of refraction allows one to obtain enhanced optical contrast for highlighting small structural changes.

(3) NLO effects using NIR may render an alternative safety criterion. The intense radiation involved in laser surgery and ablation can generate UV and hard UV light through nonlinear optical interactions with tissues and organs when the fundamental wavelength is in the visible to NIR region. In this case, the nonlinear optical effect often happens involuntarily and the impact is generally concerned with safety related issues. It is important to determine and characterize NLO effects for establishing alternative safety parameters aimed for health protection.

(4) NLO tomography can provide noninvasive *in situ* histological and histochemical maps of tissues. NLO parameters may offer a variety of image contrast mechanisms in temporal, spectral and spatial domains to visualize and characterize tissues. Potential clinical applications include precancer and cancer detection in aero-digestive, gastrointestinal, and gynecological tracts.

1.3 Thesis Statement

My thesis is about the investigation of nonlinear optical spectroscopy and microscopy of model random and biological media. It studies and demonstrates the applications of two fundamental nonlinear optical processes in highly scattering model random and biological materials: *second and third harmonic generations* and *two photon excitation induced fluorescence*. The purpose is to establish novel, new and noninvasive spectroscopy and imaging modalities using nonlinear optical approaches. The thesis research consists of spectral and spatial domain investigations to acquire histological

and histo-chemical information about biological cells and tissues for the purpose of detecting cancer and other types of diseases.

The objectives of the thesis are:

(1) to determine SHG and THG from model random and biological tissues and cells.

In particular:

(i) to quantify optical second- and third- harmonic generations in model random scattering and biological media.

(ii) to examine the polarization dependence of second harmonic generation from random scattering media.

(iii) to investigate temporal, spectral and spatial properties of second harmonic signals in biological media.

(2) to determine two photon excitation induced fluorescence characteristics of model random fluorescent molecules, biological tissues, and cell line samples.

In particular:

(i) to obtain the steady state TPF emission spectra from various biological samples.

(ii) to evaluate single and two photon emission spectra for comparison with self absorption and scattering effects.

(3) to study SHG and TPF imaging techniques using laser scanning microscope and CCD camera in highly scattering biological materials for establishing new and noninvasive modalities to detect cancer and other diseases.

In particular:

(i) to obtain two dimensional second harmonic tomographic images in layered biological structures such as skin, fascia, and other mucosal tissues.

(ii) to obtain two dimensional TPF imaging map of intrinsic fluorophore distributions in animal tissues.

(iii) to obtain direct reflection SHG image of internal structures in biological cells using CCD camera.

(4) to investigate the feasibility of using SHG and TPF imaging techniques for medical diagnosis of cancer and other diseases.

1.4 Thesis Organization

This thesis is organized into eight chapters. Chapter one provides a brief and basic review of NLO processes and NLO research history in random and biological systems. The significance of the study and the research goal are also stated.

In chapter two, a theoretical review of optical second harmonic generation in homogenous and random scattering media is given. The nonlinear wave equation is presented to explain the physical origin of the NLO process of optical harmonic generations. Scattering effect is discussed within the framework of nonlinear optics and light transportation theory to describe NLO wave propagation in random medium.

Chapter three describes the measurements of second and third harmonic generations in modal random media and biological tissues. Experimental results of studies in steady state intensity, spectral and spatial properties of second harmonic generation in biological tissues are given.

Chapter four covers a theoretical review of two photon absorption and two photon excitation of fluorescence spectroscopy in biological media. Experimental TPF measurements of steady state intensity and spectral responses from intrinsic fluorophore in biological tissues and microcrystal fluorescent molecules are given.

Chapter five will demonstrate second harmonic tomography in different biological structures. The initial results of NLO spectroscopy imaging in normal and

diseased human breast tissues and carcinogen treated hamster cheek pouch tissues will be presented. The feasibility of using SHG and TPF in medical diagnosis of cancer and other diseases is discussed.

Chapter six studies second harmonic microscopy using the CCD camera based direct imaging technique. Backscattered second harmonic images from modeled microscopic objects and substructures in biological cells are presented and compared with linear optical images.

Chapter seven focuses on two photon excitation of fluorescence imaging of tryptophan distribution in biological tissues. Subsurface histochemical maps of TPF of tryptophan are demonstrated.

Chapter eight states a number of future directions in NLO spectroscopy and microscopy of biological media and condensed matter. The research will focus on clinical testing of noninvasive NLO techniques to detect disease in tissue, and failure analysis using multiphoton microscopy in semiconductor miniature devices.

References

1. P. A. Franken, A. E. Hill, C. W. Peters, and G. Weinreich, Phys. Rev. Lett. **7**, 118 (1961).
2. N. Bloembergen, J. Ducuining, and P. S. Pershan, Phys. Rev. **127**, 1918 (1962).
3. J. A. Giordmaine, Scientific American **210**, 38 (1964).
4. For a general review on the theory and application of nonlinear optics, see Y. R. Shen, "*Principles of Nonlinear Optics*", John Wiley and Sons (1984), and the references therein.
5. M. D. Levenson and N. Bloembergen, J. Chem. Phys. **60**, 1323 (1974).
6. J. L. Oudar and Y. R. Shen, Phys. Rev. A **22**, 1141 (1980).
7. R. Hellwarth and P. Christiansen, Opt. Comm. **12**, 318 (1974).
8. P. D. Maker and R. W. Terhune, Phys. Rev. B **6**, 534 (1972).
9. J. Haung and A. Lewis, Biophys. J. **55**, 835 (1989).
10. J. Huang, Z. Chen, and A. Lewis, J. Phys. Chem. **93**, 3314 (1989).
11. S. Fine and W. P. Hansen, Appl. Opt. **10**, 2350 (1971).
12. J. Gannaway and C. J. R. Sheppard, Opt. & Quant. Elect. **10**, 435 (1978).
13. S. Roth and I. Freund, Biopolymers, **20**, 1271 (1981).
14. I. Freund, M. Deutsch, and A. Sprecher, Biophys. J. **50**, 693 (1986).
15. O. Bouevitch, A. Lewis, I. Pinevsky, J. P. Wuskell, and L. M. Loew, Biophys. J. **65**, 672 (1993).
16. W. Denk, J. H. Strickler, and W. W. Webb, Science **248**, 73 (1990).
17. P. E. Hanninen, E. Soini, and S. W. Hell, J. Microsc. **176**, 222 (1994).
18. W. Denk, D. W. Piston, and W. W. Webb, "*Handbook of Biological Confocal Microscopy*", Plenum Press, New York (1995).

19. D. W. Piston, B. R. Masters, and W. W. Webb, J. of Microsrc. **178**, 20 (1995).

20. B. A. Rockwell, W. P. Roach, M. E. Rogers, M. W, Mayo, and C. A. Toth, Opt. Lett. **18,** 1792 (1993).

21. B. R. Masters, P. T. C. So, and E. Gratton, Biophys. J. **72**, 2405 (1997).

22. S. Maiti, J. B. Shear, R. M. Williams, W. R. Zipfel, and W. W. Webb, Science **275**, 530 (1997).

23. S. K. Kurtz and T. T. Perry, J. Appl. Phys. **39**, 3298 (1968).

24. V. E. Kravtsov, V. M. Agranovich, and K. I. Grigorishin, Phy. Rev. B, **44**, 4931 (1991).

25. K. M. Yoo, S. Lee, Y. Takiguchi, and R. R. Alfano, Opt. Lett. **14**, 800 (1989).

Chapter Two

Nonlinear Optics of Optical Harmonic Generation

2.1 The General Wave Equation

Light is a form of electromagnetic (EM) energy. The EM wave propagating inside a medium is governed by the Maxwell equations[1-3]:

$$\nabla \times \vec{E} = -\frac{\partial \vec{B}}{\partial t}, \tag{2.1a}$$

$$\nabla \times \vec{H} = \frac{\partial \vec{D}}{\partial t} + J, \tag{2.1b}$$

$$\nabla \cdot \vec{D} = \rho, \tag{2.1c}$$

$$\nabla \cdot \vec{H} = 0, \tag{2.1d}$$

where $\vec{E}(r,t)$ and $\vec{B}(r,t)$ are the electric and magnetic fields varying in the spatial and temporal coordinates in MKS units, respectively. $\vec{D}$ is the electric displacement, $\vec{J}$ is the electric current density, and $\vec{H}$ is the intensity of the magnetic field. The constitutive equations that describe the relationships between the above quantities are given by:

$$\vec{D} = \varepsilon\vec{E} = \varepsilon_0\vec{E} + \vec{P}, \tag{2.2a}$$

$$\vec{B} = \mu\vec{H}, \tag{2.2b}$$

$$\vec{J} = \sigma\vec{E}, \tag{2.2c}$$

$$\vec{P} = \varepsilon_0\chi E, \tag{2.2d}$$

where $\vec{P}$ is defined as the total polarization inside the material in linear optics. The parameters that relate $\vec{D}$ and $\vec{E}$, $\vec{B}$ and $\vec{H}$, $\vec{J}$ and $\vec{E}$, $\vec{P}$ and $\vec{E}$ are ε, σ, and χ tensor quantities, and are called the permittivity, conductivity and optical susceptibility tensors, respectively. They are all dispersive, i.e., frequency dependent, and are functions of the spatial coordinates. In nonlinear optical regime, i.e., under intense light radiation, the total polarization $\vec{P}$ inside the matter is no longer sufficiently described by a simple linear proportion to the $\vec{E}$ field. The proper expression is a power series expansion of the electric field:

$$\vec{P} = \varepsilon_0 \chi^{(1)} \vec{E} + \varepsilon_0 \chi^{(2)} \vec{E}\vec{E} + \varepsilon_0 \chi^{(3)} \vec{E}\vec{E}\vec{E} + \ldots \quad , \tag{2.3}$$

where ε_0 is the dielectric constant in vacuum, and $\chi^{(n)}$ (n=1,2,3...) are called the nth order optical susceptibility tensors.

A key element in nonlinear optics is nonlinear polarization, $\vec{P}^{NL}$. It consists of the higher order terms in Eq. (2.3):

$$\vec{P}^{NL} = \varepsilon_0 \chi^{(2)} \vec{E}\vec{E} + \varepsilon_0 \chi^{(3)} \vec{E}\vec{E}\vec{E} + \ldots \quad , \tag{2.4}$$

where $\chi^{(2)}$ and $\chi^{(3)}$ are the second and third order nonlinear optical susceptibilities and are the two lowest coefficients possessing relatively large responses. Throughout the entire thesis, $\chi^{(2)}$ and $\chi^{(3)}$ will be used repeatedly. $\chi^{(n)}$ is physically related to the microscopic structure of the medium and characterizes the nonlinear optical property. It is a quantity that bridges between the response from an infinitesimal small structure-unit such as a molecule and the macroscopic signal that we observe.

The quadratic and higher order dependence of $\vec{P}^{NL}$ on the electric field $\vec{E}$ explains the origin of the nonlinear optical phenomena. From Eq. (2.1a), a wave equation can be deduced to determine the electric field $\vec{E}$ varying as a dependent on the total polarization $\vec{P}$ in temporal and spatial coordinates. By vector operations,

$$\nabla \times \nabla \times \vec{E} = -\frac{\partial(\nabla \times \vec{B})}{\partial t} = -\mu_0 \frac{\partial(\nabla \times \vec{H})}{\partial t}$$

$$= -\mu_0 \frac{\partial^2 \vec{D}}{\partial t^2} - \mu_0 \frac{\partial \vec{J}}{\partial t} = -\mu_0 \frac{\partial^2 \vec{D}}{\partial t^2} - \mu_0 \sigma \frac{\partial \vec{E}}{\partial t} \qquad (2.5)$$

$$= -\mu_0 \varepsilon_0 \frac{\partial^2 \vec{E}}{\partial t^2} - \mu_0 \sigma \frac{\partial \vec{E}}{\partial t} - \mu_0 \frac{\partial^2 \vec{P}}{\partial t^2}$$

Based on Eq. (2.5), one can obtain a partial differential equation which is similar to the equation that describes a classical oscillator model under forced oscillation:

$$\nabla^2 \vec{E} = \mu_0 \sigma \frac{\partial \vec{E}}{\partial t} + \mu_0 \varepsilon_0 \frac{\partial^2 \vec{E}}{\partial t^2} + \mu_0 \frac{\partial^2 \vec{P}}{\partial t^2}. \qquad (2.6)$$

Equation (2.6) is the general wave equation inside a nonmagnetic and electric neutral medium. Similar to the classic model of the oscillator, this equation explains the source and response of nonlinear optical interactions. The first term on the right hand side represents a damping effect on the wave, whereas the third term represents the source of the excitation. This suggests that the total polarization provides the excitation, while the electric field generates the response as a consequence. Since the nonlinear effect is introduced from the total polarization $\vec{P}$, it ultimately determines the $\vec{E}$ field's behavior inside the medium. For a given polarization, a solution for the electric field can be found from Eq. (2.6).

2.2 Wave Equation for Nonlinear Optical Interaction

In order to quantitatively determine the field response, it is necessary to separately treat linear and nonlinear excitation components and take into account the individual contribution from each term in the total polarization. In this section, a further description of the wave equation incorporating nonlinear interaction between different optical waves will be given.

Many NLO phenomena arise from nonlinear coupling between optical waves inside a material. The EM energy carried by the interacting waves can be directly exchanged between each wave or transferred via the intervening medium. Both forms of energy exchange are assisted by the nonlinear optical susceptibilities $\chi^{(n)}$. As stated in section 2.1, the electric field $\vec{E}$ inside the medium is driven by the total polarization $\vec{P}$ which is further divided into a linear $\vec{P}^{L}$ and a nonlinear $\vec{P}^{NL}$ component. Because $\vec{P}^{L}$ and $\vec{P}^{NL}$ will give rise to different modes of field responses, we shall show that the generated wave behavior can be regarded as being separately influenced by the two excitation components ($\vec{P}^{L}$ and $\vec{P}^{NL}$). The linear response produced by $\vec{P}^{L}$ is given first; the nonlinear response generated from $\vec{P}^{NL}$ will be treated as a small perturbation to the linear solution based upon the size of its contribution towards the final output.

In the frequency domain, $\vec{E}$ and $\vec{P}$ can be transformed into their Fourier components through the Fourier transform[2]:

$$\vec{E}(r,t) = \sum_{n} \vec{E}(\omega_n, r)\exp(-i\omega_n t), \tag{2.7}$$

$$\vec{P}(r,t) = \sum_{n} \vec{P}(\omega_n, r)\exp(-i\omega_n t). \tag{2.8}$$

For each particular frequency component ω_n, there is a corresponding wave equation in the frequency domain that corresponds to Eq. (2.6):

$$\nabla^2 \tilde{E}(\omega_n, r) = -i\sigma\mu_0\omega_n \tilde{E}(\omega_n, r) - \mu_0\varepsilon_0\omega_n^2 \tilde{E}(\omega_n, r) - \mu_0\omega_n^2 \tilde{P}(\omega_n, r). \tag{2.9}$$

When only linear response is considered in the medium, the polarization is given by

$$\tilde{P}(\omega_n, r) = \tilde{P}^{L}(\omega_n, r) = \varepsilon_0\chi^{(1)}(\omega_n)\tilde{E}(\omega_n, r). \tag{2.10}$$

and therefore the wave equation for a particular Fourier component is then expressed as:

$$\begin{aligned} \nabla^2 \tilde{E}(\omega_n, r) &= -i\mu_0\sigma\omega_n \tilde{E}(\omega_n, r) - \mu_0\varepsilon_0\omega_n^2 \tilde{E}(\omega_n, r) - \mu_0\varepsilon_0\omega_n^2 \chi^{(1)}(\omega_n)\tilde{E}(\omega_n, r) \\ &= -i\mu_0\sigma\omega_n \tilde{E}(\omega_n, r) - \mu_0\omega_n^2 \varepsilon(\omega_n)\tilde{E}(\omega_n, r), \end{aligned} \tag{2.11}$$

where $\varepsilon(\omega_n) = \varepsilon_0\left[1 + \chi^{(1)}(\omega_n)\right]$.

The solution of Eq. (2.11) is a plane wave $\tilde{E}(\omega_n, r)$, which can be defined to propagate along the z direction:

$$\tilde{E}(\omega_n, z) = E(\omega_n, z)\hat{a}(\omega_n)\exp(ik_n z), \tag{2.12}$$

where $E(\omega_n, z)$ is the complex amplitude of the $\tilde{E}$ field, and $\hat{a}(\omega_n)$ is the unit vector of the field oscillation in transverse spatial coordinates. Substituting Eq. (2.12) into Eq. (2.11), we have

$$\frac{d^2E(\omega_n,z)}{dz^2}\hat{a}(\omega_n)\exp(ik_nz)+2ik_n\hat{a}(\omega_n)\frac{dE(\omega_n,z)}{dz}\exp(ik_nz)-$$
$$-k_n^2E(\omega_n,z)\hat{a}(\omega_n)\exp(ik_nz) \qquad (2.13)$$
$$=-i\mu_o\sigma\omega_nE(\omega_n,z)\hat{a}(\omega_n)\exp(ik_nz)-$$
$$-\mu_o\omega_n^2\varepsilon(\omega)\hat{a}(\omega_n)E(\omega_n,z)\exp(ik_nz).$$

Under the slowly varying amplitude approximation, $\left|k_n\frac{dE(\omega_n,z)}{dz}\right| >> \left|\frac{dE^2(\omega_n,z)}{dz^2}\right|$, Eq. (2.13) can be further simplified:

$$2ik_n\hat{a}(\omega_n)\frac{dE(\omega_n,z)}{dz}-\hat{a}(\omega_n)k_n^2E(\omega_n,z)+i\mu_o\sigma\omega_n\hat{a}(\omega_n)E(\omega_n,z)+$$
$$+\mu_o\omega_n^2\varepsilon(\omega_n)\hat{a}(\omega_n)E(\omega_n,z)=0 \qquad (2.14)$$

To include the nonlinear response inside the medium, the term $\vec{P}_{NL}(\omega_n,r)$ will be introduced as the contribution of nonlinear polarization at frequency ω_n. Eq. (2.9) takes the form of:

$$\nabla^2E(\omega_n,z)+\mu_o\omega_n^2\varepsilon(\omega_n)E(\omega_n,z)=-\mu_o\omega_n^2P_{NL}(\omega_n,z), \qquad (2.15)$$

where $P_{NL}(\omega_n,z)=P^{(2)}(\omega_n,z)+P^{(3)}(\omega_n,z)+\ldots$, assuming a lossless condition, i.e., $\sigma=0$.

Comparing Eq. 2.15 with the linear case [Eq. (2.9)], the term on the right hand side of Eq. (2.15) represents the source of the nonlinear excitation. When solving this equation, the nonlinear response is considered as a perturbation to the solution of the linear response based upon its small contribution. The solution of Eq. (2.15) can be written as[2]:

$$\vec{E}(\omega_n,z)=E(\omega_n,z)\left[\hat{a}(\omega_n)+\hat{b}(\omega_n,\ z)\right]\exp(ik_nz). \qquad (2.16)$$

The difference between linear and nonlinear optics [Eq. (2.12) vs. Eq. (2.16)] lies in the fact that both the complex amplitude of the $\vec{E}$ field and the oscillation unit vector becomes functions of the propagation distance z as $\vec{P}_{NL}$ participates in the excitation. Substituting Eq. (2.16) into Eq. (2.15), and neglecting the first and second derivatives [$\frac{d\hat{b}(\omega_n,z)}{dz}, \frac{d^2\hat{b}(\omega_n,z)}{dz^2}$], i.e., $\hat{b}(\omega_n,z)$ is a small and slowly varying quantity,

$$\begin{aligned} &-[2ik_n \frac{dE(\omega_n,z)}{dz} - k_n^2 E(\omega_n,z)]\hat{z}_o \times \{\hat{z}_o \times [\hat{a}(\omega_n) + \hat{b}(\omega_n,z)]\} \\ &+ \mu_o \omega_n^2 \varepsilon(\omega_n) \cdot [\hat{a}(\omega_n) + \hat{b}(\omega_n,z)] E(\omega_n,z) \\ &= -\mu_o \omega_n^2 P_{NL}^{'}(\omega_n,z) \exp(-ik_n z) \end{aligned} \quad , \tag{2.17a}$$

$$\begin{aligned} &2ik_n \frac{dE(\omega_n,z)}{dz} \left[\hat{a}(\omega_n) \times \hat{z}_o\right] \cdot \left\{\hat{z}_o \times \left[\hat{a}(\omega_n) + \hat{b}(\omega_n,z)\right]\right\} \\ &= \mu_o \omega_n^2 \hat{a}(\omega_n) P_{NL}^{'}(\omega_n,z) \exp(-ik_n z) \end{aligned} \quad , \tag{2.17b}$$

where $P_{NL}^{'}$ stands for the polarization when $\hat{b}(\omega_n,z)$ is omitted and $\hat{z}_o$ is the unit vector along the z direction. Expanding Eq. (2.17) and neglecting the product terms, one arrives at:

$$\frac{dE(\omega_n,z)}{dz} = \frac{i\mu_o \omega_n^2}{2[z_o \times \hat{a}(\omega_n)]^2 k_n} \hat{a}(\omega_n) P_{NL}^{'}(\omega_n,z) \exp(-ik_n z), \tag{2.18}$$

$$\frac{dE(\omega_n,z)}{dz} = \frac{i\mu_o \omega_n^2}{2k_n} \hat{a}(\omega_n) P_{NL}^{'}(\omega_n,z) \exp(-ik_n z), \tag{2.19}$$

where $\hat{z}_o \times \hat{a}(\omega_n) \approx 1$, i.e., the electric vector of a plane EM wave is perpendicular to the propagation direction.

Equation (2.19) is the steady state plane wave coupling equation. It is the fundamental work equation in the theoretical treatment of various nonlinear wave

interactions. Following derivations in the temporal domain, it has been shown by Shen *et al.*, that a similar wave coupling equation can be properly derived as[3,4]:

$$\frac{\partial^2 E_\omega(z,t)}{\partial z^2} + \frac{1}{v}\frac{\partial E_\omega(z,t)}{\partial z} = \frac{i\mu\omega^2}{2k_n}\hat{a}(\omega)\bar{P}^{\omega}_{NL}(z,t)\exp(-ik_\omega z), \qquad (2.20)$$

where the E field is in the form of $E(r,t) = E_\omega(z,t)\exp[i(kz-\omega t)] + \textit{complex conjugate}$.

Both Eq. (2.19) and Eq. (2.20) can be used to characterize the NLO effects of wave couplings. However, the solutions are obtained in different domains. In Eq. (2.19), the time functions of $\bar{E}$ and $\bar{P}$ have been converted into frequency domain functions by the Fourier transform, which makes the evaluation more straightforward. Equation (2.20) is direct and convenient for analyzing temporal behaviors of nonlinear processes. In the following section, Equation (2.19) will be used to evaluate second harmonic generation process.

2.3 Second Harmonic Generation

Second harmonic generation (SHG) is the first nonlinear optical phenomenon discovered by Franken and his co-workers shortly after the invention of laser.[5] It refers to a NLO process in which two incident photons at ω are simultaneously annihilated to create a new photon at twice the incident frequency 2ω.[1,2] As shown in Fig 2.1, SHG represents an electronic process, and the energy level involved is virtual in general. Second harmonic generation does not require energy exchange between the wave and medium; thus the creation of a new wave can be pictured as the energy is being exchanged between different frequency components. When the incident photon energy closely reaches a real absorption band, it is regarded as the resonant SHG.

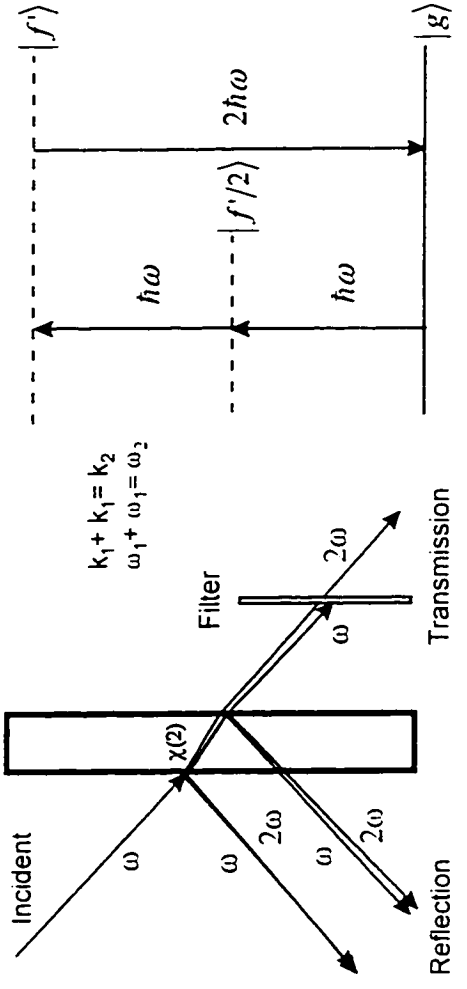

Fig. 2.1 Schematic and Jablonski diagrams of second harmonic generation (a): physical diagram of reflected and transmitted fundamental and second harmonic waves. (b): Jablonski diagram indicates that two incident photons at ω are destroyed and a single photon at 2ω is simultaneously generated. $|g\rangle$ is the initial state; $|f'/2\rangle$ and $|f'\rangle$ are the intermediate and final states, respectively. In general, $|f'\rangle$ and $|f'/2\rangle$ are virtual states.

Second harmonic generation is governed by the second order nonlinear optical susceptibility $\chi^{(2)}(\omega,\omega)$. It is a special case of the sum frequency generation. The second order nonlinear polarization is given by:

$$\vec{P}^{(2)} = \sum_{i,j} \varepsilon_0 \chi^{(2)}(\omega_i,\omega_j) : \vec{E}(\omega_i)\vec{E}(\omega_j)\exp\left[-i(\omega_i+\omega_j)t\right]. \tag{2.21}$$

Substituting the electric field $\vec{E} = \vec{E}_\omega \cos(k_\omega z - \omega t) = \vec{E}(\omega)\exp(-i\omega t) + \vec{E}^*(\omega)\exp(i\omega t)$, and setting $\omega_i = \omega_j = \omega$ in the above equation,

$$\begin{aligned}\vec{P}^{(2)}(2\omega) &= \frac{1}{4}\varepsilon_0 \chi^{(2)}(\omega,\omega) : \vec{E}_\omega \vec{E}_\omega \exp\left[i(2k_\omega z - 2\omega t)\right] \\ &+ \frac{1}{4}\varepsilon_0 \chi^{(2)}(-\omega,-\omega) : \vec{E}_\omega \vec{E}_\omega \exp\left[-i(2k_\omega z - 2\omega t)\right] \\ &= \frac{1}{2}\varepsilon_0 \chi^{(2)}(\omega,\omega) : \vec{E}_\omega \vec{E}_\omega \cos(2k_\omega z - 2\omega t)\end{aligned} \tag{2.22}$$

Equation (2.22) suggests that the second order nonlinear polarization component will give rise to light emission at 2ω in the presence of an incident wave and $\chi^{(2)}(\omega, \omega)$.

The harmonic generation can be explained by introducing $\vec{P}^{(2)}$ into the wave coupling equation [Eq. (2.19)]:

$$\frac{dE(2\omega,z)}{dz} = \frac{2i\omega^2}{k_{2\omega}c^2}\chi^{(2)}(\omega,\omega)E^2(\omega,z)\exp(i\Delta k z), \tag{2.23}$$

$$\frac{dE(\omega,z)}{dz} = \frac{i\omega^2}{k_\omega c^2}\chi^{(2)}(2\omega,-\omega)E(2\omega,z)E^*(\omega,z)\exp(-i\Delta k z), \tag{2.24}$$

where $\Delta k = 2k_\omega - k_{2\omega}$. Equation (2.23) can be solved by integration:

$$\int_0^z dE(2\omega,z) = \int_0^z \frac{2i\omega^2}{k_{2\omega}c^2}\chi^{(2)}(\omega,\omega)E^2(\omega,z)\exp(i\Delta kz)dz, \tag{2.25a}$$

$$E(2\omega,z) = \frac{4\omega^2}{k_{2\omega}c^2}\chi^{(2)}(\omega,\omega)E^2(\omega,0)z\exp\left(i\frac{\Delta k}{2}z\right)\frac{\sin\left(\frac{\Delta k}{2}z\right)}{\Delta kz}. \tag{2.25b}$$

The electric field and its intensity is related by:

$$I = 2n\left(\frac{\varepsilon_\omega}{\mu_\omega}\right)^{1/2}|E|^2, \tag{2.26}$$

where n is the index of refraction. Therefore,

$$I(2\omega,z) = \frac{2\omega^2}{n_{2\omega}n_\omega^2c^2}\frac{\mu_\omega}{\varepsilon_\omega}\left|\chi_{2\omega}^{(2)}\right|^2 I^2(\omega,0)z^2\frac{\sin^2\left(\frac{\Delta k}{2}z\right)}{\left(\frac{\Delta k}{2}z\right)^2}. \tag{2.27}$$

Equation (2.27) describes the SH wave intensity propagating inside a homogeneous nonlinear optical material. The generated harmonic field has a maximum output at $\Delta k = 2k_\omega - k_{2\omega} = 0$. This means that the index of refraction of the medium should satisfy $n_\omega = n_{2\omega}$. Under such a condition, the process is called phase matched SHG. Phase matching is a critical factor that determines the conversion efficiency based on energy and momentum conservation. When waves at ω and 2ω travel at the same speed, second harmonic signal will build up in phase. Another important parameter in second harmonic generation is the coherence length l_c, which defines the distance when the harmonic amplitude first reaches its maximum. The coherence length is derived from $\frac{\Delta kz}{2} = \frac{\pi}{2}$. By solving $z = l_c$, $l_c = \frac{\lambda}{4(n_\omega - n_{2\omega})}$.

One can see from Eq. (2.27) that $I(2\omega)$ depends on the squared quantities of the following parameters: the $\chi^{(2)}$ coefficient, the primary wave intensity, the reciprocal of the index of refraction n_ω, the phase matching factor $[\sin(\Delta k_j 2\cdot z)/\Delta k z]$ and the propagation path length. The quadratic dependence on the incident intensity is a very useful characteristics that later on will be demonstrated in biomedical imaging applications for achieving optical sectioning using localized excitation.[8-10]

2.4 Second Harmonic Generation in Random Media

Optical harmonic generation in randomly oriented particles of powder exhibits several striking differences when compared with the HG process in homogeneous materials. The air gaps formed between the particles generate index of refraction changes which lead to light scattering due to reflection and refraction at the air-particle interfaces(Fig. 2.2). The transmission-scattered and back reflection-scattered waves have different angular and intensity distributions, both of which become functions of the average particle size, sample thickness and the index of refraction mismatch. It was also found that the orientation of the crystallographic axis inside individual phase-matchable particles contributes to the final intensity, spatial, and temporal profiles of the harmonic signal. The representative theoretical analysis will be outlined in this section to bring insight into the SHG in model random medium. Specifically, only non-phase-matching schemes will be given, because random samples and biological tissues are in general non-phase-matchable materials.

It is well known that NLO effects of electronic origins highly depend on the incident wave intensity, phase structure, polarization and the direction of wave propagation. When dealing with homogenous media, the incident light is considered to

have a well defined phase structure, polarization, and direction of propagation. In most cases, the wave energy is assumed to be undepleted as the light transverses the medium. On the contrary, all these mentioned properties inside a random medium become functions of the scattering and absorption properties such as the particle size, the propagation distance, and the index of refraction change at both fundamental and second harmonic wavelengths. This dependence results in different intensity and spatial distributions of the primary and second harmonic waves. When incident photons are injected into a random medium, two scattering processes simultaneously exist inside the medium: one at ω and another at 2ω. There are also two possible absorption processes coexisting in the same region. To investigate how the injected photons are affected by the disordered medium during the excitation process, it is necessary to know the incident intensity distribution as a function of the propagation distance z.

The light scattered in the forward direction (z) at ω consists of a combination of three temporally spreaded components: ballistic (coherent), snake (quasi-coherent) and diffusion (incoherent) components. The ballistic component is the portion of the light that retains the coherence of the original beam. For the sake of simplicity, we adopt a special solution of wave intensity in a slab of infinite medium with air before z=0 and after distance z. The ballistic component is defined as[11-13]:

$$I_{ballistic} = I_{0}(\omega)\exp\left[-z/l_{s}\right], \tag{2.28}$$

where $I_{0}(\omega)$ is the initial incident intensity, l_{s} is the scattering length and the absorption length l_{a} is assumed to be zero.

The snake light is an early portion of the diffuse component and is defined as:

$$I_{snake}(\Delta t) = A\exp\left[-bz / l_t\right], \tag{2.29}$$

where Δt is the time slice at the early portion of the temporal profile, and $b \approx 0.8$ is assumed for demonstration. A is a constant depending on the experiment geometry. The transport length l_t is defined as $l_t = l_s / (1-g)$, where g is the mean cosine of the photon scattering angle.

The diffusion component is given by:

$$I_{diffusion} = \frac{\sinh\left[(3/l_t l_a)^{1/2}(1.42 l_t)\right] I_o(\omega)}{2\sinh\left[(3/l_t l_a)^{1/2}(z+1.42 l_t)\right]}. \tag{2.30}$$

When absorption is neglected, Eq. (2.30) can be simplified as:

$$I_{diffusion} = 0.71 I_o(\omega) l_t / (z + 1.42 l_t). \tag{2.31}$$

Fig 2.3 shows the calculation of the normalized intensity distributions of the primary wave and their corresponding squared quantities for the ballistic, snake and diffusion components, respectively. Since $I(2\omega) \propto I^2(\omega)$, the evolution of these three components as functions of z are evaluated to decide their contributions towards the total harmonic signal. The ballistic component decreases exponentially as z increases, indicating that the coherence of the primary wave drops sharply due to the scattering in a disordered medium. After the first scattering length l_s, the number of survived ballistic photons is approximately 3 times less than the original value, and l_s is generally only a few tens of micrometers for a highly turbid medium such as biological tissues. This distance suggests that ballistic photons contribute only up to the second

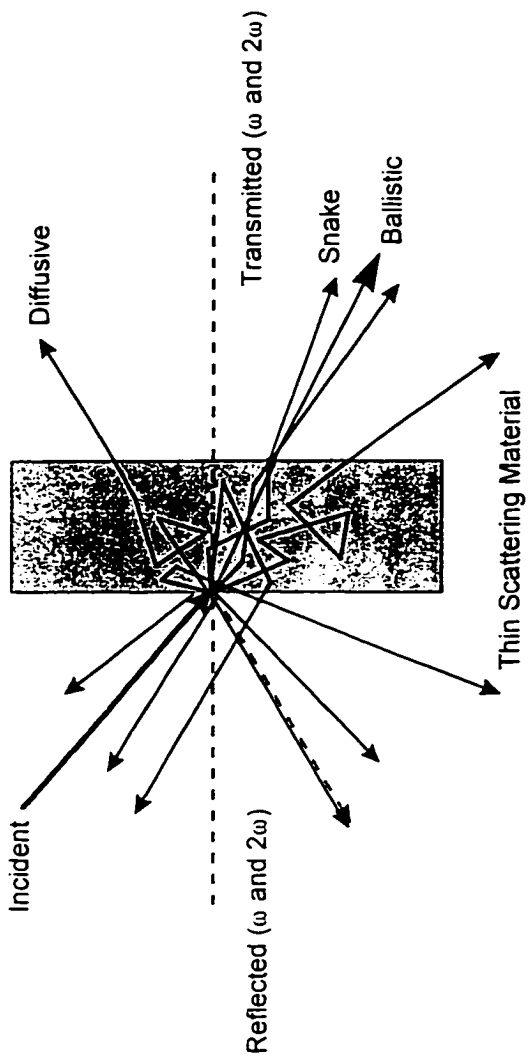

Fig. 2.2 Schematic diagram of fundamental and second harmonic light in a scattering medium.

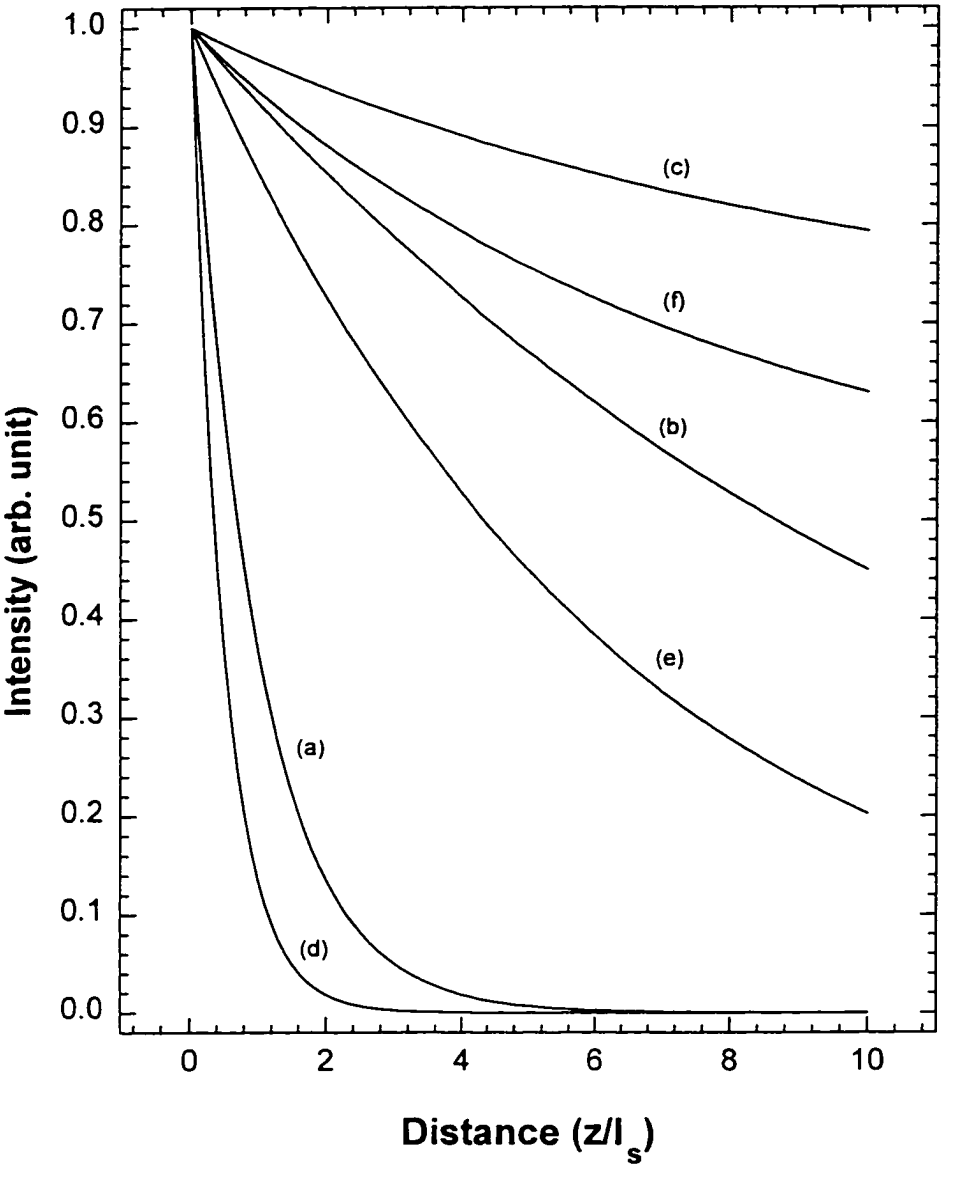

Fig. 2.3 Intensity decays of the ballistic (a), snake (b), and diffussion (c) components respectively. Curve (d), (e) and (f) are the corresponding decays of the squared quantities of (a), (b) and (c), respectively. Absorption is neglected g=0.9. In biological tissues, ls =50 - 300 micrometers.

scattering length $2l_s$. The number of the snake photons that still partially retain the coherence decreases slower than the number of the ballistic photons. After two scattering lengths, the contribution from the ballistic component is negligible while the diffusion photons remain as the majority. Optical excitation using diffusion light can be considered as an incoherent input where the photons have randomly distributed wave characteristics, resulting in inefficient harmonic generation and signal cancellation. For contributions from ballistic and snake components, the photons at 2ω will experience a second scattering or absorption process which is determined by l_s and l_a at the harmonic wavelength 2ω.

Kurtz and Perry investigated second harmonic generation from a series of powder crystalline samples.[12] Although aimed at the classification of $\chi^{(2)}$ materials, the study also serves as a guideline for SHG in discrete random media. The important parameters which impact on the SH signal intensity are: the average particle size, the number of particles within the excitation volume, the average coherence length, the effective second order nonlinear optical susceptibility, and indices of refraction at both fundamental and second harmonic wavelengths.

The theoretical approach for solving the steady state SH intensity generated from a random medium begins with finding $I(2\omega)$ in a single noncentrosymmetric crystal particle of size r. Substituting z=r and using $l_c = \lambda/4(n_\omega - n_{2\omega})$, $\Delta k = 2k_\omega - k_{2\omega} = 4\pi(n_\omega - n_{2\omega})/\lambda = \pi/l_c$, $\Delta k/2 = \pi/2l_c$ in Eq. (2.27), one can obtain the following expression for the SH intensity:

$$I(2\omega) = \frac{8\omega^2\mu_0 l_c^2}{\pi^2 n_{2\omega} n_\omega^2 \varepsilon_0}\left|\chi^{(2)}(\omega,\omega)\right|^2 I^2(\omega,0)\sin^2\left(\frac{\pi}{2}\frac{r}{l_c}\right), \tag{2.32}$$

where l_c is the coherence length.

The next step is to extend Eq. (2.32) by incorporating the averaged parameters of r, *lc*, and then summing over the particles and angular averages of $\chi^{(2)}_{2\omega}$. The SH intensity generated through a thin layer of non-phase-matchable crystal powders and collected over the entire 4π solid angle is given by:

$$I(2\omega) \cong \frac{8\omega^2\mu_o}{\pi^2 n_{2\omega} n_\omega^2 \varepsilon_o} \left\langle \left(\chi^{(2)}{}_{2\omega} \right) \right\rangle^2 I^2(\omega,0) L \frac{\bar{l}_c^{\,2}}{\bar{r}} \sin^2\left(\frac{\pi}{2} \frac{\bar{r}}{\bar{l}_c} \right), \tag{2.33}$$

where $\bar{r} << L << D$, $\bar{r}$ =average particle size, L =layer thickness, D=beam width, and $\bar{l}_c = \left\langle \lambda / 4\left(n_{2\omega} - n_\omega \right) \right\rangle_{av}$ is the ensemble average coherence length. In deriving Eq. (2.33), index matching liquid is assumed to be embedded between particles.

It is the relative sizes of $\bar{r}$ and $\bar{l}_c$ that determine whether the SH signals from adjacent particles are phase correlated. For a $LiNbO_3$ microcrystal sample, $\bar{l}_c \approx 5.82$ μm, and $\bar{r}$ can be in the range of 10-100 μm. If $\bar{r} >> \bar{l}_c$, one can assume that the harmonic signal generated by different particles are uncorrelated and proceed to sum up the contribution from each individual particles. This assumption also permits one to average the angular dependence of $\chi^{(2)}_{2\omega}$ tensor components. The term $\sin^2\left(\pi\bar{r}/2\bar{l}_c\right)$ in Equation (2.33) suggests an oscillatory behavior for $I(2\omega)$ when $\bar{r} < \bar{l}_c$. The oscillation will smear out as the root mean square deviation of r from averaged size $\bar{r}$ exceeds the averaged coherence length. For $\bar{r} << \bar{l}_c$, $\sin^2\left(\pi\bar{r}/\bar{l}_c\right) \sim \left(\pi\bar{r}/\bar{l}_c\right)^2$ and $I^{2\omega} \propto \bar{r}L$.

Although the harmonic signal generated from different particles tends to correlate with each other when $\bar{r} << \bar{l}_c$, the derivation can proceed by breaking the total layer into N regions where $N = L / \bar{l}_c$ with $N' = \bar{l}_c / \bar{r}$ particles in each region. The nonlinear polarization P_{NL} within each region can be treated by a one dimensional random walk model where the step length is proportional to $\chi^{(2)}{}_{2\omega}$. The

net contribution of each region to the total SH intensity is proportional to $\left\langle \left(\chi^{(2)}{}_{2\omega} \right)^2 \right\rangle / N'$, which leads to

$$I^{2\omega} \propto N\left[\left\langle \left(\chi^{(2)}_{2\omega}\right)^2 \right\rangle / N'\right] = \left(L / \bar{l}_c\right)\left\langle \left(\chi^{(2)}_{2\omega}\right)^2 \right\rangle \left(\bar{r} / \bar{l}_c\right)$$
$$I^{2\omega} \propto \bar{r}L. \tag{2.32}$$

Therefore,

$$I^{2\omega} \propto \frac{8\omega^2 \mu_0}{\pi^2 n_{2\omega} n_\omega^2 \varepsilon_0} \left\langle \left(\chi^{(2)}{}_{2\omega} \right) \right\rangle^2 I^2(\omega,0)\bar{r}L \qquad \text{for } \bar{r} << \bar{l}_c ,$$
$$I^{2\omega} \propto \frac{8\omega^2 \mu_0}{\pi^2 n_{2\omega} n_\omega^2 \varepsilon_0} \left\langle \left(\chi^{(2)}{}_{2\omega} \right) \right\rangle^2 I^2(\omega,0)\left[\left(\bar{l}_c\right)^2 / 2\bar{r}\right] \qquad \text{for } \bar{r} >> \bar{l}_c . \tag{2.33}$$

For $\bar{r} << \bar{l}_c$, $I^{2\omega}$ increases with the particle size and sample thickness. For $\bar{r} >> \bar{l}_c$, $I^{2\omega}$ decreases with the particle size.

Based upon SHG measurements from random crystalline powders, two important properties can be deduced for evaluating second order nonlinear optical materials: first, the magnitude of the $\chi^{(2)}$ tensor components relative to a known reference material such as quartz or KDP; and second, the existence or absence of phase matching ability.

References

1. A. E. Franken, C. Hill, W. Peters, and G. Weinreich, Phys. Rev. Lett. 7, 118 (1961).

2. Yi Ji Guo, "*Nonlinear Optics*", Publisher of Northwestern Electronic Communication Engineering, China (1987); N. Bloembergen, "*Nonlinear Optics*", Benjamin, New York (1965).

3. G. C. Baldwin, "*An Introduction to Nonlinear Optics*", Plenum Press, New York (1969).

4. Y. R. Shen, "*Principles of Nonlinear Optics*", John Wiley and Sons (1984), and the references therein.

5. D. C. Hanna, M. A. Yuratich, and D. C. Cotter, "*Nonlinear Optics of Free Atoms and Molecules*", Heidelberg, New York (1979).

6. S. K. Kurtz and T. T. Perry, J. Appl. Phys. **39**, 3798 (1968).

7. V. E. Kravtsov, V. M. Agranovich, and K. I. Grigorishin, Phy. Rev. B, **44**, 4931 (1991).

8. W. Denk, J. H. Strickler, and W. W. Webb, Science **248**, 73 (1990).

9. P. E. Hanninen, E. Soini, and S. W. Hell, J. Microsc. **176**, 222 (1994).

10. D. W. Piston, B. R. Masters, and W. W. Webb, J. of Microsc. **178**, 20 (1995).

11. Feng Liu, Ph. D Thesis, City College of New York (1993).

12. A. Ishimaru, "*Wave Propagation and Scattering Random Media*", Academic Press, New York (1978).

13. M. Lax, V. Nayaramamurti, and R. C. Fulton, "*Laser Optics of Condense Matters*", Plenum Press, New York (1987).

Chapter Three

Harmonic Generation from Model Random Microcrystal Particles and Biological Tissues

In this chapter, harmonic generation from various microcrystal particles and biological tissues have been studied. Experimental results have shown that optical harmonic generation was connected to the histological structures of tissue in its signal strength. The conversion efficiencies of second- and third-harmonic generation from biological tissues have been determined to range from $10^{-7} \sim 10^{-10}$. Spectral and spatial measurements were performed to bring insight into nonlinear optical responses in scattering medium.

3.1 Histological Descriptions and Relevant Optical Properties of Biological Tissues

Animal and human bodies are made up of tissues which are aggregations of cells with various forms of morphology and functions. Different tissues exist inside an animal or human body: epithelial, connective, muscular, nervous, and other types that are derived from epithelial, endothelial or mesodermal tissues.

Tissues are made of particular types of cells organized in a three dimensional way and supported by the extra-cellular fibrous matrix. Cellular function is the combination, interaction and reaction of heterogeneous species of molecules. Cellular morphology exists on a microscopic scale and attributive to the next level in the hierarchy. Histology studies tissue's physical structure and chemical composition

which are the two important indicators closely related to the physiological state. Various studies have confirmed that certain structural symmetry and order exist inside a biological system despite its chemical and physical heterogeneity.[1,2] Morphogenesis of symmetry may be present either on a microscopic or on a macroscopic level. For example, spherical symmetry has been found in adipose cells that comprise the fatty tissue (Fig. 3.1). Cylindrical symmetry is present in skeletal muscle fibers which are consisted by fine internal arrays of striated protein filaments (Fig. 3.2). Orderly arranged oval shaped crypts are neatly packed in the top layer of the human colon mucosa. Finger-like villi with similar morphological shape cover the luminal surface of the small intestine (Fig. 3.3). An overall polarity that can only arise from specific molecular arrangements maintained over macroscopic distances has been observed in the rat tail tendon system.[3]

Symmetry and order not only play roles in maintaining structurally related biological functions but also determine the underlying tissue's linear and nonlinear optical properties. Depending on the wavelength of the light illumination, symmetry properties will affect light reflection, refraction, transmission, polarization (birefringence) and especially nonlinear wave interactions inside the tissue.

A nonlinear optical process is accompanied by other linear processes. In most linear biomedical optics, the investigation depends on using the index of refraction and phase changes in light transmission or reflection to bring contrast of targeted cellular components relative to their environment. The index of refraction or phase change is transformed into intensity changes which can be visualized. The primary linear parameters in nonscattering tissues are: the index of refraction n, the optical density (OD), and optical path length z. In terms of nonlinear optical properties, the primary

Fig. 3.1 Scanning electron micrograph of the spherical shaped fat cells in animal adipose tissues.

After reference 1.

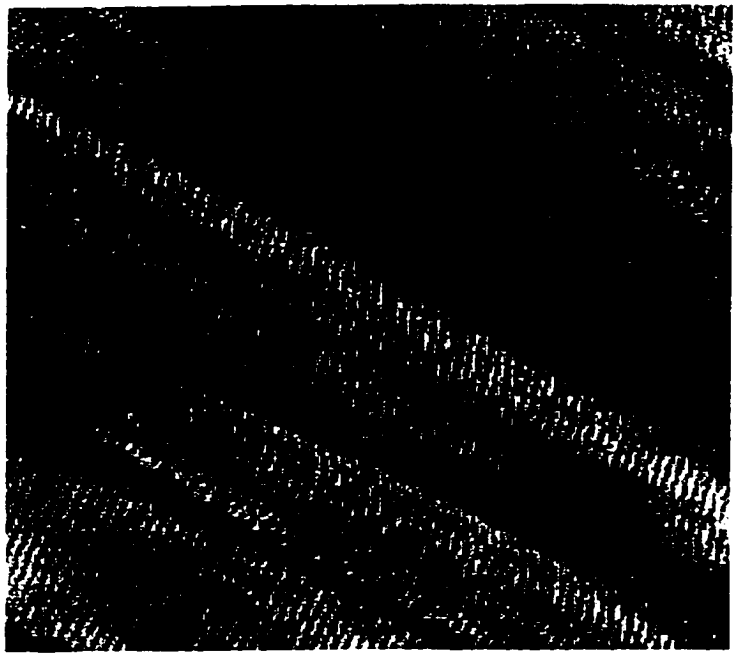

Fig. 3.2 Human striated muscle tissue in which muscle fibers are neatly arranged with their long axis parallel to each other. Inside each fiber, an organized array of the striated structure can be seen.

Reproduced from Michael Abbey/Science Source/Photo Researchers Inc.

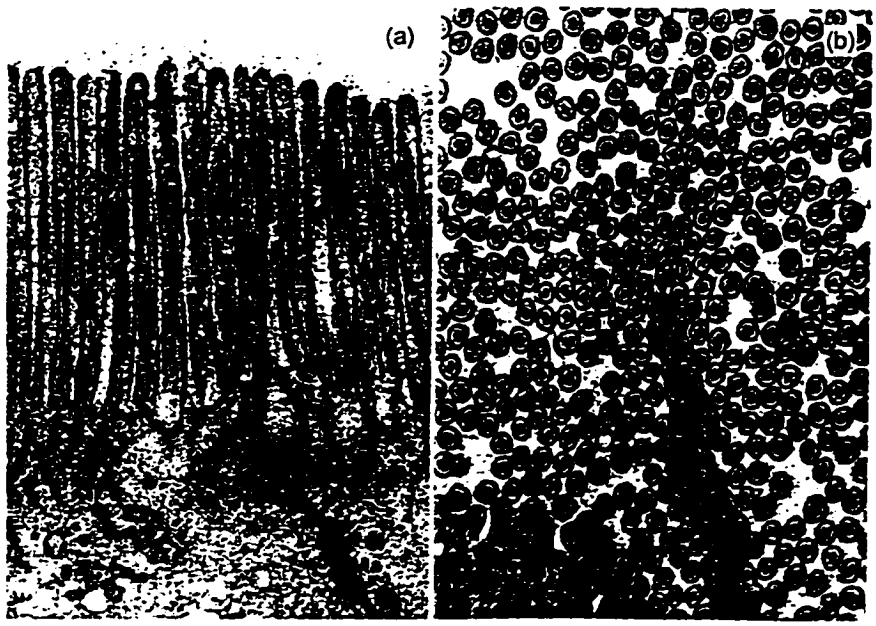

Fig. 3.3 Cross sectional (a) and top (b) view of human small intestine surface in which finger-like villi can be seen.

After reference 2.

parameter defining the nonlinear response is $\chi^{(n)}$ ($n > 1$). A n^{th} order nonlinear optical signal usually scales with powers of n to the excitation intensity. The response derived from $\chi^{(n)}$ directly depends on the detailed electronic configuration, molecular symmetry, and the morphology of the ultrafine structures within the scale of the light wavelength. Although both linear and nonlinear signals can be physically generated from the same group of structures, their respective responses may exhibit different temporal, spectral and spatial characteristics. For example, the linearly reflected light depends on OD, n, and z. The reflected second harmonic light, in the nonlinear regime, depends on $\chi^{(2)}$, the $1/n_{\omega}^{2} n_{2\omega}$ and I_{pump}^{2}. The SH light has a characteristic frequency at twice the incident light frequency, a narrower temporal pulse width, and a smaller transversal spatial distribution compared with those of the fundamental wave.

An integrated nonlinear optical response can be modified by several related linear optical parameters. This influence is derived from the wave equation that defines the nonlinear wave interactions. The second harmonic signal is related to $1/n_{2\omega}^{2} n_{\omega}$, z^{2}, and $[\sin(\Delta k/2 \cdot z)/\Delta kz]^{2}$. When theoretically extracting the $\chi^{(2)}$ tensors, it is necessary to have an accurate knowledge on these linear parameters. On the other hand, one may use this relationship to highlight small changes in the linear optical parameters for practical purposes.

3.2 Optical Detection Techniques in Second Harmonic Generation

Studies in SHG have been developed along two lines: the first direction concentrates on theories and experiments in frequency conversion, searching for high efficiency nonlinear crystals/polymers, and NLO devices. The second direction uses SHG to study the basic structure of matter, especially configurations of electrons and molecules, surface or interface nonlinear properties, and photodynamic processes. The

results in this later area have established SHG as a standard probing technique in various scientific fields.

The details of SHG study can be summarized into the following aspects:

(1) Measurements of the absolute or relative SH intensity including determination of phase matching property and conversion efficiency.

(2) Determination of resonant and nonresonant second order optical nonlinear susceptibility $\chi^{(2)}$ and its tensor components including sign and magnitude.

(3) Evaluation of phase factors of $\chi^{(2)}$.

(4) Investigation of spatial properties including polarization dependence and angular distributions.

(5) Evaluation of spectral and temporal domain related second order nonlinear effects.

(6) Determination of surface second harmonic generation and interfacial properties.

The experimental arrangements for SHG measurements[4] are illustrated in Fig. 3.4 and 3.5. The light pulses generated from a laser source are delivered by mirrors and are passed through polarization control optics and then focused by a lens onto the sample. The transmitted second harmonic signal, propagating co-linearly with the fundamental light, is separated out by optical filters, grating, or prism and then collected by a photodetector.

In Fig. 3.5, the laser beam is split into two equal portions: one is used to excite SHG from the sample, and the other one to generate SH signal in a reference crystal with known $\chi^{(2)}$. The ratio between signals from the sample and the reference crystal is then used to deduce the nonlinear optical susceptibility of the sample. When measuring the tensor components of $\chi^{(2)}$, a particular set of polarizations of the fundamental and

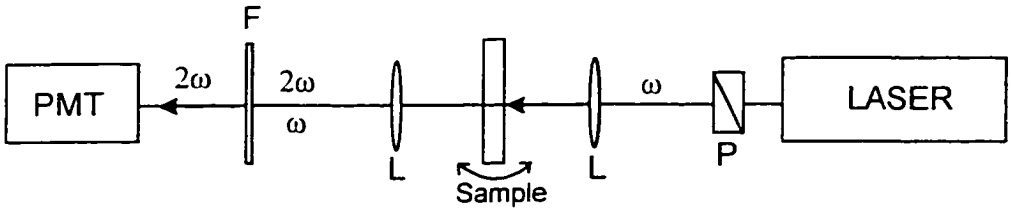

Fig. 3.4 Experimental setup of transmission detection of SHG from nonlinear crystals. P: polarizer, L: lens, F: filter, PMT: photomultiplier tube.

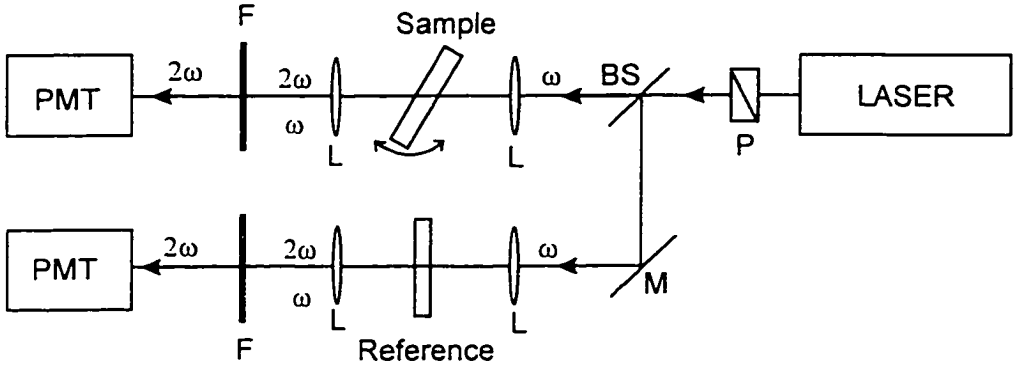

Fig. 3.5 Experimental setup of transmission detection of SHG from nonlinear crystals. BS: beam splitter, M: mirror, P: polarizer, L: lens, F: filter, and PMT: photomultiplier tube. The ratio of SHG from the sample and reference paths allows relative measurements of second order nonlinear optical susceptibility.

second harmonic light will be chosen. The sample is set to an angle with respect to the excitation beam. By varying the angle of inclination, the second harmonic intensity output from the sample will vary periodically between a maximum and a minimum value as the optical thickness varied from an even multiple to an odd multiple of the coherence length. The resultant fringes of the SH intensity versus the inclination angle are known as the Maker fringes which can be used to determine $\Delta k \cdot z$ and $\chi^{(2)}$.

The experimental setup for measuring the phase factor of $\chi^{(2)}$ uses two slabs of crystals arranged in series. The phase matched SH output from the first crystal feeds the input of the second crystal. Interference peaks will be generated in the output SH intensity from the second crystal depending on the relative phase of $\chi^{(2)}_{1.eff}$ and $\chi^{(2)}_{2.eff}$ in the first and second crystals. From the variation of the SH output, the phase factor of $\chi^{(2)}$ can be deduced.[5,6]

Among scattering media, SHG from microcrystal powders has been studied by Kurtz *et al.* who used an integrating sphere or parabolic mirror shown in Figs. 3.6a and b to collect the SH light scattered in all directions.[7] A thin layer of the particles was used to ensure signal transmission. A weakly focused excitation beam was used to include averaged response from a large number of particles.

SHG in biological tissues was first measured using transmission geometry similar to the setup shown in Fig. 3.5. In early investigations, either transparent or quasi-transparent samples such as cornea, retinal-choroidal, lens, and thin layer of tendon were selected to minimize scattering and absorption effects.[3,7,8] The SHG measurement conducted in this thesis study has emphasized on reflection/back-scattered detection geometry. The biological samples investigated are highly scattering media. Reflected signals are suitable for minimal invasive evaluation and characteriza-

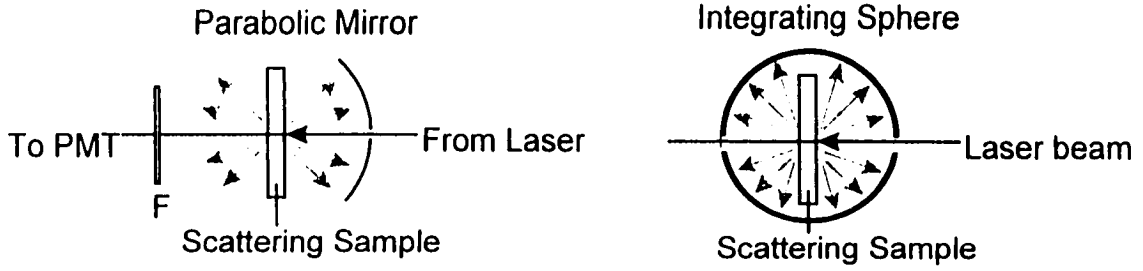

Fig. 3.6 Experimental setup for SHG measurement in scattering microcrystal powder particles. A parabolic mirror (a) or an integrating sphere (b) is used to collect the SH signal. F is a filter and PMT is a photomultiplier tube.

tion of nonlinear responses from tissues. It is also essential for studying thick samples having varying particle size and highly scattering properties.[9]

The determination of the second order $\chi^{(2)}$ coefficient in biological tissues can be severely hampered by the heterogeneity present in both the structure organization and molecular compositions. Scattering, absorption, and component distribution make the extraction of absolute $\chi^{(2)}$ value virtually impossible. While no exact optical method is available for solving this problem, three currently applied techniques are used to answer the challenge.

The first is to measure a extracted structure component and compare the result with the averaged response and histology from the same tissue. This can be done in a way similar to that utilized in a fluorescence spectroscopy, where independently measured results were compared between purified molecules and specimens obtained through surgical biopsy. In this thesis, the composition dependence will be investigated to analyze SHG, THG, and TPF in tissues.

The second technique is to use certain chemical agents and selected optical excitation to activate a particular molecular group and then correlate the results with the histology. This type of method has been used in probing cell membrane potentials, where dye molecules were introduced to bind and orient in the lipid bilayer, providing sensitivity of surface SHG to detect cell membrane potentials.[10]

The third technique is to use high resolution microscopy to locate signal down to the cellular and sub-cellular structure level comparable to the accuracy found with histology. The technique involves achieving a diffraction limited focal spot in the specimen through a high power microscope objective and detecting the signal using confocal and other background rejection methods.[11]

3.3 Harmonic Generation Measurements from Randomly Oriented Microcrystal Particles and Biological Tissues

3.3.1 Intensity Measurements

3.3.1a Experimental Methods and Samples

A schematic diagram of the experimental setup for MHG from highly scattering biological media is shown in Fig. 3.7. Femtosecond laser pulses were generated from a Kerr lens self-mode-locked Ti:Sapphire laser oscillator with a repetition rate of 76 MHz. The pulse width was 120 fs, and the wavelength was adjusted to 810 nm. The average power density of the laser output was approximately 10^6 W/cm^2. After suitable attenuation, the beam was focused by a 8.8 cm focal-length lens onto the sample at an incident angle of 45 degrees, with a power density of 2.8×10^8 W/cm^2 at the focal spot. The reflected diffusive light was collimated and collected through a pair of quartz lenses into a spectrometer coupled to a photomultiplier tube and a computer controlled lock-in amplifier system. A long wavelength pass filter was placed in front of the focusing lens to cut any possible signal contribution from laser cavity and on-line optics. A short band pass filter was placed at the entrance of the spectrometer to eliminate light scattering at the fundamental wavelength. In order to confirm that the harmonic signal was generated from the samples, the excitation beam was gradually defocused to check if the harmonic signal diminished accordingly.

The third harmonic generation measurements were performed using the 30 ps pulses at 1064 nm generated from a Nd:YAG laser under the same experimental arrangement. The pulse repetition rate was 10 Hz, and the peak intensity at the sample site was 1.96×10^9 W/cm^2. For signal detection under pulsed excitation with low repetition rate, a boxcar averaging unit was used instead of a lock-in amplifier. When

measuring the polarization dependence, a $\lambda/2$ waveplate in conjunction with a polarizer and an analyzer were used to select the polarization states of the incident and signal beams. A de-polarizer was inserted in front of the entrance slit to eliminate any polarization preference of the optics inside the spectrometer.

Native chicken tissue samples (frozen then thawed) were obtained from the upper thigh portion. A large sample section ($3 \times 3 \times 2$ cm^3) was used to avoid external stress and forces. The interfaces examined were directly exposed to the laser radiation. The SHG signal was detected and averaged for multiple scans and locations from fifteen samples.

To analyze the composition dependence, microcrystal powder samples were used in the investigation. The examined samples included powders of KDP, silica, sucrose, purified endogenous molecules of L-tryptophan (Trp), tyrosin (Try), Flavin Adenine Dinucleotide (FAD), elastin and chopped type I collagen. The microcrystal powder samples were purchased from Sigma Chemical Company. The characteristic size of the powder particles was ~ 20 μm.

Under a non-phase matched condition, the microcrystal KDP and sucrose samples were used as references. The measured SH and TH spectra and intensities from the reference samples with 810 nm and 1064 nm laser excitations were used to compare with the signal generated from other molecule and tissue samples.

In addition to MHG, up frequency conversion (sum frequencies) with two-photon resonance enhancement has been investigated in fluorescent micro-crystals. In Fig. 3.8, the frequency doubled 532 nm pulses were separated out from the 1064 nm output of the Nd:YAG laser, and recombined with the infrared beam through a dichroic mirror to form a co-linear excitation. The temporal overlap between the two beams was achieved through an optical delay stage. Neutral density filters were inserted to adjust

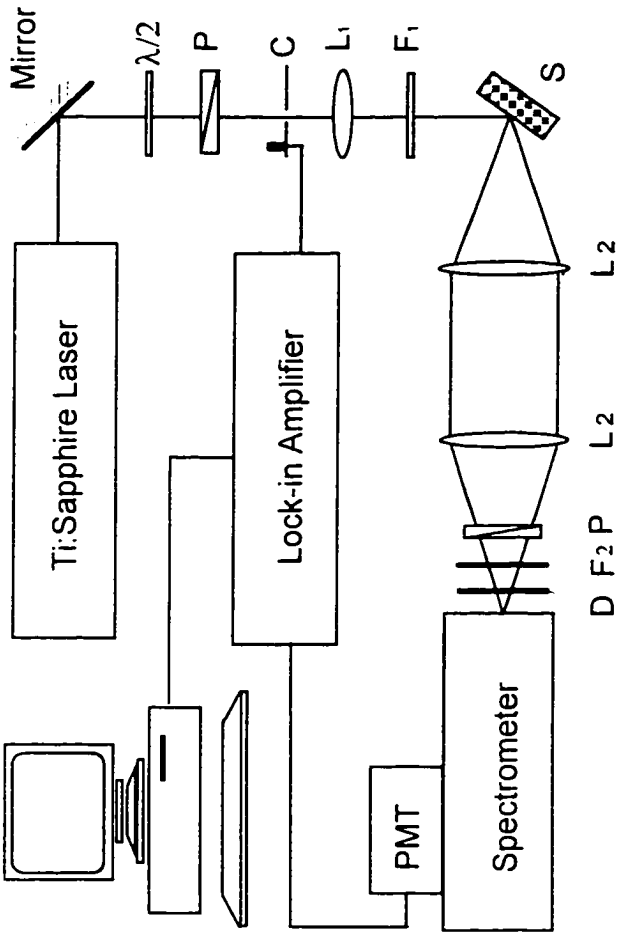

Fig. 3.7 Experimental setup for SHG and THG measurements from model random and biological media. λ /2: half wave plate; L 1 : focusing lens; L 2 : collecting lens; P: polarizer; F_1, F_2 : long and short pass filters, respectively; D: depolarizer; S: the sample and C is the chopper.

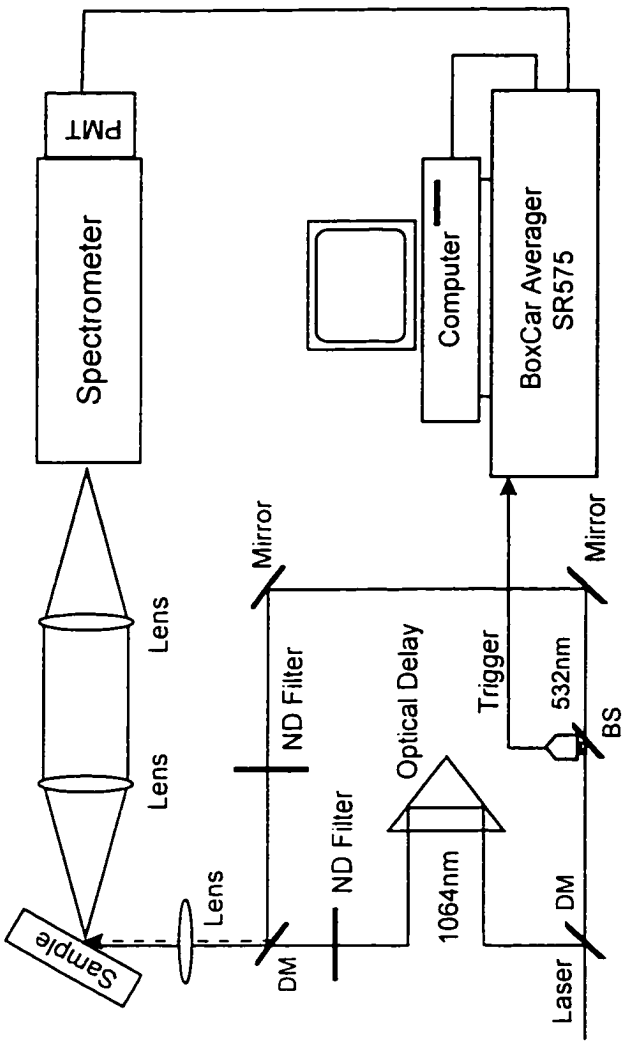

Fig. 3.8 Experimental setup for up conversion measurement from model random and biological media. DM is the dichroic beam splitter.

the power at the 1064 nm and 532 nm beam paths. The estimated pump intensity at the focus was ~ $2GW/cm^2$.

3.3.1b Results and Discussions

(i) Correlation Between Signal Strength and Tissue Structures: Fig. 3.9 presents the results of SHG intensity measurements from skin (curves a), muscle (curve b) and fat chicken tissues (curve c), under 810 nm, 120 fs laser excitation, respectively. The skin interface exhibited the largest SH intensity. The SH signal generated from the muscle interface was approximately 1 order of magnitude weaker compared with that from the skin tissue, while the signal from the fat interface was about 2 orders of magnitude weaker. The integrated SH signal is generated from an optically excited surface area (diameter $> 1/\mu_t \sim 200$ μm) and a subsurface volume defined by a volume integral of the squared Gaussian beam incorporated with attenuation. This signal was found to carry an averaged and quantified strength reflecting on the tissue's histology within the laser focal point. Compared with the previously reported studies in which only the existence of SHG has been observed without linking between different tissues, this strength-structure correlation is significant in facilitating the use of SHG to visualize histological structures at different tissue locations and to differentiate between tissue types.

The third harmonic signal has been observed for the first time using the 10 Hz excitation of a Nd:YAG laser output at 1064 nm. Under the same excitation, the faint green light of SHG was visually observable in the dark from the chicken skin tissue. The largest TH signal was observed from the skin tissue. In contrast to SHG, THG from fat was stronger than the signal from muscle (shown in Fig. 3.10). Therefore, the magnitudes of TH signal from fat and muscle were reversed as compared with SHG. It

was also noticeable that the magnitude differences between tissue structures were found to be smaller than those of SHG under femtosecond excitation. A third order power dependence on the pump intensity for the THG signals was confirmed as $n = 2.9 \pm 0.2$, and a quadratic dependence of $n = 1.8 \pm 0.3$ for SHG. The results were in agreement with the theory of $I(n\omega) \sim I^{n}_{pump}(\omega)$.

The THG is governed by the third order nonlinear susceptibility $\chi^{(3)}(3\omega)$ which can be orders of magnitude weaker than SHG. Under the electric dipole approximation, molecules and other tissue constituents possessing centrosymmetric structures will be prohibited for SHG. THG is a dipole allowed process in such materials. Surface SHG will dominate in two cases: (i) the material is centrosymmetric and (ii) the material is noncentrosymmetric but randomized on the scale of the wavelength. For THG, a bulk contribution should dominate regardless of the symmetry consideration.

The strength differences in the harmonic generation can be partially attributed to the structure of molecules and microscopic cellular components. The results in SHG versus THG indicate a lack of noncentrosymmetric response in the fatty tissue since it is more efficient in THG than in SHG. This finding is in agreement with the fact that in muscle and skin tissues, constituents such as tryptophan and collagen with noncentrosymmetric structures are greatly increased. Delocalized conjugated ring and π electron structure in amino acids such as tryptophan and tyrosine enhance a large noncentrosymmetric response. The double bond structure is absent in saturated fat molecules, suggesting a smaller response from the adipose tissue. In addition, how these molecules are organized and arranged into the tissue is an important factor since SHG is sensitive to orientational order in addition to molecular structures. For instance, collagen molecules are known to orient in parallel or antiparallel to form fibrils in

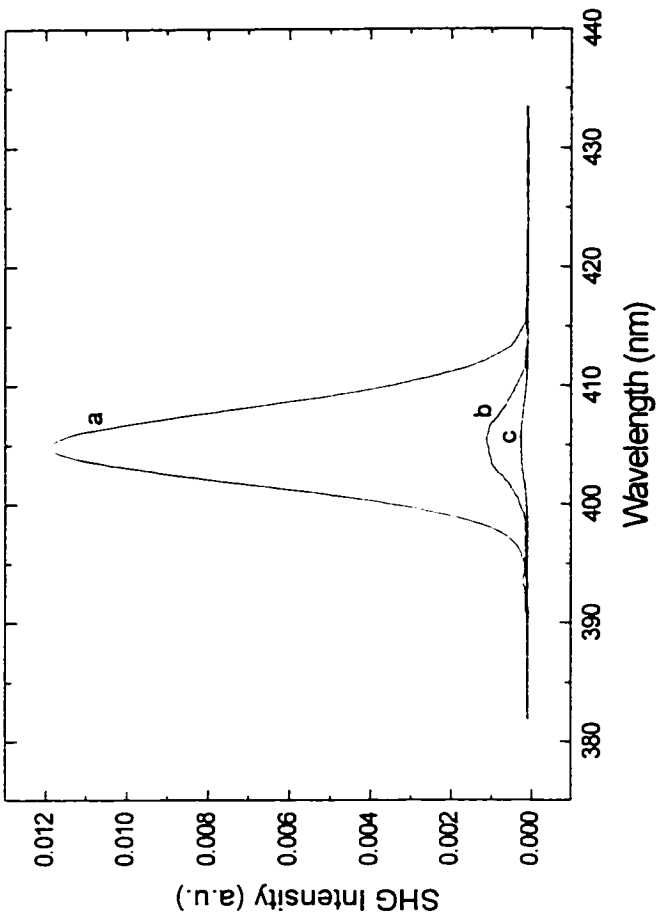

Fig. 3.9 Intensity spectra of second harmonic generation from chicken skin (a), muscle (b) and fat (c) tissues under 120 fs, 810 nm laser excitation.

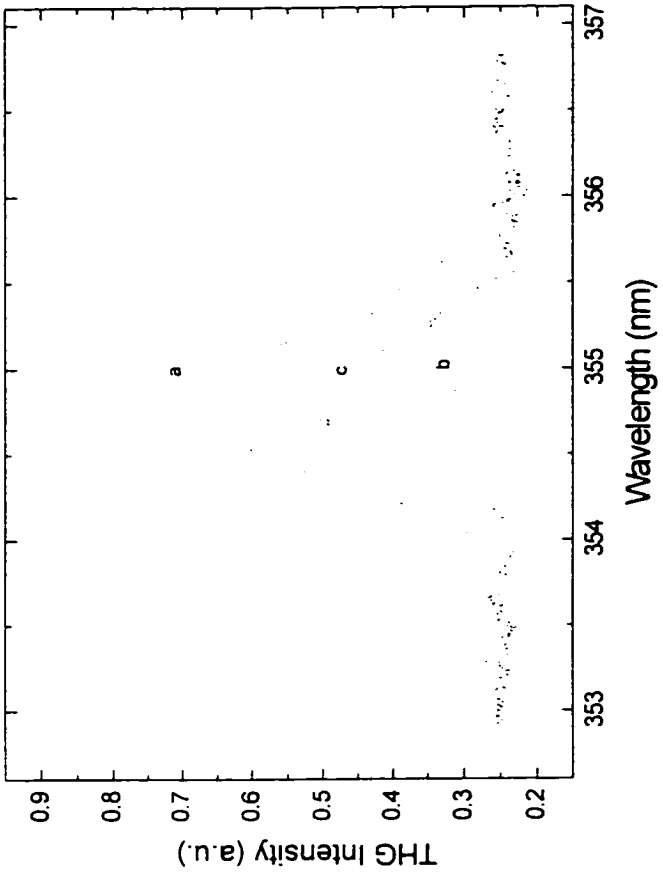

Fig. 3.10 Intensity spectra of third harmonic generation from chicken skin (a), muscle (b) and fat (c) tissues under 30 ps, 1064 nm laser excitation.

tissues.[3] These organized basic structures are advantageous for SHG. As for the skin tissue, the multi-layered interfacial effect and molecular packing density are also likely to contribute to the signal magnitude differences. For THG, since the nonlinear process does not depend on symmetry, molecules that do not participate in SHG will contribute to the signal. Delocalized conjugate electronic configuration of organic molecules and a larger scattering coefficient might explain the larger THG response from the skin tissue.

(ii) Composition Dependence: The typical spectral responses of SHG and THG from powders of Trp, collagen, FAD and sucrose molecules are shown in Fig. 3.11. The experimental arrangement and laser system were similar to those which have been previously described. The sharp peaks observed at 2ω and 3ω indicate the correct order of the second and third harmonic processes. L-tryptophan showed a SH signal 15 times stronger than that from the sucrose sample, while signals from collagen and FAD were 1 and 2 orders of magnitudes weaker than that of the sucrose, respectively. Tryptophan also exhibited the largest THG response, which was about 3 times stronger than that of sucrose. THG signal from collagen was 5 times smaller than sucrose, and no detectable TH signal can be observed from the FAD sample under the same excitation condition.

The result in this selected composition study was in agreement with the theory about the size of the $\chi^{(2)}$ response. A large second order nonlinearity requires an organic molecule to have a noncentrosymmetric structure, a delocalized π electronic configuration, and some low-lying resonance states which can be mixed with the ground state in charge transfer. Amino acid molecules (L-tryptophan, etc.) meet the structural requirement and have a large nonlinear susceptibility. Molecules with helical structures such as collagens and keratins also possess noncentrosymmetric response.

However, in terms of their electronic configuration they are not as efficient as

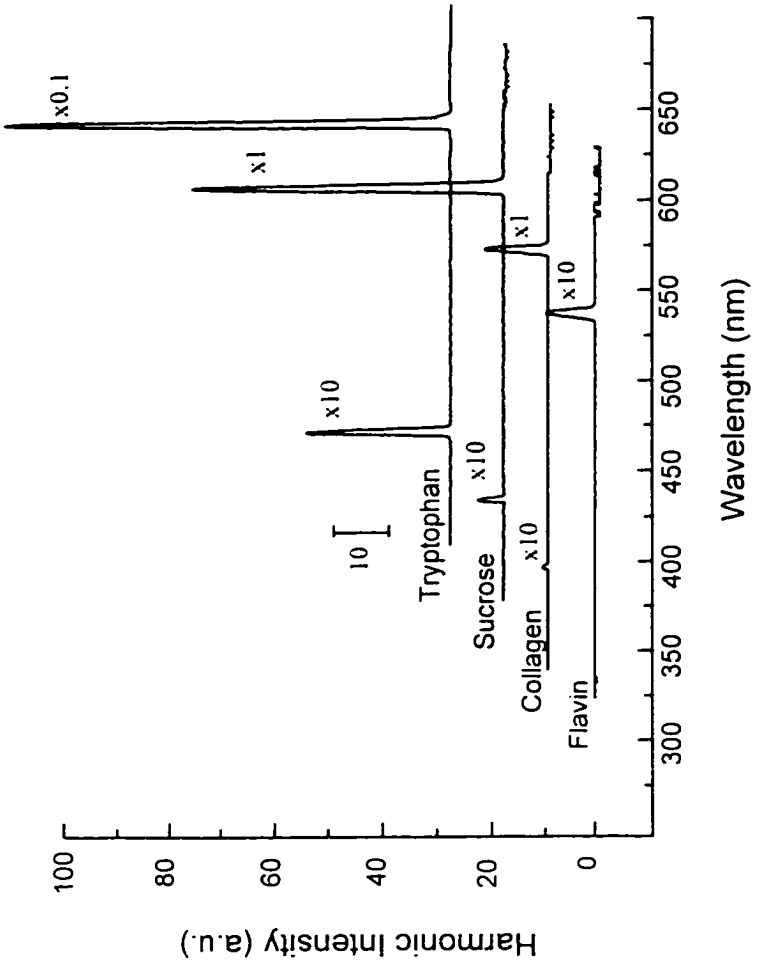

Fig. 3.11 SHG and THG spectra of tryptophan, collagen, and flavin ardenine dinucleotide powders. The excitation source was the 30 ps, 1064 nm light pulses generated from a Nd:YAG laser at a repetition rate of 10 Hz.

amino acids in SHG.

The electronic states of L-tryptophan in the UV region consist of two overlapped ^1L_a and ^1L_b bands.[12,13] Two photon transition can be prompted by simultaneously absorbing two photons at 532 nm. This resonant process was observed by two photon excitation of fluorescence (TPF) in the Trp powder between 300 - 400 nm above an excitation flux level of 10^{22} photons/cm^2·s. An up frequency conversion process was studied below and above this threshold with colinearly 1064 nm and 532 nm excitation. The total incident photon flux was kept fixed by varying the 532 nm input, while a compensation amount of the 1064 nm input was increased and decreased accordingly. The up-converted sum frequency signal was monitored at 355 nm as a result of the incident intensity changes.

Table 3.1 Second and third harmonic intensity ratio and conversion efficiencies of chicken tissue interfaces

Interfaces	$\frac{I_{2\omega}}{I_{2\omega,KDP}}$ *	$\frac{I_{3\omega}}{I_{3\omega,Sucrose}}$ *	SHG Conversion Efficiency	THG Conversion Efficiency
Chicken Skin	1.25×10^{-2}	0.46	$(2.0\pm0.8)\times10^{-7}$	$(1.4\pm0.6)\times10^{-9}$
Chicken Muscle	8.2×10^{-4}	0.12	$(1.3\pm0.5)\times10^{-8}$	$(3.5\pm1.0)\times10^{-10}$
Chicken Fat	7.8×10^{-5}	0.30	$(1.2\pm0.6)\times10^{-9}$	$(8.8\pm2.5)\times10^{-10}$

* $I_{2\omega}$ was measured at 405nm using the femtosecond Ti:Sapphire laser with peak intensity of 2.8×10^8 W/cm^2 under S polarization excitations, $I_{3\omega}$ was measured at 354.7 nm using the picosecond Nd:YAG laser.

Considering TPF as a background superimposed on the up-converted signal and subtracting it from the total response, a two fold increase in the up frequency conversion has been observed through a two photon assisted resonant enhancement.

(iii) **Conversion Efficiencies:** The conversion efficiencies in harmonic generations determine the ratio of the absolute intensities at both harmonic and fundamental wavelengths. The relative conversion efficiency in this study has been defined as $I_s(n\omega)/I_s(\omega)$ and ($n=2$ or 3), which is the intensity ratio of the diffusively scattered harmonic and reference fundamental signals within the collecting solid angle. This definition can be used under a quasi-uniform intensity distribution at both $n\omega$ and ω in modeled scattering media and biological tissues.

The deduced ratio of $I_s(n\omega)/I_s(\omega)$ is proportional to $|\chi^{(n)}|^n$ and I^n_{pump}. Since the extraction of the absolute $\chi^{(2)}$ value from tissues is extremely difficult, the relative figure of the conversion efficiencies provides useful information for evaluating the nonlinear optical effect. For the skin, muscle and fat tissue structures under examination, the measured conversion efficiency of SHG ranges approximately from 10^{-7} to 10^{-9}. The THG conversion was about two orders of magnitude smaller than that of SHG. It should be noted that these conversion ratios are higher than the usual value obtained from a single KDP crystal surface, since the scattered fundamental intensity was used instead of the incident one along with the inclusion of a subsurface contribution.

Table 3.1 summarizes the conversion efficiencies for different tissue interfaces and their relative numerical ratios of SH and TH intensity with respect to the reference samples (KDP and sucrose). Table 3.2 summarizes the results obtained from some basic molecules. The measured conversion efficiencies of SHG for Trp to FAD

vary from 10^{-6} to 10^{-8}. The conversion efficiencies of THG were about 3 orders of magnitudes lower than those of SHG for Trp and collagen, respectively.

(iv) Other Factors Affecting Harmonic Generation: In randomly oriented powders, long range order within each crystal particle will give rise to a bulk SHG signal. When molecules are centrosymmetric, or non centrosymmetric but with randomized arrangement, surface term emerges but carries a subsequently small response. The large differences observed in the strength of SHG from powders supported this point. Assuming an equal excitation volume and the same characteristic particle size, surface enhancement only has a secondary contribution towards the final output signal strength.

Table 3.2 SHG and THG conversion efficiencies of three basic fluorophore molecules in solid powder form

Interfaces	$\frac{I_{2\omega}}{I_{2\omega,KDP}}$	$\frac{I_{3\omega}}{I_{3\omega,Sucrose}}$	SHG Conversion Efficiency	THG Conversion Efficiency
L-tryptophan	15.38	3.2	$(2.8 \pm 0.4)\times10^{-6}$	$(9.5 \pm 2.8)\times10^{-8}$
Flavin Adenine Dinucleotide	1.5×10^{-3}	-	$(1.1 \pm 0.9)\times10^{-8}$	-
Type I collagen	0.25	0.2	$(1.8 \pm 0.5)\times10^{-7}$	$(6.8 \pm 2)\times10^{-9}$

Scattering and absorption at ω and $n\omega$ will affect the resultant harmonic signals. A stronger scattering coefficient will effectively decrease the measured value of $\chi^{(2)}$ and $\chi^{(3)}$. The skin and fat tissues have a larger scattering coefficient than the muscle tissue. Absorption of surfactants and internal absorbers may also alter the final signal which reaches the detector.

3.3.2 Polarization Dependence of SHG

In linear optics, if the incident electric field is linearly polarized along the z axis, the scattered light detected at a 45° angle with respective to the incident (y) direction in the x-y plane is proportional to the induced momentum $\bar{p}$ as[14]:

$$I_{scattered} \propto \bar{p}_z^2 \,\&\, \left(\bar{p}_x^2 + \bar{p}_y^2\right) \quad . \tag{3.1}$$

where $\bar{p}_z^2 = E^2\left[1/5\left(A^2 + B^2 + C^2\right) + 2/15(AB + BC + AC)\right]$,

$\bar{p}_x^2 + \bar{p}_y^2 = E^2\left[2/15\left(A^2 + B^2 + C^2 - AB - BC - AC\right)\right]$, $\bar{p}_x^2$, $\bar{p}_y^2$, $\bar{p}_z^2$ are the induced momentum, A, B, C are the polarizibilities along the principal axis, and the medium is a randomized molecular system.

The depolarization ρ_v is given by[14]:

$$\rho_v = \frac{\bar{p}_x^2 + \bar{p}_y^2}{\bar{p}_z^2} = \frac{2\left(A^2 + B^2 + C^2 - AB - BC - AC\right)}{3\left(A^2 + B^2 + C^2\right) + 2(AB + BC + AC)}. \tag{3.2}$$

We introduce $\alpha = 1/3\left(A^2 + B^2 + C^2\right)$, and $\gamma^2 = \left(A^2 + B^2 + C^2 - AB - BC - AC\right)$, where γ is the optical anisotropy and α is the spherical coefficient (isotropy) or the mean polarizability. ρ_v is given by:

$$\rho_v = \frac{6\ 45\left(\gamma^2\right)}{\alpha^2 + 4\ 45\left(\gamma^2\right)} = \frac{6\ 45x}{1 + 4\ 45x}, \tag{3.3}$$

where $\gamma^2/\alpha^2 = x$. For $x \geq 0$, $\Rightarrow \quad \frac{45\rho_v}{6 - 4\rho_v} \geq 0 \quad \Rightarrow \quad \rho_v \leq \frac{3}{2}$.

Polarization dependence in SHG has been used in many applications to extract the $\chi^{(2)}$ tensor coefficients and to interrogate structural symmetries both in homogenous and weakly scattering biological materials.[3,4,10] A typical measurement

uses a half wave plate and a polarizer to define the incident polarization which can be changed from S to P state. An analyzer in the signal beam path detects a pre-selected S or P component of the signal. The ratio of the P polarized second harmonic signal over its S polarized counterpart reflects on the symmetry condition of the system. Alternatively, the incident polarization can be changed continuously through a series of angles respective to one of the spatial coordinates. The signal analyzed parallel or perpendicular to that coordinate is used to deduce the symmetry property of the sample.

Under illumination of a polarized radiation E(r) at ω, the second order nonlinear polarization at 2ω is given by:

$$P^{(2)}(2\omega,r) = \sum_{j}\sum_{k}\beta_{ijk}(r)E_j(\omega,r)E_k(\omega,r), \tag{3.4}$$

where β is the hyperpolarizability of the molecular system, r is the spatial vector. The common symmetries found in biological tissues belong to the C_∞ and C_{2v} group. This leads to two non-vanishing hyperpolarizability coefficients β_{zzz} and β_{zxx}, and the coordinates of x, y, z are designated as z along the C (symmetry) axis, y along the normal of the interface and x perpendicular to y and z. Under these conditions, equation 3.1 can be reduced to[3]:

$$P_z^{(2)}(r) = \beta_{zzz}(r)\left[E_z(r)\right]^2 + \beta_{zxx}\left[E_x(r)\right]^2, \tag{3.5}$$

$$P_x^{(2)}(r) = 2\beta_{zxx}(r)E_x(r)E_z(r). \tag{3.6}$$

It has been shown by Fruend *et al.* that the polarized SH emission from the rat tendon reflected on the tendon's long axis as its polar axis with a C_∞ symmetry.[3] The

ratio of the P polarized SHG to the S polarized SHG in a dye labeled cell membrane was found to have a value above 10 regardless of the incident polarization change. This result concluded that reflection symmetry existed in planes perpendicular to the hemispherical bilayer .

Polarization measurement can be obscured by light scattering in a random medium. Photons lose their original polarization after multiple scattering, resulting in depolarization. In this study, the parallel and perpendicular (S,P or P,S) polarized SH components were analyzed respective to the incident (S and P) polarization in chicken tissues. Fig. 3.12 shows the polarized SHG spectrum from chicken tissues. The observed S-P or P-S intensity ratios I_{ss}/I_{sp}, I_{pp}/I_{ps} were ~ 1.65 (first and second subscripts denote the excitation and second harmonic signal polarizations respectively) which indicated that the SH signal oscillated slightly favoring the incident polarization state.

From Eq. (3.3), we have $\rho_v = \left[6/45\langle\gamma^2\rangle\right]/\left[\alpha^2 + 4/45\langle\gamma^2\rangle\right] \approx 1/1.65$, $\gamma \approx 2.76\alpha$, yielding a large anisotropy.[14,15] Fig. 3.13 shows the plot of the depolarization ratio ρ_v as the function of γ^2 and α^2. The depolarized SH signal agreed with the suggested overall randomness in tissue but to what level (microscopic or macroscopic) the randomness present depends on the specific tissue histology. A randomness on the molecular level would result in isotropic characteristics and lead to cancellation of the bulk SHG under the electric dipole approximation. In highly scattering tissues, depolarization can arise from both randomness and heterogeneity. The polarization state will be affected most for signals generated from below the surface. The harmonic light generated upon the first scattering is most likely to preserve the polarization state and structural symmetries.

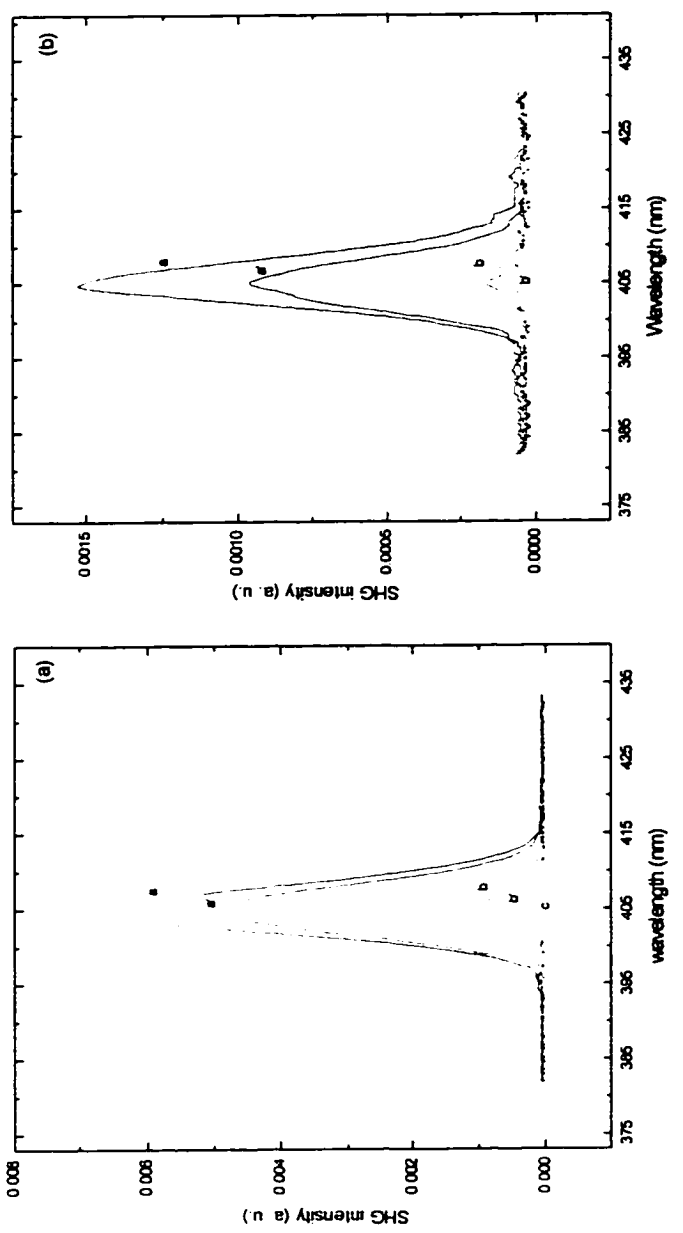

Fig. 3.12 Polarization dependence of SHG in chicken tissues. Graph (a): SHG under S polarized excitation. Curves a, b, and c stand for the S polarized SH components while curve a' and b' stand for the P polarized SH components from skin, muscle, and fat, respectively. Graph (b): SHG under P polarised excitation. Curves a and b stand for the P polarized SH components while curve a' and b' stand for the S polarized SH components from skin and muscle, respectively. c' was below the detection limit.

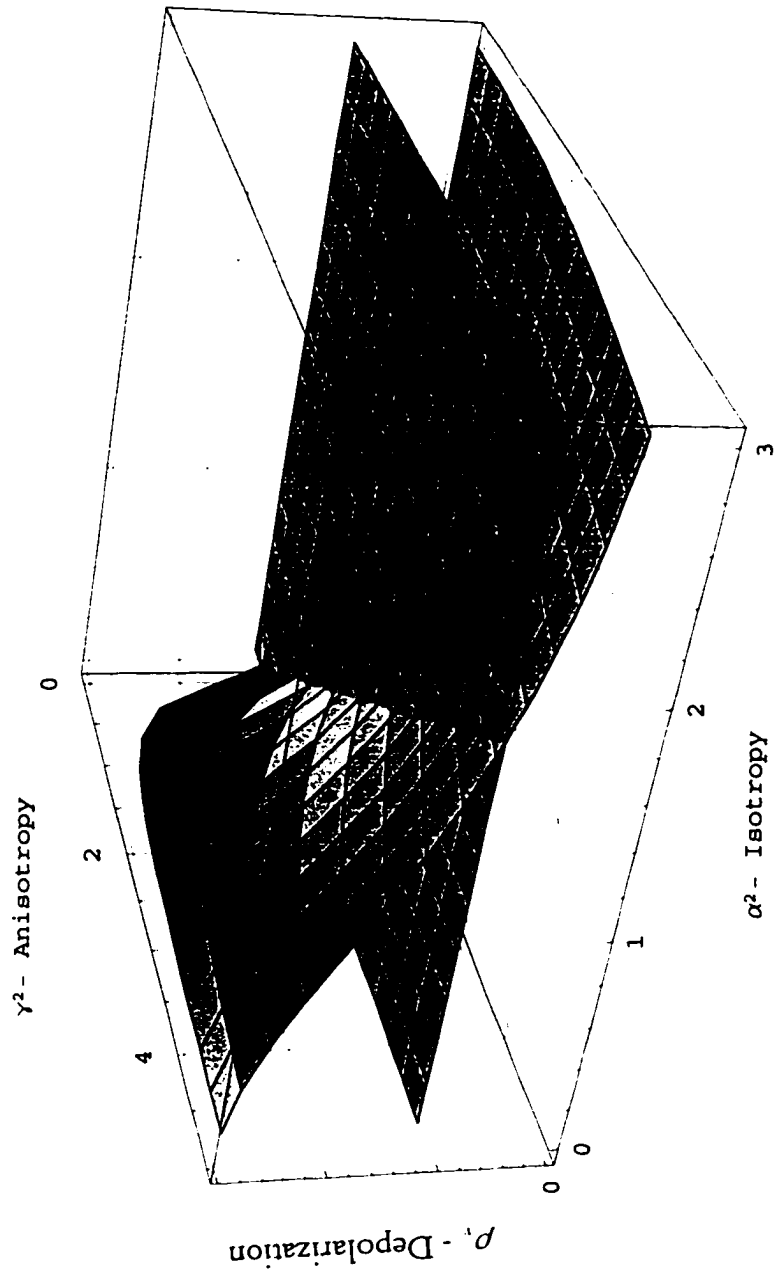

Fig. 3.13 Depolarization ratio ρ_v versus the anisotropy γ^2 and the isotropy α^2. The intersection indicates the depolarization ratio of 1.65.

3.3.3 Spatial Distribution and Angular Dependence of SHG

Fig. 3.14 demonstrates the experimental apparatus used for studying spatial distribution in model random and biological media. The setup is similar to that in Fig. 3.8, except a single lens and a CCD (charge coupled device) camera were used to image the light distribution in the focal area on the sample. Fig. 3.15 shows the resultant images obtained at both primary and harmonic wavelengths from a aluminum plate and a quartz powder sample. Figs. 3.15a and b show the primary light distributions of

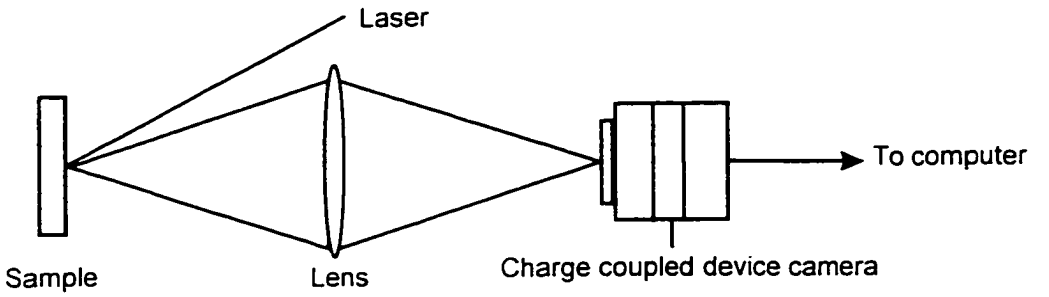

Fig. 3.14 Experimental setup of studying the spatial distribution of SHG.

the laser focus on an aluminum plate at 1064 nm and 532 nm, respectively. Figs. 3.15c and d show primary light distributions of the laser focus on the quartz powder sample at 1064 nm and 532 nm, respectively. Fig. 3.15e show the second harmonic light distribution of the quartz sample under 1064 nm laser excitation. Given a TEM_{∞} mode Gaussian beam profile, the spatial distribution of the fundamental and harmonic light can be readily calculated. Because the harmonic light depends on the square of the fundamental intensity, a narrower spatial width is expected at 2ω. The second harmonic light has a more pronounced scattering background as compared with the

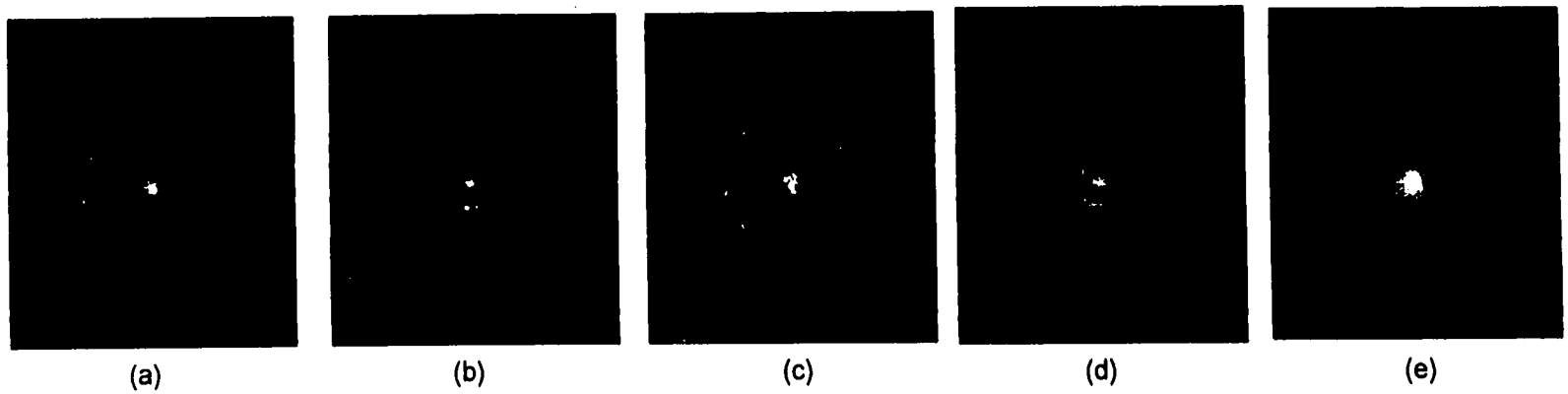

Fig. 3.15 Spatial distributions of the fundamental and second harmonic intensity in scattering media. (a) and (b), intensity distributions of the fundamental light in an aluminum plate at 1064 nm and 532 nm, respectively; (c) and (d), intensity distributions of the fundamental light in quartz powder at 1064 nm and 532 nm, respectively; (e), intensity distribution of the second harmonic light in quartz powder under 1064 nm laser excitation. A 8.8 cm focal length lens was used to focus the laser light. The fundamental light has an incident angle at 45° respective to the normal direction of the sample.

primary light in the quartz powder sample. The spatial distributions of 532 nm primary and 532 nm second harmonic light could be partially due to differences in the beam divergence at 1064- and 532 nm and chromatic aberration in the image optics. The outer ring structure observed around the immediate focus is likely to arise from scattering interference effect.

Kurtz *et al.* has shown that the angular distribution of SHG from a thin layer of KDP powders followed a radiation pattern similar to that from an isotropic planar radiator. The radiation can be described by Lambert's law:

$$I(\theta,\phi) = \int B \cdot ds(\cos\theta), \tag{3.7}$$

where B is the photometric brightness, ds is the surface element and θ and ϕ are the spherical polar angles.

A typical angular dependence of SHG for a tightly focused Guassian beam in highly scattering samples are illustrated in Fig. 3.16. The measurements have been conducted on a piece of white scattering paper and a quartz powder sample. The incident beam entrance angle was set at 45° from the normal direction of the sample. Due to the obstruction from the focusing optics, the measurement started at $> 50°$.

The salient feature of these observed backscattered light distribution is the quasi-uniform spatial profile as a function of the scattering angle. At harmonic wavelength, the spatial intensity profile deviated from the profile at fundamental wavelength with a faster decrease as the angle increased from the incident beam.

The angular dependence of SHG in a random medium is a function of the wavelength, the particle size, the coherence length, the nonlinear coefficient and focusing geometry. In particular, when the wavelength is on the order of the coherence

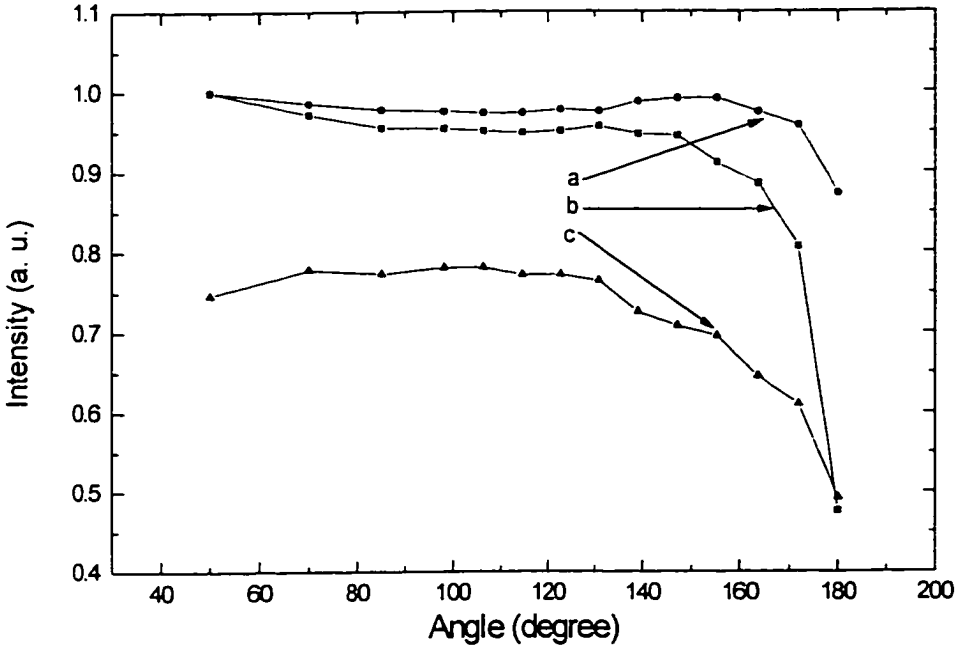

Fig. 3.16 Angular dependence of the scattered intensity profiles from (a) paper, (b) chicken muscle tissue at ω, and (c) from muscle tissue at 2 ω. The incident fundamental light entrance angle is set at 45°.

length, and smaller than the particle size, SHG can be constructively accumulated and a peak can be observed in the specular reflection direction. A second angular enhancement in the backscattered direction was predicted from the weak localization effect in SHG, involving interplay between disorder and optical nonlinearity.[16,17] The observed quasi-uniform distribution under a tight focus in this study is similar to the diffusion background discussed in Ref. 16 and Ref. 17.

References

1. J. M. Barrett, P. Abramoff, A. K. Kumaran, and W. F. Millington, "*Biology*", Prentice-Hall, Englewood Cliffs, N. J. (1985).
2. T. Ebe and S. Kobayashi, "*Fine Structure of Human Cells and Tissues*", John Wiley & Sons, New York, Igaku Shoin Ltd. Tokyo (1972).
3. I. Freund, M. Deutsch, and A. Sprecher, Biophys. J. **50**, 693 (1986).
4. Y. R. Shen, "*Principles of Nonlinear Optics*", John Wiley and Sons (1984), and the references therein.
5. J. J. Wynne and Bloembergen, Phys. Rev. **188**, 1211 (1969).
6. R. C. Miller and W. A. Nordland, Phys. Rev. **B2**, 4896 (1970).
7. S. K. Kurtz and T. T. Perry, J. Appl. Phys. **39**, 3298 (1968).
8. S. Fine and W. P. Hansen, Appl. Opt. **10**, 2350 (1971).
9. Y. Guo, P. P. Ho, A. Tirksliunas, F. Liu and R. R. Alfano, Appl. Opt. **35**, 6810 (1996).
10. O. Bouevitch, A. Lewis, I. Pinevsky, J. P. Wuskell, and L. M. Loew, Biophys. J. **65**, 672 (1993).
11. W. Denk, D. W. Piston, and W. W. Webb, "*Handbook of Biological Confocal Microscopy*", Plenum Press, New York (1995).
12. S. G. Schulman, "*Fluorescence and Phosphorescence Spectroscopy: Physiochemical Principles and Practice*", Pergamon Press, New York (1977).
13. R. F. Steiner and I. Weinryb, "*Excited State of Proteins and Nucleic Acids*", Plenum Press, New York (1971).
14. Contribution from Dr. Dana Calistru, Phys. Dept. of CCNY.

15. S. Bhagavantam, "*Scattering of Light and the Raman Effect*", Chemical Publishing Co., New York (1942).

16. K. M. Yoo, S. Lee, Y. Takiguchi, and R. R. Alfano, Opt. Lett. **14**, 800 (1989).

17. V. E. Kravtsov, V. M. Agranovich, and K. I. Grigorishin, Phy. Rev. B **44**, 4931 (1991).

Chapter Four

Two Photon Excitation of Fluorescence from Model Random Media and Biological Tissues

This chapter describes the two photon excitation of fluorescence spectral measurements in highly scattering animal tissues and fluorescent molecule samples over the wavelength region from 300- to 400 nm. The observed TPF signals from endogenous chromophores were found to carry quantitative information about the tissue systems. The results demonstrate the feasibility of using TPF to acquire optical and chemical properties of tissues for a deeper penetration depth to probe sublayer biological changes.

4.1 Two Photon Absorption (TPA)

Two photon absorption and two photon excitation induced fluorescence are two important NLO processes that have been extensively studied in various inorganic and organic media. The theoretical prediction of a two photon process was first given by Göppert-Mayer in 1931.[1] The experimental observation of TPA was demonstrated using strong monochromatic radiation generated from lasers.[2,3]

Two photon absorption refers to a nonlinear process in which the medium simultaneously absorbs two incident photons with energy $\hbar\omega$ to reach an excited state. TPA can be alternatively achieved by absorbing two incident photons at different frequencies ω_1 and ω_2, where the sum energy of $\hbar\omega_1$ plus $\hbar\omega_2$ equals to or is greater than that of the excited state.

The absorption constant α of a material is defined as[4]:

$$\alpha = \left\langle \frac{d}{dt} \frac{absorbed\ \ energy}{volume} \right\rangle \Big/ energy\ \ flux. \tag{4.1}$$

α can be expressed as a power series of the light intensity:

$$\alpha = \alpha^{(1)} + \alpha^{(2)} I + \alpha^{(3)} I^2 + ... \ , \tag{4.2}$$

where $\alpha^{(2)}$ is the two photon absorption coefficient. Two photon absorption coefficient depends on the incident intensity and has the unit of $cm \cdot W^{-1}$. The absorption constant under the EM wave radiation can be expressed as:

$$\alpha = \langle \vec{j} \cdot \vec{E} \rangle \Big/ I = \left\langle \frac{1}{2} \mathrm{Re}\left[\tilde{j}\tilde{E}\right] \right\rangle \Big/ I . \tag{4.3}$$

The current induced in the medium $\vec{j}$ is:

$$\vec{j} = \frac{\partial \vec{P}}{\partial t} + c\left(\nabla \times \vec{M}\right) - \frac{\partial}{\partial t}\left(\nabla \cdot \vec{Q}\right) + ... \ . \tag{4.4}$$

The second and third terms on the right hand side of Eq. (4.4) from $\vec{M}$ and $\vec{Q}$ represent the magnetic dipole and electric quadruple contributions. These two terms can be neglected under the electric dipole assumption.

The third order nonlinear polarization at ω_1 is given by:

$$P_{NL}^{(3)}\left(\omega_1\right) = \chi^{(3)}\left(\omega_1 \omega_2 - \omega_2\right) E_1 E_2 E_2^* , \tag{4.5}$$

Considering the two photon absorption of a beam at ω_1 with the presence of a beam at

ω_2, the contribution to j from the third order nonlinear polarization is given by:

$$j = \partial P/\partial t = -i\omega_1 \chi^{(3)}(\omega_1\omega_2 - \omega_2) E_1 E_2 E_2^* e^{-i\omega_1 t} \quad . \tag{4.6}$$

Therefore,

$$\left\langle \frac{d}{dt} \frac{absorbed\ \ energy}{volume} \right\rangle = \frac{1}{2} \mathrm{Re}\left[-i\omega\chi^{(3)} E_1 E_1^* E_2 E_2^* \right]. \tag{4.7}$$

From Eq. (4.3), the absorption coefficient is:

$$\alpha(\omega_1) = \alpha^{(2)} I_2 = (4\pi\omega_1 / c)\,\mathrm{Im}\,\chi^{(3)}(\omega_1\omega_2 - \omega_2)|E_2|^2 . \tag{4.8}$$

The two photon absorption coefficient is:

$$\alpha^{(2)} = (32\pi^2\omega_1 / c^2)\,\mathrm{Im}\,\chi^{(3)}(\omega_1\omega_2 - \omega_2). \tag{4.9}$$

The TPA coefficient $\alpha^{(2)}$ is linearly proportional to the imaginary part of $\chi^{(3)}$. Theoretical derivation using second order perturbation theory by Göppert-Mayer[1] and later by Shen[5] has also verified that two photon absorption is a third order nonlinear optical process.

Multiphoton absorption has been formally described by quantum mechanical time dependent perturbation theory.[2,7] The probability of a radiation induced transition for a molecule going from an initial state ψ_a to a final excited state ψ_f is given by[5,6,7]:

$$W_{0\to f} = (2\pi/\hbar)\left|\langle f|M|0\rangle\right|^2 \rho^{n}(E) d^{n-1}E , \tag{4.10}$$

where ρ is the density state of photons, M is the n^{th} order matrix element, and E is the energy.

The physical process of a single- or multi-photon transition in a molecule can be viewed through time ordered Feynman diagrams. Different types of two photon processes are illustrated by Feynman and their corresponding Jablonski diagrams shown in Fig. 4.1. In Fig. 4.1c, a two photon transition takes molecules directly from state ψ_n to ψ_f via the Hamiltonian of the vector potential product in the first order perturbation, and directly connects states of different parity in the next higher order approximation. In Fig. 4.1d and e, TPA is achieved via the intermediate state ψ_n. This intermediate transitional process happens on an extremely fast time scale, approximately on the order of 10^{-16} sec via a virtual state. The initial and final states of same parity are connected.

It is known that the eigenfunctions of molecules having a center of inversion symmetry possess a definite parity, and the states can be further divided into symmetric g (gerade) and unsymmetric u (ungerade) states. Single photon absorption (SPA) is limited to $g \rightarrow u$ and $u \rightarrow g$ transitions, since an allowed one photon transition $(0 \rightarrow f)$ implies a nonvanishing integral of $\int \psi_f^* r \psi_n d\tau$. Two photon absorption is not limited by this selection rule. Fig. 4.2 shows an example of a two photon transition via the intermediate state in an anthracene molecule. In the final state B_{2u} of anthracene, $y\psi_f$ is symmetric while $x\psi_f$ is unsymmetric. Based on the parity concern, $\int \psi_f y \psi_n d\tau \neq 0$ and $\int \psi_f x \psi_n d\tau = 0$. To satisfy a nonvanishing integral of $\int \psi_f r \psi_n d\tau$, the B_{2u} state can only be excited by light which is polarized along the y axis through a single photon transition. It turns out that the anthracene molecule does not have an axis by which the integral is nonvanishing in the B_{1g} state. Thus single photon absorption from A_{1g} to B_{1g} is forbidden. In this case, a two photon transition

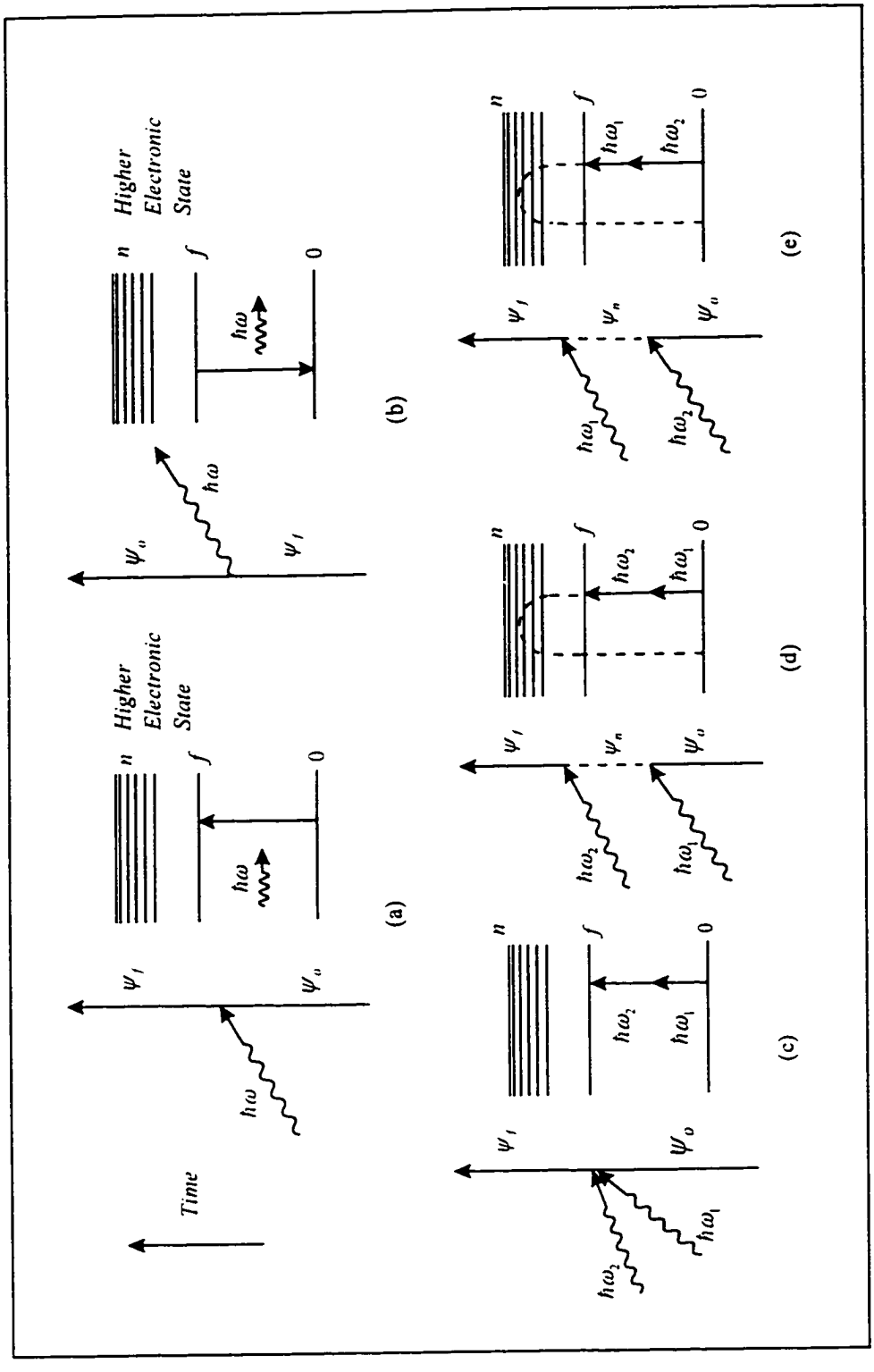

Fig. 4.1 Time ordered Feynman diagrams and Jablonski diagrams of one- and two-photon excitation processes: (a) single photon absorption, (b) single photon emission, (c) direct two photon absorption, (d) and (e) two photon absorption through intermediate states.

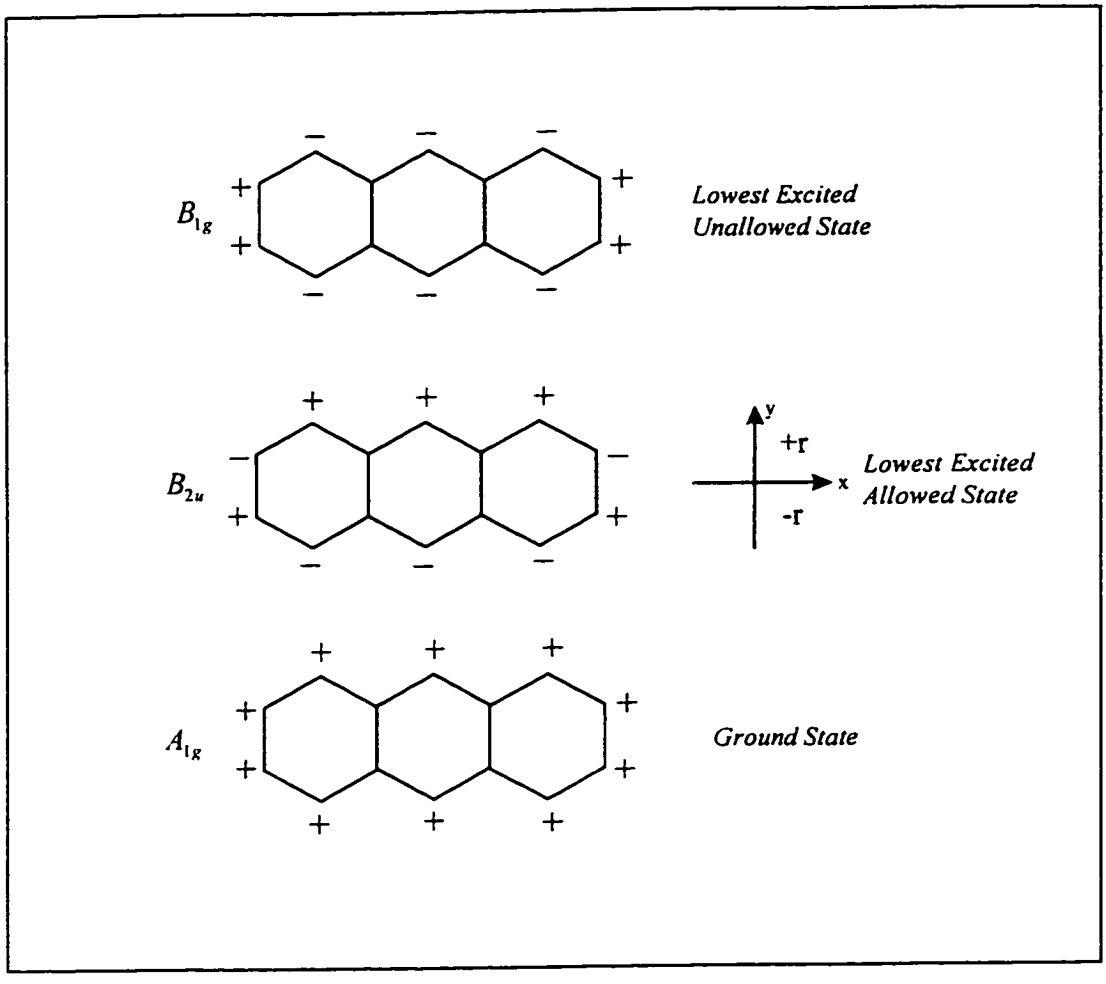

Fig. 4.2 The ground and first excited ungerade and gerade states of an anthracene molecule.

can be mediated via an intermediate state which may be considered as a mixture of all the one photon allowed u states. The parity can be altered during the transitional change from the intermediate state to the final state so that both initial and final states of the same parity can be connected. Theoretical and experimental investigations have shown that this type of two photon transition (shown in Figs. 4.1d and e) predominates in most cases. Direct transition shown in Fig. 4.1c is of minor importance since it only connects a state with itself in the dipole approximation.

If the molecule does not have a center of inversion symmetry, then the states can not be classified as symmetric or unsymmetric, and all the final excited states may be both one and two photon allowed. It should be pointed out that selection rule in parity allowed transitions can be compromised by vibronic coupling mechanisms. Besides parity, the electronic spin is another determinant which requires conservation of the spin angular momentum. The electronic states that are designated as S_i (for singlet states) have parallel electron spin and T_i (for triplet states) have anti-parallel electron spin. Single- and two- photon excitations follow different spin selection rules, and it is possible to flip the spin direction with a two photon mode to form a transition that is forbidden in a single photon event. In general, parity, spin and symmetry restrictions should be considered in combination to determine a final electronic transition.

The intensity equation governed by TPA in a homogenous and nonscattering medium can be expressed as[5]:

$$\frac{dI}{dz} = -\alpha I , \tag{4.11a}$$

$$\alpha = \alpha^{(2)} I , \tag{4.11b}$$

$$\frac{dI}{dz} = -\alpha^{(2)} I^2. \tag{4.11c}$$

The solution for Eq. (4.11c) has the form:

$$I(z) = I_o / \left(1 + \alpha^{(2)} I_o z\right), \tag{4.12}$$

where I_o is the incident light intensity at z=0, and $I(l)$ is the transmitted intensity at $z = l$.

The calculated solution of $I(l)$ is plotted in Fig. 4.3 together with SPA for comparison. The hyperbolic decay of light transmission under TPA is quite different from that in SPA as $I(l) = I_o e^{-\alpha l}$. In the limit of large $\alpha^{(2)} I_o l$, the transmitted intensity in TPA approaches the asymptote of $1/\alpha^{(2)} l$, which is independent of the incident intensity. This property is in contrast to SPA, in which the transmission always is linearly dependent upon the incident intensity and decreases exponentially with the propagation distance.

Two photon absorption coefficient $\alpha^{(2)}$ and cross section σ_{TPA} are two key parameters. $\alpha^{(2)}$ depends on the laser intensity I or photon flux F ($F = I/\hbar\omega$), where F has the unit of photons/cm^2·sec. It is more convenient to use σ_{TPA}/F as a parameter to characterize two photon absorption. Some researchers define $\delta_{TPA} = \sigma_{TPA}/F$ as the TPA cross section, which in fact is the ability of a molecule to form a two photon transition. The unit of δ_{TPA} is cm^4 sec/($photon \cdot molecule$), and it is independent of the incident photon flux or intensity, concentration, and path length.

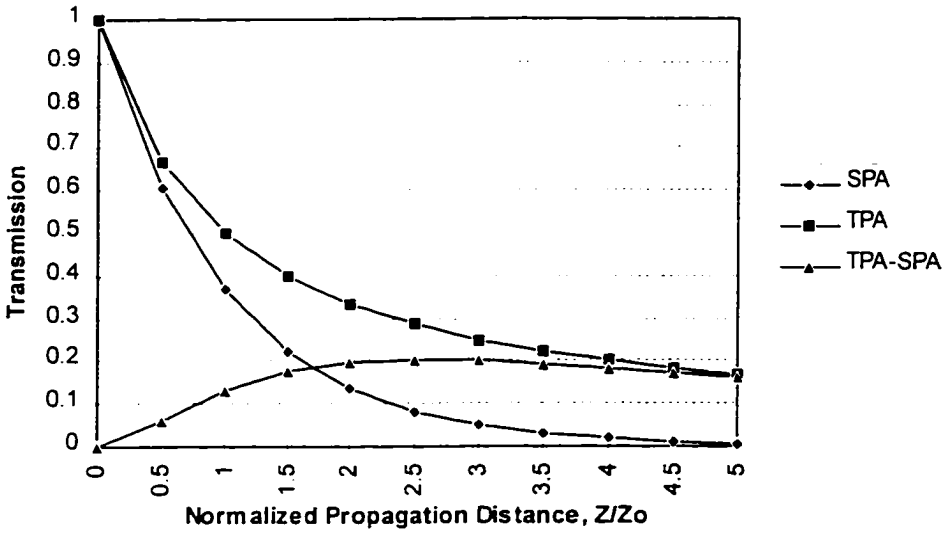

Fig. 4. 3 Transmission under SPA and TPA over normalized distance $z_n = \alpha^{(2)} I_n$.

Table 4.1 Experimental δ_{TPA} values of dye and fluorescent media.

Material	$\delta^{u}_{TPA} \times 10^{-50}$ [a]	Wavelength (nm)
Rhodamine B	14[b]	1064
Rhodamine 6G	3.6[b]	1064
Fluorescein	0.23[c]	1050
Coumarin 307	19 ± 5.5[b]	776
Anthracene	4.3[c]	694
NADH/NADPH[e]	1.5×10^{-2} [d]	700
FMN[f]	0.83 [d]	700

[a] The unit is cm^4·sec/photon. It is defined that 1GM (Göppert-Mayer) = 10^{-50} cm^4·sec/photon.
[b] Ref. 8.
[c] Ref. 9.
[d] Ref. 10.
[e] NADH/NADPH: reduced pyridine nucleotide.
[f] FMN: Flavin mononucleotide.

$\alpha^{(2)}$ and δ_{TPA} is related by $\alpha^{(2)} I = \sigma_{TPA} N = \delta_{TPA} NF$, where N is the concentration. It has been shown that δ_{TPA} is strongly polarization dependent even in randomly oriented medium.[6] In practice, the polarization dependence and excitation spectra are used to determine the symmetry properties of the excited states.

Table 4.1 lists some of the measured values of δ_{TPA} in several dye and fluorescing materials. As evident from this table, the magnitude of δ_{TPA} is extremely small, usually on the order of 10^{-70} - 10^{-49} cm^4 sec/*photon* compared to a general value of one photon absorption cross section of 10^{-16} - 10^{-22} cm^2, thereby implying the requirement of a very intense laser excitation typically on the order of $I \sim 10^9$ W/cm^2 or F ~ 10^{22} photons/cm^2·sec to observe a two photon transition.

Several important properties of TPA are summarized as follows:

1) TPA and SPA follow different selection rules. SPA occurs between states of opposite parity, whereas TPA occurs between states having the same parity. TPA can excite transition that is forbidden in SPA.

2) TPA is a third order nonlinear optical resonant process. TPA absorption cross section σ_{TPA} is proportional to the incident intensity and its transition probability or transition rate is proportional to the square of the incident intensity.

3) TPA requires energy exchange between the excitation light and the medium. A linear dependence on Im $\chi^{(3)}$ leads to the damping of optical field propagating inside the medium.

4.2 Two Photon Excitation of Fluorescence (TPF) from Biological Media

4.2.1 Photophysics of Two Photon Excited Fluorescence

Once the molecules are raised to the excited state through a two photon absorption, the energy can be dissipated through different conventional mechanisms such as fluorescence, phosphorescence, hot luminescence, Raman and internal conversion. Fig. 4.4 illustrates the photophysics of a typical molecular system returning from an excited state to the ground level under two photon excitation.

Fluorescence describes the spontaneous process of photon emission on a nanosecond time scale. As discussed in section 4.1, if both one- and two-photon transitions reach the same final state, their resultant fluorescence emissions and intensity decays would be indistinguishable. When exciplex and excited species are formed, or a different final state is reached, TPF spectra may exhibit significantly different characteristics compared with the single photon excited fluorescence (SPF). Because most key fluorescent chromophores in native tissues lack a center of inversion symmetry and

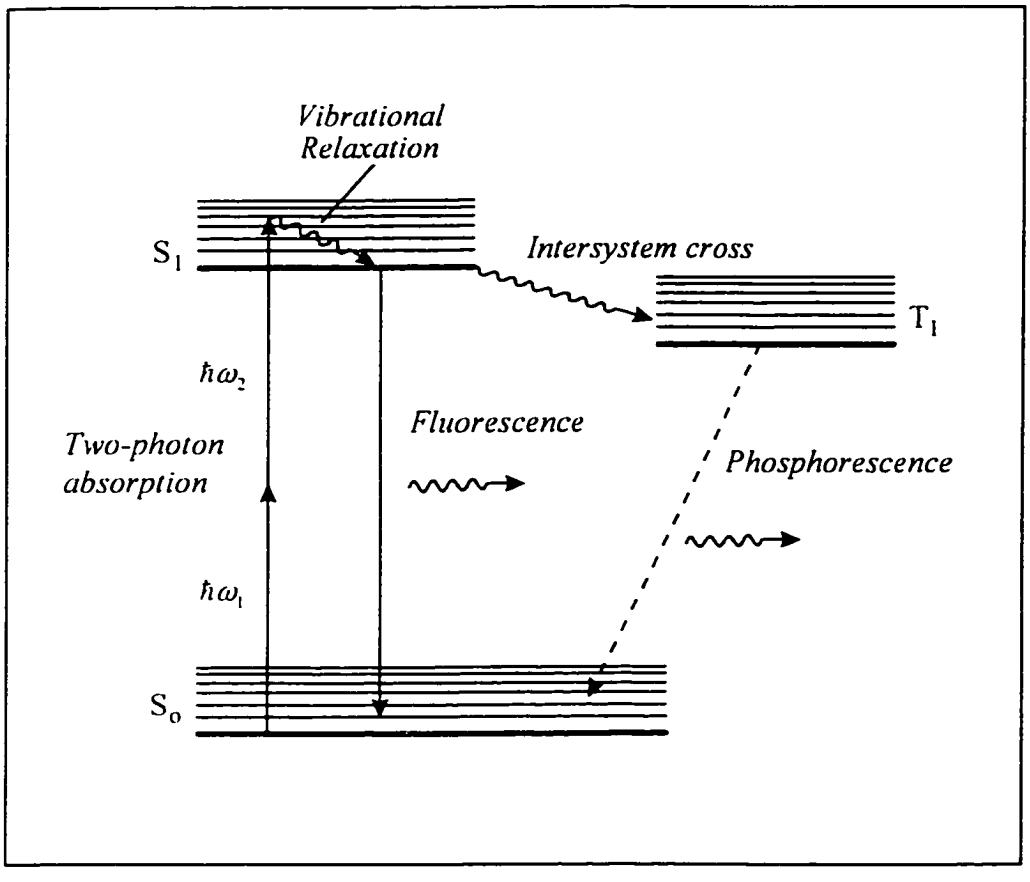

Fig. 4.4 Two-photon excitation induced processes in Jablonski diagram. By absorbing energies of two incident photons the molecule undergoes electronic transition from the ground state S_o to an excited singlet state S_1. After absorption, internal relaxation happens within S_1. Then, radiative and non-radiative decays take place from S_1 to S_o, and the rate is controlled by the excited state lifetime. The radiative decay is known as fluorescence. Inter-system crossing to a triplet state T_1 results in another radiative relaxation to the ground state known as phosphorescence.

consequently have no parity designation, they exhibit similar spectra of fluorescence emission under both one- and two-photon absorption.

4.2.2 Theory of Two Photon Excitation Induced Fluorescence

The TPF fluorescent rate under a quadratic intensity dependence can be estimated by:

$$\frac{dS}{dt} = \frac{1}{2} Q N \delta_{TPA} F^2 , \tag{4.13}$$

where dS/dt is the number of fluorescent photons generated per unit time, Q is the quantum yield, and N is the number of fluorophore or concentration. The factor of $1/2$ indicates that two photons are required to accomplish a single event.

For a laser flux of $F = 10^{25}\, photon \cdot cm^{-2}\, \sec^{-1}$ or $I \approx 1$ GW/cm^2, a dye molecule with a two photon cross section of $\delta_{TPA} = 10^{-51} cm^4 \cdot \sec \cdot photon^{-1} \cdot molecule^{-1}$, a quantum yield of Q=0.01, and the number of fluorophore at $N = 10^8$, will yield a $dS/dt \sim 5 \times 10^4$ *photons/sec.*

Equation (4.13) shares some resemblance to the single photon induced fluorescence rate $dS_1/dt = QNI\delta_{SPA}F$, which depends linearly on the incident photon flux, and δ_{SPA} is the single photon absorption cross section. The quadratic dependence of TPF on F or I is an important characteristics, but can be altered due to quenching, photo-bleaching, saturation and stimulated emission from the excited state to a highly excited vibrational ground level.[11] In addition, the temporal and spatial distributions of the incident photon flux have a direct impact on the final TPF output. The total number of photons in a TPF signal is given by:

$$S = \frac{1}{2} Q N \Phi p \delta_{TPA} \int_0^\infty \int_0^\infty F^2(r,t) dr dt \,, \tag{4.14}$$

where ϕ is introduced as the collection efficiency that depends on the experimental apparatus and geometry. p is the repetition rate of the laser pulse. The temporal and spatial dependence has been treated by separating F into a time and a spatial function in the form of $F(r,t) = F_1(t) \cdot F_2(r)$. Under the assumption of a Gaussian distribution, the averaged fluorescence photon flux is given by[9]:

$$\langle s \rangle = \Phi Q N \delta_{TPA} g^{(2)}(n\pi / \lambda) \langle P(t) \rangle^2 \,, \tag{4.15}$$

where $g^{(2)}$ is the second order temporal coherence function, and P(t) is the averaged power of the incident light.

TPA cross section δ_{TPA} can be obtained through a prior knowledge of the ratio of single- and double-photon fluorescent rates. Assuming an identical quantum efficiency and experimental setup in both one- and two-photon measurements, δ_{TPA} can be deduced from[12]:

$$\delta_{TPA} = 2 \frac{(ds_2 / dt) N_1 \delta_{SPA} F_1}{(ds_1 / dt) N_2 F_2^2} \,, \tag{4.16}$$

where the suffix denotes the single and double photon parameters.

4.2.3 TPF Study in Biological Tissues

TPF spectral lineshape and relaxation dynamics can be used to extract valuable information for determining the electronic structure and TPA cross section of molecules.[8-10] In biological cells and tissues, two photon spectroscopy offers advantages

over its SPF counterpart in a deeper penetration depth, reduced background interference, and less photo-bleaching or damage for studying biological functions and structures.[13] Because most absorption bands of fluorophores lay in the UV region, probing methods based on SPF are often hampered by cyto-toxicity problems. It is desirable to use the visible and near infrared wavelength window through multi-photon excitation to avoid the problem. Visible or near infrared light generates less photo-bleaching and penetrates deeper into scattering tissues. TPF is therefore a sensitive approach to access and monitor subsurface physical and chemical changes.[13]

Over the past two decades, fluorescence emissions from native biological tissues has been studied using single photon UV excitations.[14,15,16] The key endogenous fluorophores which show useful diagnostic properties include tryptophan, collagen, elastin, NADH, flavin and porphrins. It has been demonstrated that the emission signature and intensity ratio at 340 nm and 450 nm of SPF from these native fluorophores can be used as optical fingerprints to distinguish between diseased and normal tissues.[14,15,16] One may extend this single photon "fluorescence pathology" to a multi-photon mode in which a deeper penetration depth could further enhance the ability to detect cancer and other diseases. The fluorescence signal from native fluorophores is important in many sensitive situations where the interaction between the extrinsic agent and the tissue component may cause unwanted changes in the state of the tissue. For potential *in vivo* screening, it is impractical to chemically stain organs with a large area, and it often requires different dyes to label and probe in different cellular and molecular environments. Based on these considerations, TPF spectral measurement will serve as an important first step in the further development of nonlinear optical biopsy modalities based on multiphoton fluorescence approaches.[13]

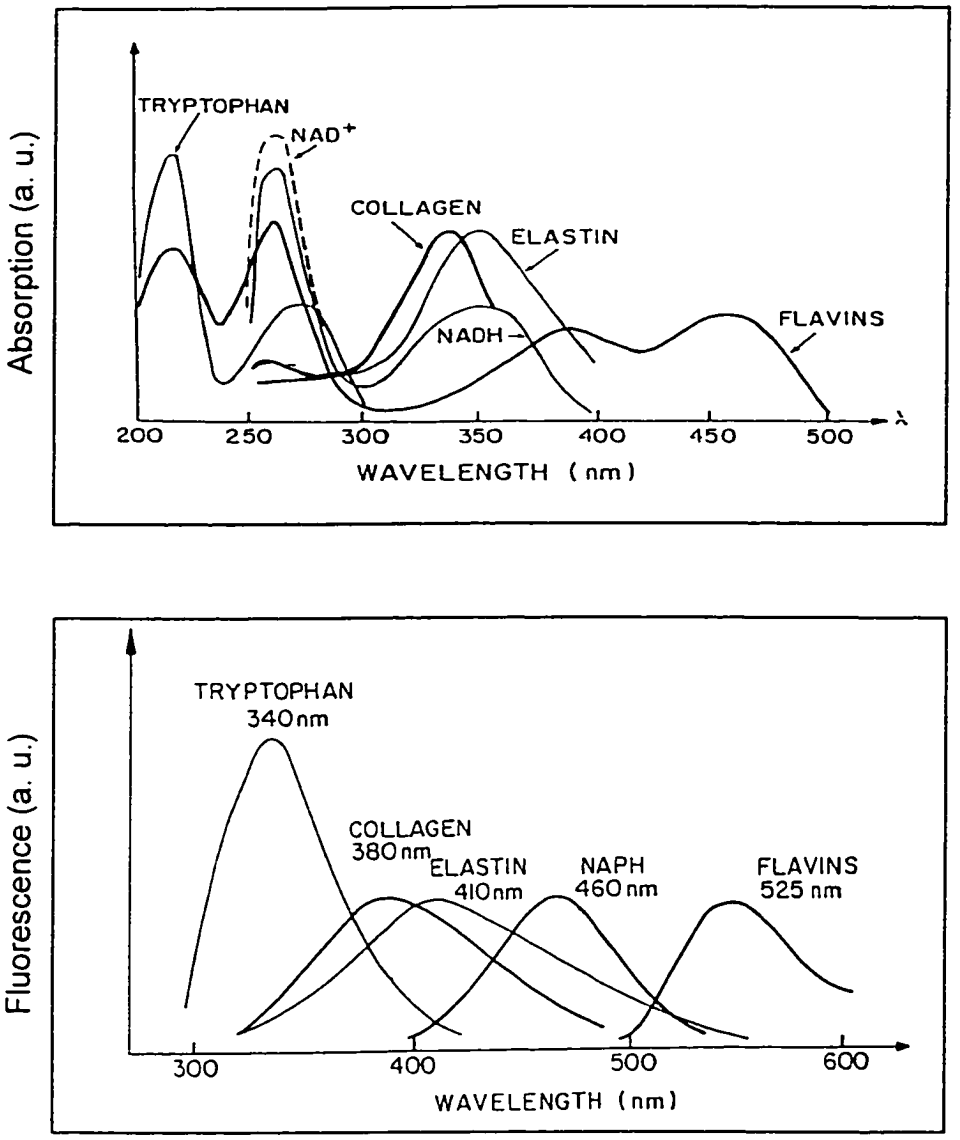

Fig. 4.5 Absorption and fluorescence spectra of key fluorophores in tissues.

After Ref. 15, Wenling Sha Glassman, CCNY.

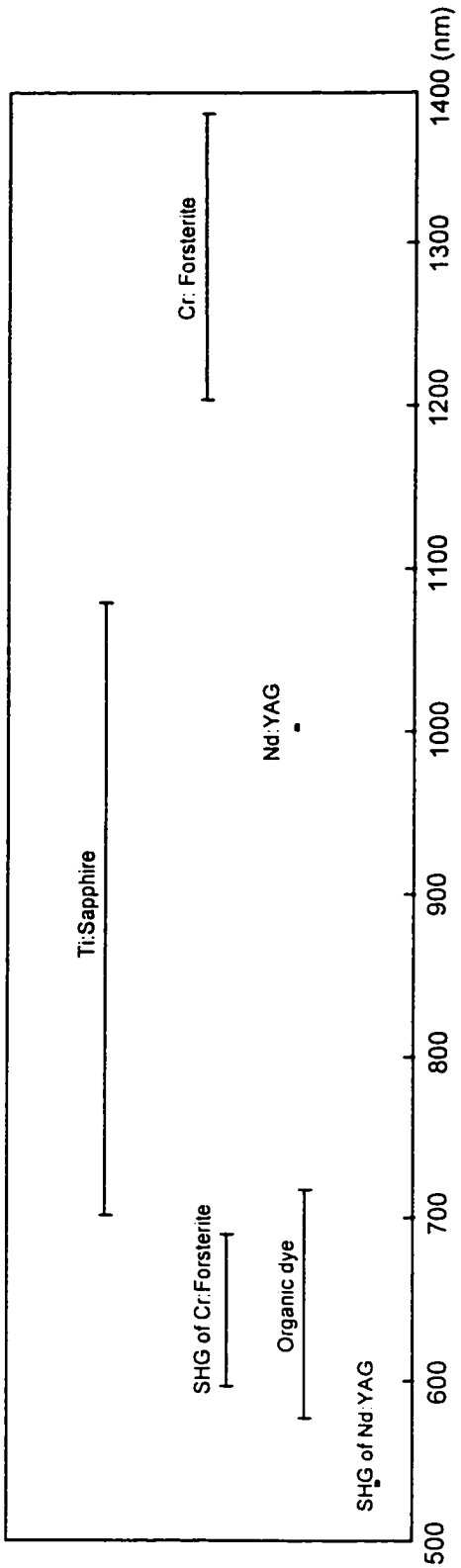

Fig. 4.6 Typical wavelength span of major commercially available lasers for two photon excitation of key tissue fluorophores. The arrows correspond to wavelengths about the peak positions in the absorption bands.

4.3 Experimental Methods and Samples

The experimental arrangement for spectral TPF measurement is shown in Fig. 4.7. The output of a colliding pulse mode locked laser was synchronously amplified by a copper vapor laser pumped sulphur Rhodamine dye amplifier. Pulses of 100 fs at 625 nm wavelength were obtained with a repetition rate of 6.5 kHz. The incident light was directed by a beam splitter onto the sample through a 27X-UV microscope objective lens to achieve chromatic aberration correction and a tight focus. The back-scattered TPF signal was collected by the same objective lens, transmitted through the beam splitter and then analyzed by a spectrometer. A photomultiplier tube and a computer controlled lock-in amplifier were used to record the data. A long pass filter ($\lambda > 550$ nm) was inserted in the input beam path to eliminate possible contribution from the laser cavity. A short pass filter ($\lambda < 450$ nm) was placed in front of the entrance slit of the spectrometer to block the fundamental scattering. The average power at the sample site was estimated to be $\sim < 1$ mW. For comparison, the single photon excited fluorescence measurement was performed using a CD-Scan unit (Mediscience Technology Corp.), shown in Fig. 4.8. A Xenon lamp was used as the illuminating source. The excitation light was delivered through a step motor controlled grating and a fixed slit and then focused onto the sample surface at a grazing angle of 30°. The emitted light was collected at -60° through the emission monochromator followed by a photomultipier tube. Wavelength dependence correction was achieved by a monitoring signal from a separated PMT and computer software.

TPF measurements have been performed on animal tissues. Frozen and thawed muscle, skin and fat native chicken tissues were placed in plastic cuvettes with a front opening section (5 × 10 mm) to directly expose the specimen under the laser excitation.

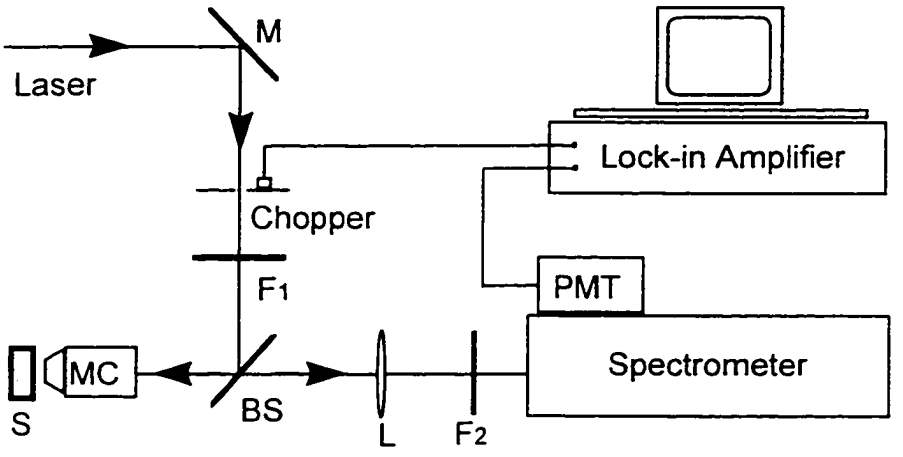

Fig. 4.7 Experimental setup for TPF spectral measurement. M is a mirror, BS is a dichroic beam splitter, MC is a UV microscope objective lens, S is the sample, L is a lens, F_1 and F_2 are long and short pass filters, respectively.

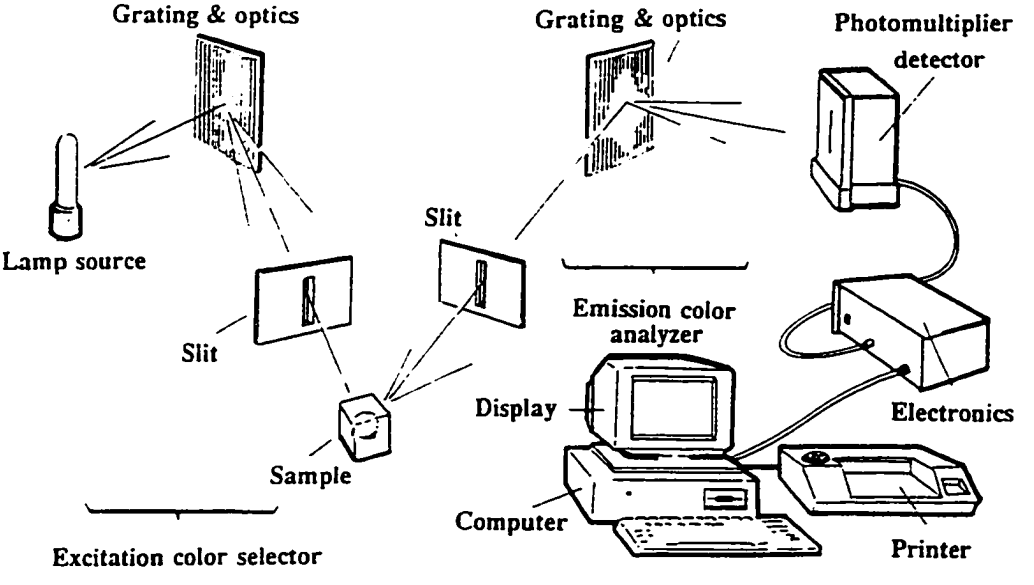

Fig. 4.8 Instrumentation arrangement of CD-Scan Unit for single photon excitation of fluorescence measurements. (Mediscience Corp.)

After Leming Wang, CCNY.

Purified fluorescent molecule powders of tryptophan, tryosine, and phenylalanine were investigated using the same experimental apparatus.

4.4 Results and Discussion

The key issues investigated in this TPF study included fluorescence spectral profile, emission strength, power squared intensity dependence, spectra-structure dependence, and self-absorption and scattering effects. The TPF emissions were measured between the wavelength region of 300 - 400 nm. Figs. 4.9 a, b, c present the typical TPF spectra obtained from muscle, skin and fat chicken tissues, in which SHG signals have been simultaneously observed. The narrow peak at half of the laser wavelength in Fig. 4.9 is SHG, while the following broad contour is the TPF signal. The FWHM widths of SHG and TPF spectra indicate the respective temporal or coherent characteristics in these two NLO processes.

The emission strength of TPF intensity was found to be different in the three examined structures. The strongest TPF signal was generated from the muscle, followed by signals from the skin and fat tissues. Consistent differences in emission strength were also confirmed by the single photon fluorescence spectra between muscle and skin, as shown in Fig. 4.10. These results suggest that muscle tissue is more fluorescent than skin and fat tissues between 320 to 370 nm. A more pronounced difference in emission strength has been observed in SPF between skin and fat tissues. In addition, noticeable spectral shift in the peak positions was also found in the TPF spectra. For muscle and skin tissues, the emission peaks at ~345 nm, while the maximum emission location (not as conspicuous) of fat is approximately at 360 nm.

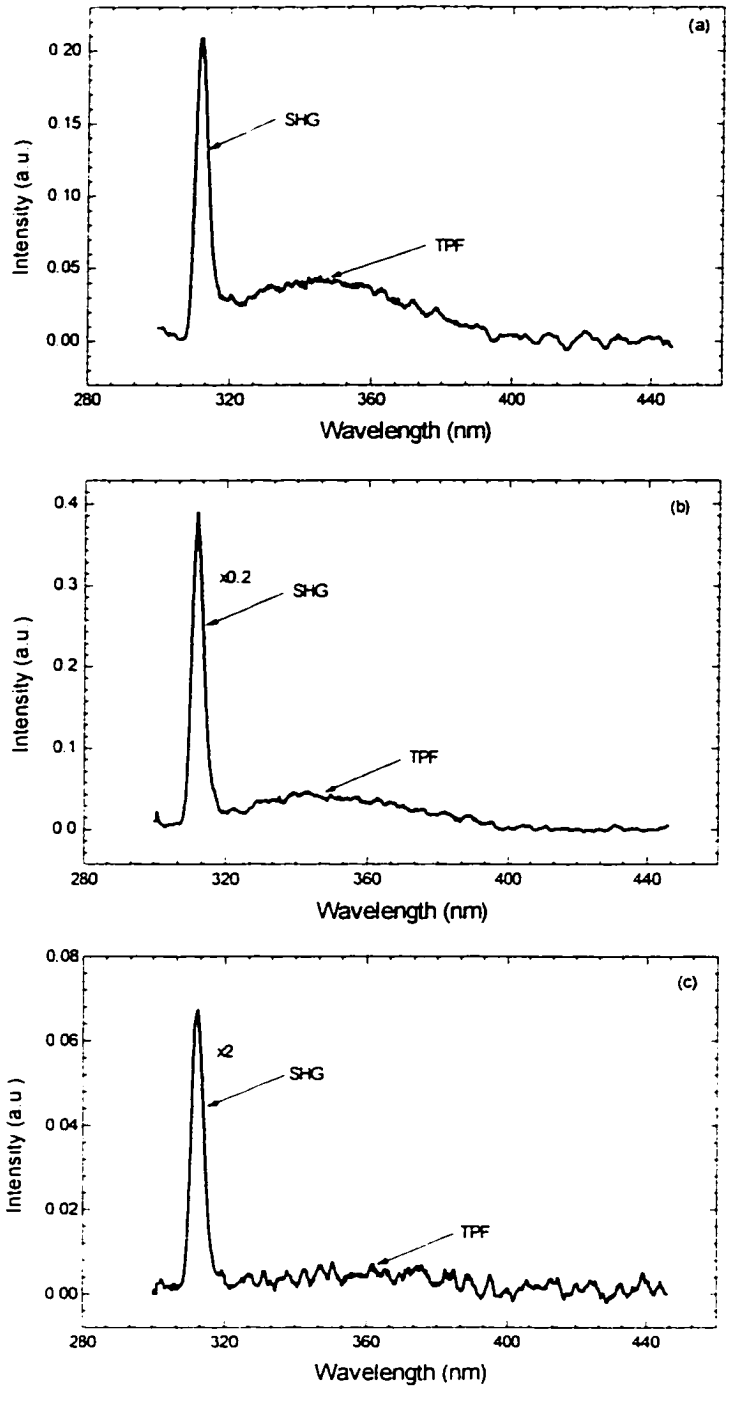

Fig. 4.9 TPF spectra of (a) muscle, (b) skin and (c) fat chicken tissue under 625 nm, 100 fs laser excitation. The incident power is ~1mW.

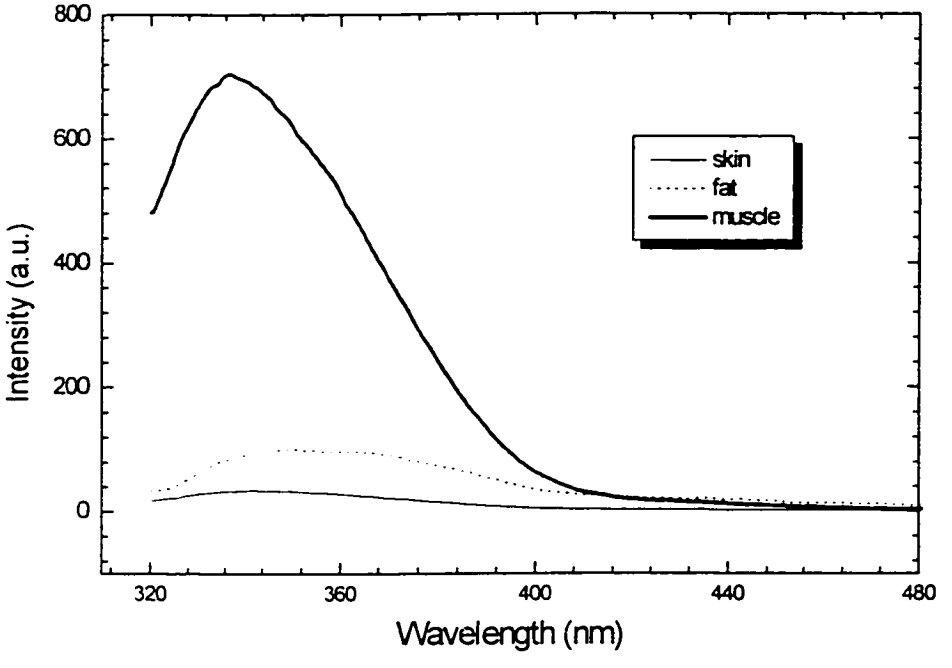

Fig. 4.10 Single photon excitation of fluorescence spectra of chicken skin, fat and muscle tissues under 300 nm lamp excitation.

These salient features of spectral shape and emission differences are connected to the structural and chemical content variations.

One of the most characteristic differences between TPF and SPF is their signal dependence on the excitation intensity. To investigate the intensity dependence, the TPF signals were examined by changing the incident light using neutral density optical filters. The fitted slope of a log-log plot of the TPF signal versus incident intensity is 1.96 ± 0.5, as shown in Fig. 4.11, which confirms the nature of a two photon excitation process ($I_{fluo} \propto I_{in}^2$). The measured TPF emission from powder tryptophan particles is shown in Fig. 4.12, in which the signal strictly follows to a power squared dependence. The peak emission is approximately at 330 nm.Tryptophan (Trp), Tyrosine (Tyr) and Phenylalanine (Phe) are the three major amino acids that fluorescence in the UV region between 200 - 400 nm. They are the building blocks in various types of proteins. Most protein molecules do not fluorescence due to the non-rigid skeleton leading to a large freedom of vibration and energy dissipation through non-radiative relaxations. By contrast, aromatic amino acids were found to strongly fluorescence owing to the electronic configuration of the delocalized π conjugation structure of the indole ring. The quantum efficiency of these molecules can be as high as close to 50%, depending on the pH value and temperature of the local environment. The emission band around 340 nm has been attributed to tryptophan residues attached to the proteins in native tissues.[17-19] The absence of emission from Tyr and Phe is due to the fact that when tyrosine and phenylalanine present together with tryptophan, the fluorescence from the former two will be quenched by absorption of Trp and energy transfer.

The fluorescence of tryptophan is a dependent on environmental variations such as polar solvent interaction and protein conformational changes.[17-19] The TPF

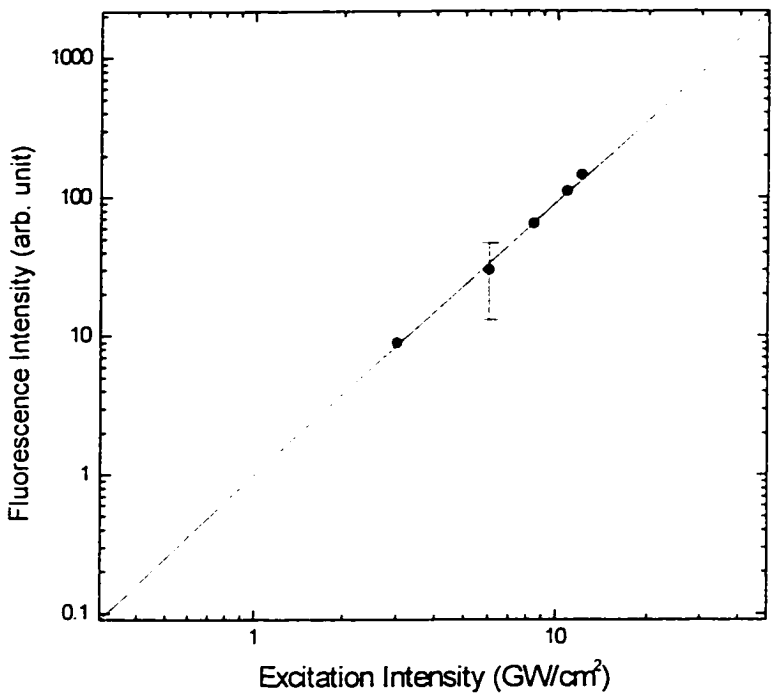

Fig. 4.11 TPF intensity versus excitation intensity of chicken muscle tissue. The log-log fitted slope is 1.96 ± 0.5.

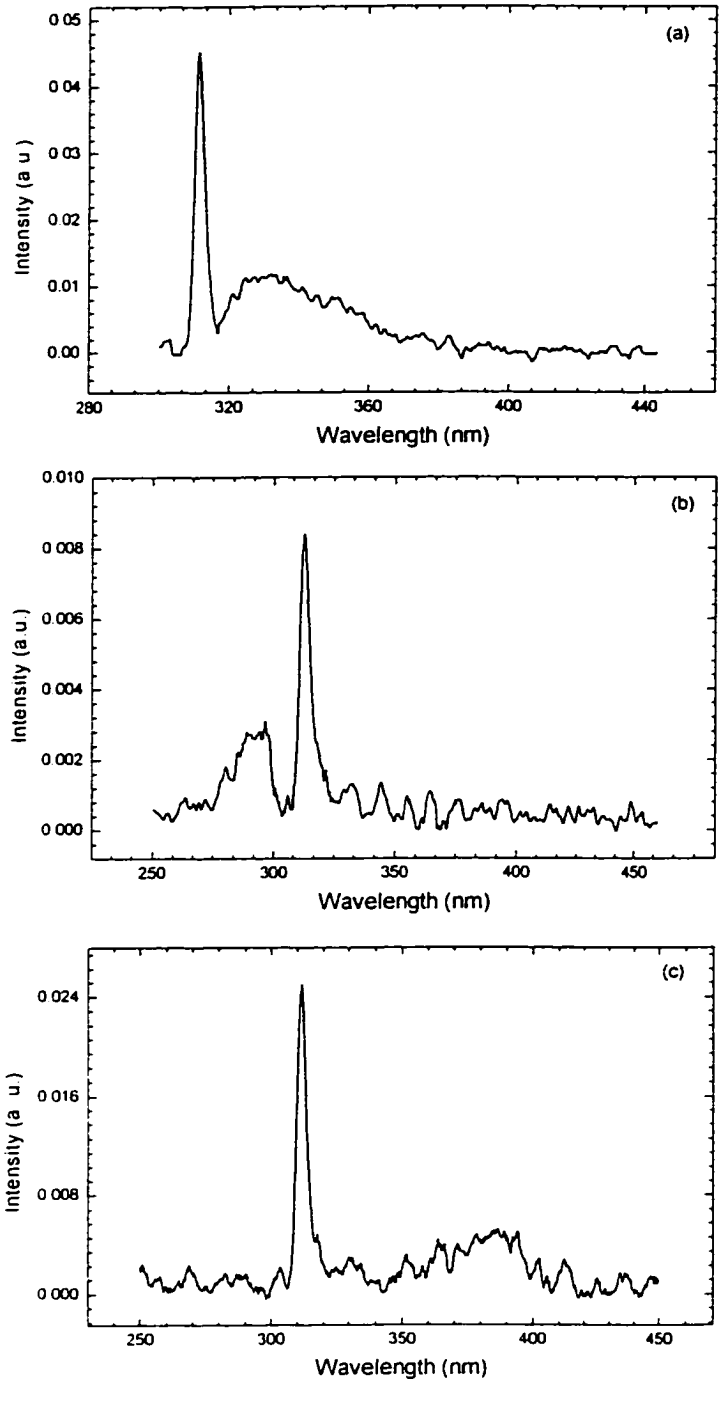

Fig. 4.12 TPF spectra of (a) tryptophan (b) phenylalanin and (c) tyrosine powder particles under 625 nm, 100 fs laser excitation.

spectra of tryptophan in aqueous and solid states were found to closely resemble each other except for the spectral shift.[18] The resemblance of TPF from muscle chicken tissue and tryptophan powder is fairly close as shown in Figs. 4.9 and 4.12. Spectral peak location deviation from tissue to tryptophan powder is expected due to environmental variation. This result leads to the conclusion that native tryptophan molecules are responsible for the observed signal from the chicken tissue samples.[20] The resultant difference found between TPF spectra of muscle/skin and fat was consistent with the fact that there is almost no tryptophan present in the fat tissues.[21] For phenylalanine and tryrosine, two photon excitation with 625 nm is not likely to induce TPA since the energy is far below the efficient absorption region. The measured spectra from these two molecules in dry powdered form however, exhibit two emission bands at 290 nm and 380 nm (Fig. 4.12), which can be attributed to other nonlinear mechanisms and higher order processes. The intrinsic fluorescence spectra of tissues can be distorted by a number of mechanisms such as wavelength dependent self absorption, scattering effects, excitation and emission angles.[22-25] The impact of multiple scattering and self-absorption on fluorescence spectra was experimentally studied by Yoo *et al.* in a medium made of dye solution mixed with T_iO_2 scatters.[22] The final fluorescence signal detected at the surface of the sample were found to be red shifted. The shift was attributed to the preferential scattering and internal absorption at shorter wavelengths in the spectrum. This attenuation mechanism should have an enhanced effect on the blue part of the TPF spectrum as the light travels a longer random path to emerge from the surface. The observed results in powder Trp particles (shown in Fig. 4.13) supported this conclusion. The red shift observed in the TPF spectrum compared with SPF is considered to arise from the self absorption effect and verifies a deeper interaction length in the two photon processes.

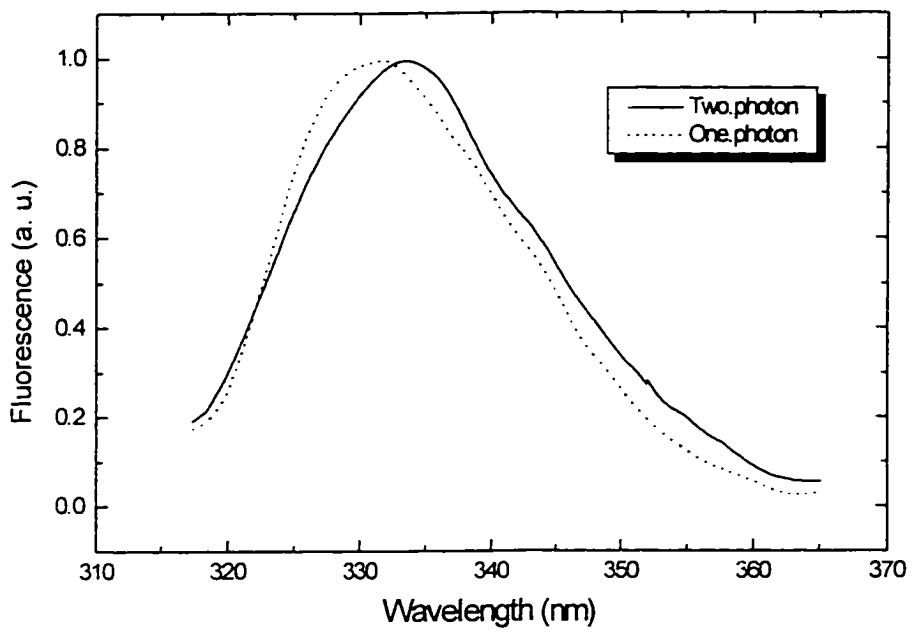

Fig. 4.13 One- and two-photon excitation of fluorescence of tryptophan powder particles under 312.5 nm and 625 nm laser excitations.

References

1. M. Göppert-Mayer, Ann. Phys. **9**, 273 (1931).
2. W. Kaiser and C. G. B. Garrett, Phys. Rev. Lett. **7**, 229 (1961).
3. J. P. Hermmann and J. Ducuing, Phys. Rev. A **5**, 2557 (1972).
4. H. Mahr, "*Two-photon Absorption Spectroscopy*", Chapter 4 in "*Quantum Electronics: A Treatise, Nonlinear optics, Part A*", Vol. 1, Academic Press, New York (1975).
5. Y. R. Shen, "*Principles of Nonlinear Optics*", Chapter 12, John Wiley and Sons, New York (1984).
6. H. Eyring, C. J. Christensen, and H. S. Johnston, "*Annual Review of Physical Chemistry*", Annual Reviews Inc. (1967).
7. W. L. Peticolas and K. E. Rieckhoff, J. Chem. Phys. **39**, 1347 (1963).
8. D. J. Bradley, M. H. R. Hutchinson, and H. Koetser, Proc. R. Soc. London Ser. A **329**, 105 (1972).
9. C. Xu and W. W. Webb, J. Opt. Soc. Am. B **3**, 481 (1996).
10. C. Xu, W. Zipfel, J. B. Shear, R. M. Williams, and W. W. Webb, Proc. Natl. Acad. Sci. **93**, 10763 (1996).
11. M. D. Galanin, B. P. Kirsanov, and Z. A. Chizhikova, Sov. Phys. JETP Lett. **9**, 304 (1969).
12. A. Fischer, C. Cremer, and E. H. K. Stelzer, Appl. Opt. **34**, 1989 (1995).
13. W. Denk, J. Biomed. Opt. **1(3)**, 296 (1996), and the references therein.
14. R. R. Alfano, D. B. Tata, J. Cordero, P. Tomashefsky, F. W. Longo, and M. A. Alfano, IEEE J. Quant. Electron. QE-20, 1507 (1984).

15. R. Richards-Kortum, R. P. Rava, R. E. Petras, M. Fitzmaurice, M. Sivak, and M. S. Feld, Photochem. Photobiol. **50**, 777 (1991).

16. Fig. 4.5 shows the single photon absorption and fluorescence spectra of key fluorescent molecules in native tissues. [After thesis of W. L. Sha Glassman, CCNY (1993)]. Fig. 4.6 shows a schematic diagram of commercially available laser sources providing various wavelength windows for two photon excitation of key fluorophores in biological tissues.

17. Y. Yang, L. D. Mitchell, and R. R. Alfano, J. Biomed. Opt. **2**, 53 (1997).

18. Ji Ji Cheng, *"Photo-biology Physics"*, Chinese Academic Publisher, Beijing, (1987).

19. R. R. Alfano, G. C. Tang, A. Pradhan, W. Lam, D. C. Choy, and E. Opher, IEEE J. Quant. Electron. QE-**23**, 1806 (1987).

20. Yici Guo, Q. Z. Wang, N. Zhadin, Feng Liu, S. G. Demos, D. Calistru, A. Tirksliunas, A. Katz, Y. Budansky, P. P. Ho, and R. R. Alfano, Appl. Opt. **36**, 968 (1997).

21. Personal communication with Dr. M. L. Steinberg.

22. S. A. Ahmed, Z. W. Zhang, K. M. Yoo, and R. R. Alfano Appl. Opt. **33**, 2746 (1994).

23. M. S. Patterson and B. W. Pogue, Appl. Opt. **33**, 1963 (1994).

24. A. E. Cerussi, J. S. Maier, S. Fantini, M. A. Franceschini, W. W. Mantulin, and E. Gratton, Appl. Opt. **36**, 116 (1997).

25. N. N. Zhadin and R. R. Alfano, J. Biomed. Opt. **3(2)**, 171 (1998), and the references therein.

Chapter Five

Second Harmonic Tomography of Biological Tissues

This chapter presents research on nonlinear optical second harmonic tomography in biological tissues and cells. Using femtosecond laser excitations at 625 nm and 800 nm, second harmonic tomography has been demonstrated as a novel and noninvasive imaging technique with local symmetry sensitivity and an inverse quadratic reflectance dependence for highlighting subsurface histological changes. The feasibility of nonlinear optical biopsy based on second harmonic tomography in normal and diseased tissues has been investigated.

5.1 Overview of Second Harmonic Microscopy in Biological Media

Optical microscopes have revolutionized biological and medical sciences since the first observation of microscopic organisms in 1668. Over the past three hundred years, advances in microscopy have allowed scientists not only to visualize structures in tissues, but also to follow molecules in real time within living cells.[1] Optical microscopy also plays a central role in histology and pathology. The conventional histology uses a series of fixing, embedding cutting and straining procedures to prepare the specimen into the histology slides. These slides are analyzed under microscope. The demand on high resolution and specialized functionality of microscopy has attracted intensive effort in developing new types of microscopes. Most recently, the NLO method of using multiphoton excitation to investigate native or tagged biological systems has become a rapidly growing area in bio- and medi-photonics.

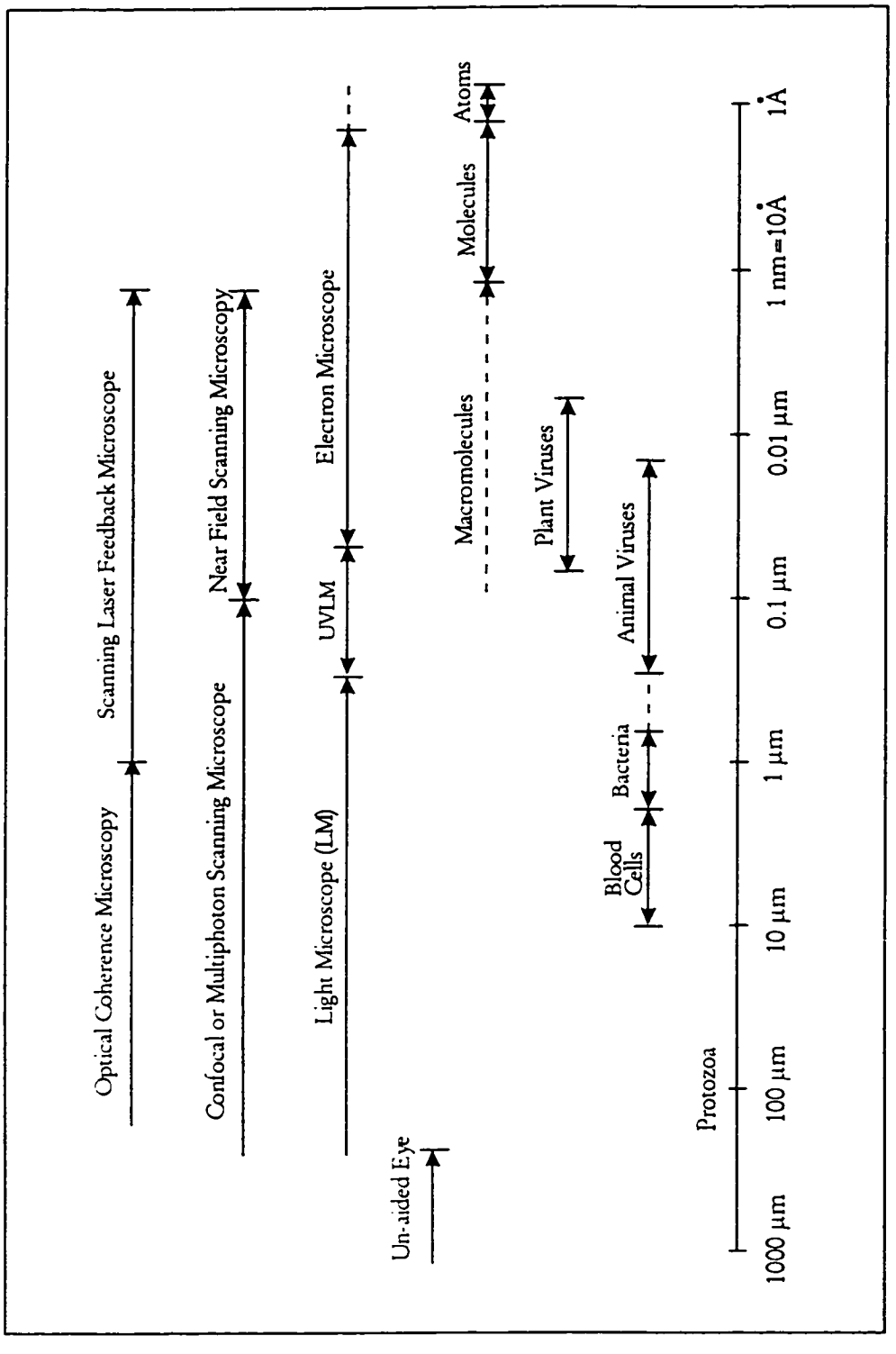

Fig. 5.1 Performance range of various types of microscopy techniques and dimensions of targeted biological objects.

The increasing interest in NLO microscopy is mainly driven by the search for new approaches besides conventional widefield or confocal microscopy to provide the following advantages: (a) a deeper penetration depth derived from NIR excitation to circumvent scattering and absorption effects, (b) improved sensitivity and optical sectioning capability based upon nonlinear dependence of signal on the incident intensity, and (c) reduced photobleaching and cyto-toxicity due to spatially localized excitation. On the other hand, a drawback is introduced from complexity, increased cost, and size due to the requirement of a mode locked laser system and highly sensitive photo-detection units.

Theoretical models of transmission, reflection and resonant scanning SH microscopes were first proposed by Sheppard *et al.* in 1977[2], and experimentally demonstrated by Freund *et al.* in 1986.[3] Fig. 5.2 shows the block diagrams of the transmission type SH scanning microscope for studying polar filaments and collagen fibrils in a rat-tail tendon system.[3] Figs. 5.2a, b illustrate a single and a crossed-beam version of SH scanning microscopes, respectively. In the single beam geometry, a laser beam is focused through a set of lenses onto the sample, and the signal is scanned and detected in the transmission pathway. In the crossed beam geometry, a laser beam is first split into two equal portions, and then focused onto the sample with a crossing angle ensured with spatial and temporal overlap. The transmitted signal is detected in the center direction dissecting the angle formed by the two incident beams. The single-beam SH microscope allows one to use either a coherent or an incoherent scanning mode, by angularly selecting the signal in the forward direction while moving the sample relative to the laser focus. The images acquired under coherent and incoherent modes thus distinguish between the ordered polar filaments and the disordered fibrils. Quantitative thickness and volume estimation of polar filaments have been obtained using the crossed-beam SH scanning geometry.[3]

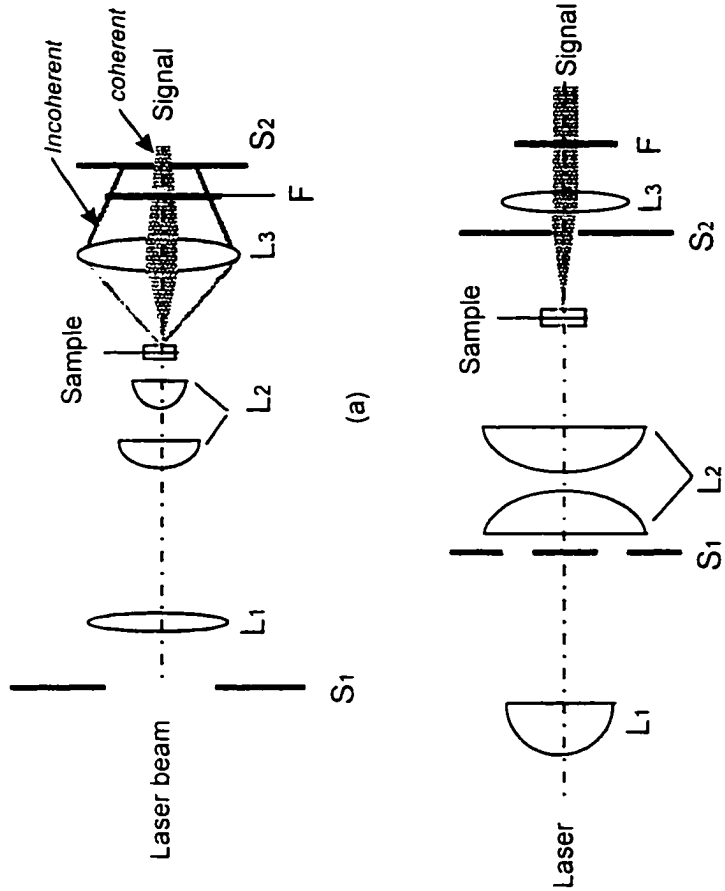

Fig. 5.2 Transmission second harmonic microscope. (a) a single-beam version, and (b) a crossed-beam version. In the single-beam version, the forward SH signal has two components: a coherent component along the axial beam direction and an incoherent component with a broad spatial distribution. L_i, lenses or condensers; S_i, apertures; and F, filters.

After Reference 3.

Transmission scanning SH technique offers structure sensitivity based on coherent characteristics of the nonlinear signal. The method is however invasive and usually limited to nearly transparent or extremely thin preparations for resolving optical contrast in the forward direction. The scattering or diffusion in turbid specimens hampers its effective resolution and applicability in thick and scattering tissues as the coherent light component decreases exponentially with the sample's thickness.

5.2 Two Photon Excitation and Imaging Properties

The key characteristics of SH/TPF microscopy stem from the excitation process used by the NLO imaging techniques. To facilitate SHG and TPF, the laser energy carried by the addition of two incident photons is used to generate signals, i.e., a photon at twice the incoming frequency or fluorescence emission from an excited state. In both cases, the signal scales quadratically with the instantaneous laser intensity. Because of the small second order nonlinear susceptibility $\chi^{(2)}$ and the low TP absorption cross section σ_{TPA} , the excitation of SH and TPF signals requires high-peak-energy photon pairs that are coincident temporally and spatially. This is in contrast to a single photon excitation induced fluorescence which derives from a linear dependence on the laser intensity.

Fig. 5.3 illustrates the axial distributions of the signal under a single photon excitation versus double photon excitation in a typical homogenous medium. The spatial distributions show that the one photon excited signal extends over the optical path along the laser beam whereas the two photon signal confines itself to the immediate focus where the laser intensity is the strongest. It has been shown that an

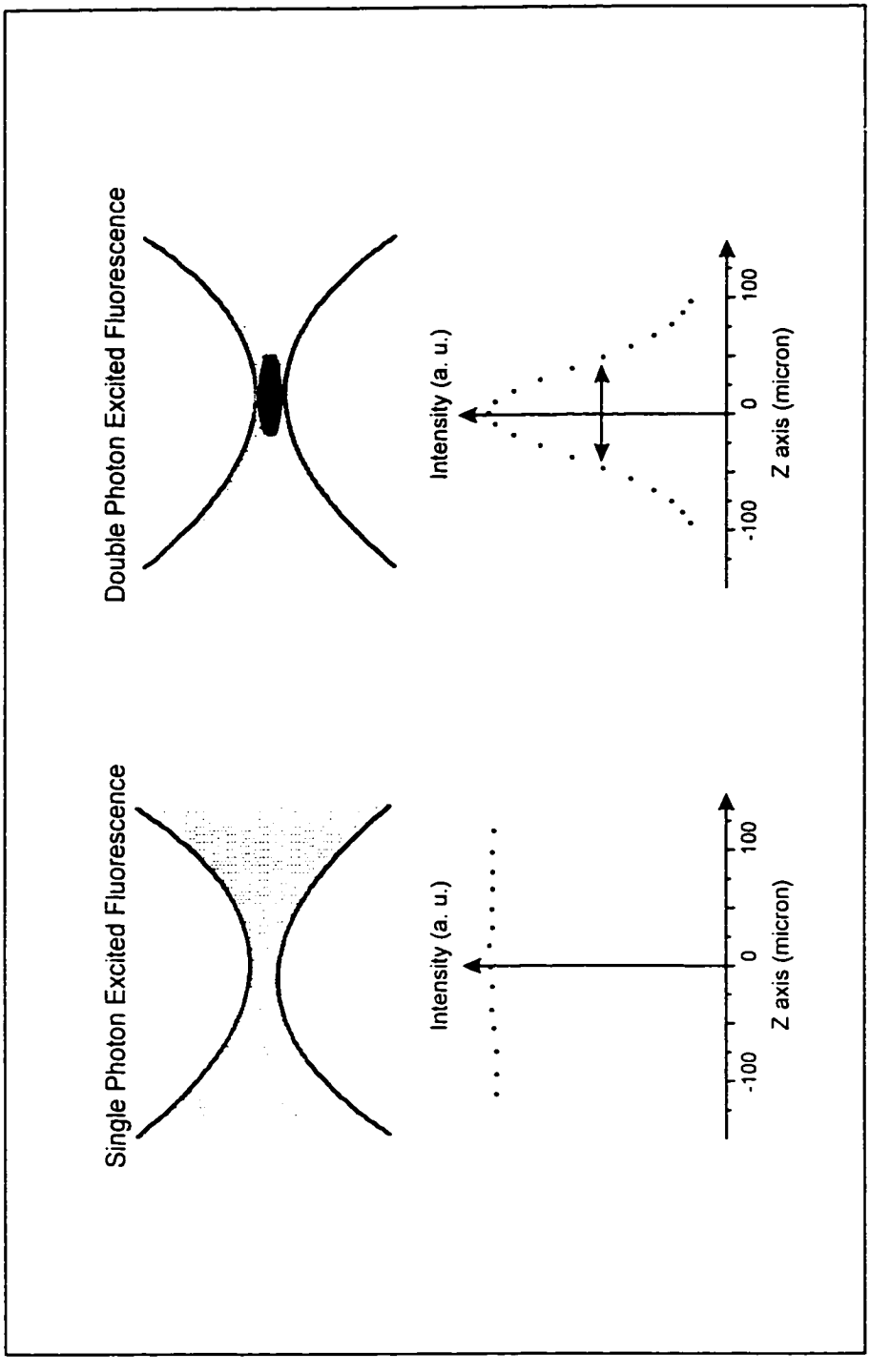

Fig. 5.3 Axial profiles of single photon versus double photon excited fluorescence in dye solutions. Double photon excited signal is typically a double cone structure which arises from a fluorescence signal throughout the sample. Double photon excited signal is confined to the immediate laser focus where the light intensity is the strongest.

objective lens with a numerical aperture of 1.25 can confine over 80% of the total TPF signal to within ± 1 μm of the focal plane at an excitation wavelength of 780 nm.[4,5] At 700 nm, a 1.3 numerical aperture objective lens can localize the signal to a volume of only 0.1 μm^3.[5]

Knowledge of 3-D optical properties of biological samples is related to image resolution and image contrast. Image resolution depends on the point spread function (PSF) that determines the system performance. Image contrast is generated from differential absorption, reflection, birefringence and phase change due to specimen composition or structure variation. In a conventional microscope, the minimum resolvable spacing ζ is given by:

$$\zeta = \frac{0.61\lambda}{NA}, \tag{5.1}$$

where λ is the wavelength and NA is the numerical aperture of the lens. For $NA = 0.4$, $\lambda = 800$ nm, $\zeta = 1.22$ μm.

The evaluation of the overall performance in a laser scanning microscope generally involves three parameters: (i) resolution derived from the minimum resolvable spatial variation, (ii) optical contrast determined by the signal to background ratio and (iii) image information capacity that is limited by the signal to noise ratio. The background is defined as the light generated from off focus planes. The noise is defined as the square root of the total light detected, which is the square root of the signal plus the background.[6]

When imaging a point source, the width of PSF determines the lateral resolution and the height of PSF determines the axial resolution. Currently, there are two methods that are used to describe the 3-D image property: (a) using the 3-D intensity PSF by imaging an ideal point, or (b) using the 3-D optical transfer function

(OTF) obtained from the Fourier transform. The former method gives the imaging performance in practical space, while the latter method describes the imaging property in Fourier space.

Under the paraxial approximation, the PSF for single photon excitation is given by[7]:

$$I_{1p}(v,u) = h^2[u,v] = \left| 2\int_0^1 J_o(v,\rho)\exp(iu\rho^2/2)\rho d\rho \right|^2, \tag{5.2}$$

where J_o is the zeroth order Hankel function; v and u are defined as the radial and axial optical coordinates which are related to the real cylindrical coordinates:

$$v = k(NA)r, \tag{5.3}$$

$$u = k(NA)^2 z/n, \tag{5.4}$$

where $k=2\pi/\lambda$ is the vacuum wave number, $NA=n\sin\alpha$, α is the half angle of collection for the objective lens, r is the distance from the optical axis and z is the distance from the focal plane.

In a two photon process, the excitation is determined by the modulus square of the field intensity $|I(r,z)|^2$. Two photon PSF is the square of the linear intensity PSF[7]:

$$I_{2p} = |I_{1p}(v,u)|^2 = \left| 2\int_0^1 J_o(v,u)\exp(iu\rho^2/2)\rho d\rho \right|^4. \tag{5.5}$$

The 3-D two photon OTF can be derived by performing the 3-D Fourier transform of the 3-D intensity PSF:

$$C_{2p}(l,s) = F[I(v/2,u/2)] \otimes_3 F[I(v/2,u/2)], \tag{5.6}$$

where F represents the 3-D Fourier transform and $\otimes_3$ denotes the 3-D convolution operation. l and s are the radial and axial spatial frequencies normalized by $\sin\alpha / \lambda$ and $\left[4\sin^2(\alpha/2)\right]/\lambda$, respectively. $F\left[I(v,u)\right]$ can be expressed as:

$$F\left[I(v,u)\right] = \frac{2}{l}\mathrm{Re}\sqrt{1-\left(\frac{|s|}{l}+\frac{|l|}{2}\right)^2}\,. \tag{5.7}$$

At $s=0$, the 3-D OTF describes imaging of a thick object with no variations in the axial direction. At $l=0$, the 3-D OTF corresponds to imaging a planar structure with no variation in the transverse direction.

Theoretically, the 3-D image can be modeled in all cases by performing the inverse Fourier transform of the object spectrum multiplied by the 3-D OTF, i.e., $I_{2p}(u,v) = F^{-1}\left\{\left[C_{2p}(l,s)\right]\cdot\left[S(l,s)\right]\right\}$, where $S(l,s)$ is the object spectrum.

The comparison between the signal intensities under one- and two-photon excitation modes is shown in Fig. 5.4. The signal intensity profile under the two photon excitation clearly demonstrates depth discrimination, i.e., the contribution from axial sections away from the focal plane falls sharply. In contrast, the contribution form different axial sections under one photon excitation is independent of the focal plane position.

5.3 Second Harmonic Tomography in Modeled Random Medium

5.3.1 Experimental Method and Sample

To demonstrate the spatial resolving power and feasibility of locating subsurface structures in second harmonic tomography, experiments were first conducted in modeled random scattering samples. Fig. 5.5 illustrates the experimental

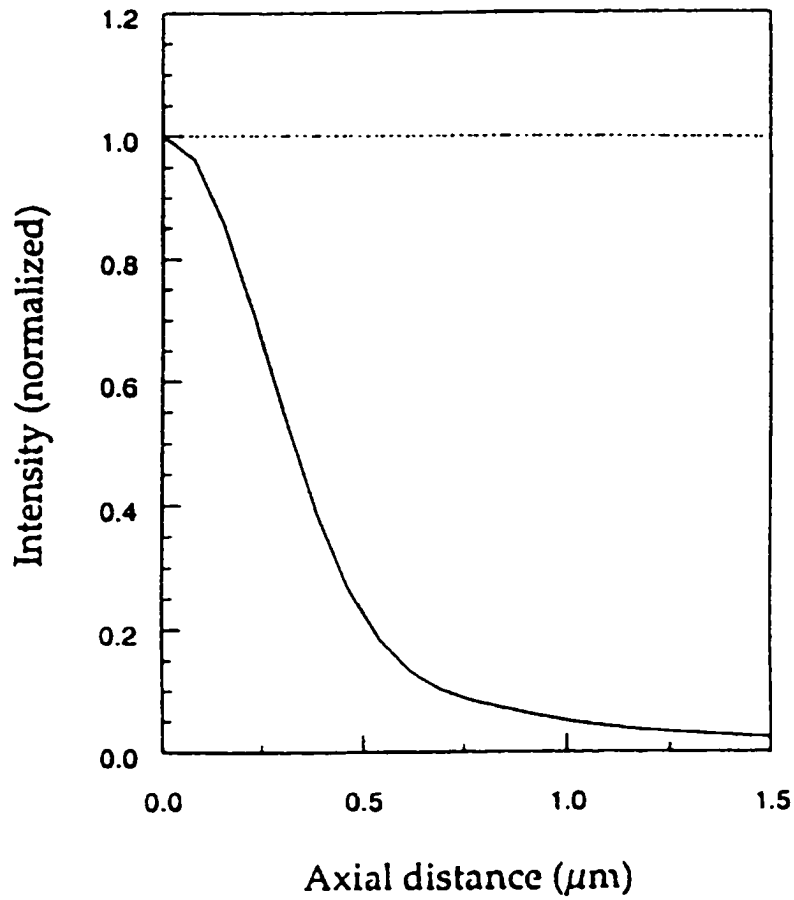

Fig. 5.4 Axial profiles of signals under one- and two-photon excitation. The dashed line shows the one photon exited signal intensity. The solid line shows the two photon excited signal intensity. The calculation assumes an excitation wavelength of 760 nm and a numerical aperture of 1.25.

After Reference 7.

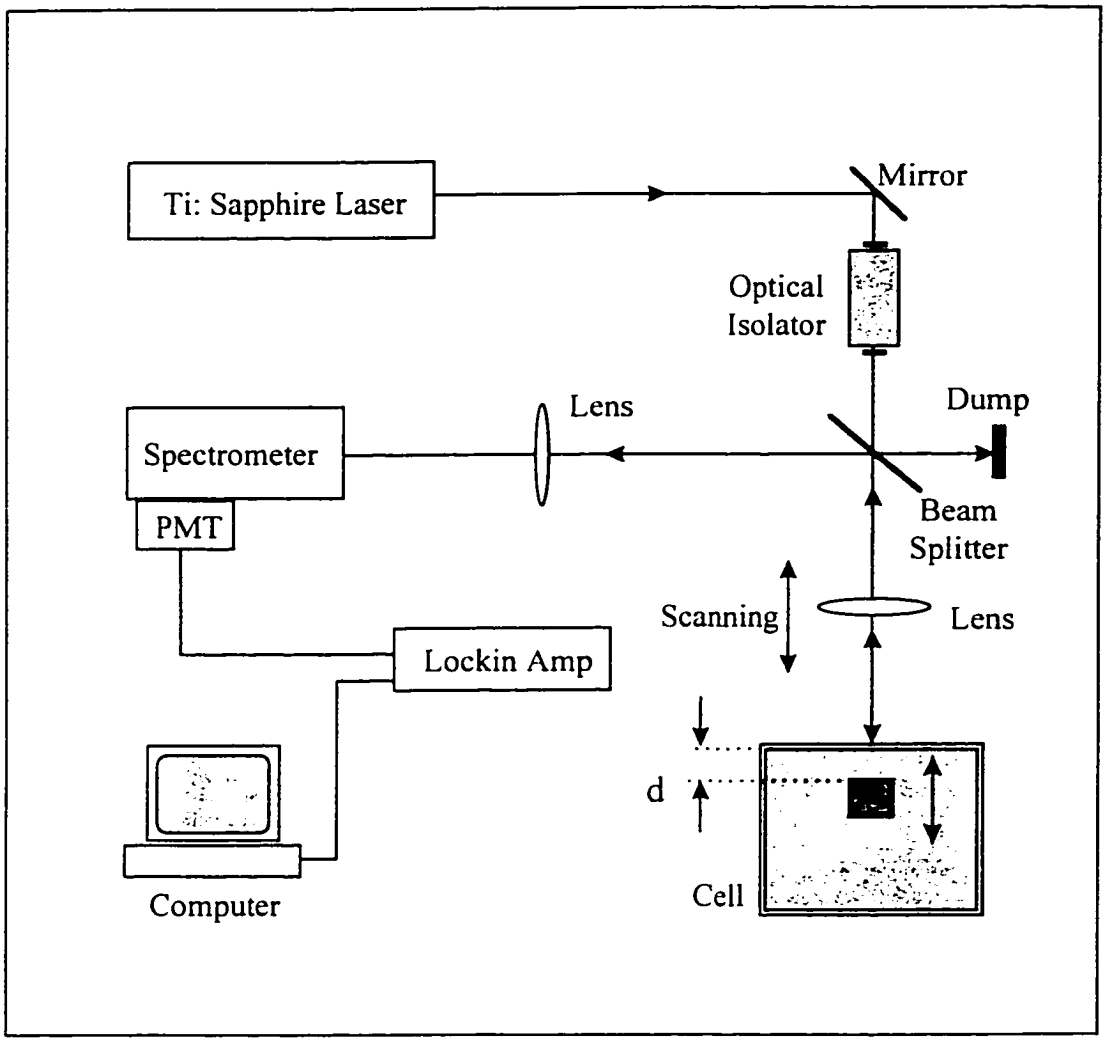

Fig. 5.5 Experimental setup of second harmonic imaging in modeled multi-layered scattering medium. An optical lens is scanned along its optical axis to resolve the embedded object S inside a cell of water quartz particle mixture.

setup. Femtosecond laser pulses at 800 nm were transmitted through a beam splitter and focused by an optical lens onto the sample at a normal incidence. An electronic controlled motor-driven translation stage was used to move the optical lens along the incident direction to achieve axial depth-scan. The second harmonic signal backscattered from the sample was collected by the focusing lens, then reflected by the beam splitter to the entrance slit of a spectrometer. At the exit slit of the spectrometer, a photomultiplier tube, a lock-in amplifier, and a personal computer were used to record and display the data. In order to simulate a structure of multiple interfaces, a modeled random sample was constructed by two cells of scattering medium. The first plastic (outer) cell had a dimension of $5 \times 5 \times 4$ cm^3 and was filled with a mixture of water and suspension of quartz particles of nominal size ≈ 5 μm. The second (inner) cell with a dimension of $1 \times 1 \times 3$ cm^3 was packed with dry powders of quartz particles and immersed in the first cell as an embedded object. A second translation stage was used to control the movement of the second cell inside the first cell. The distance d, which refers to the separation between the first and second cells, was adjusted for simulating a subsurface-layered system.

5.3.2 Results

Fig. 5.6 shows the measured one dimensional axially scanned second harmonic intensity profiles versus depth z as a function of d for the sample described in section 5.3.1. Each depth-scanned signal follows a profile of multiple peaks generated from different interfaces. The salient changes of these scans shown in Fig. 5.6 are: (i) the positions z where the peaks emerge and (ii) the peak magnitude and shape associated with variance in d. Information about structures in the subsurface region can be derived from these features. To illustrate, peak position markers are added in Fig. 5.7

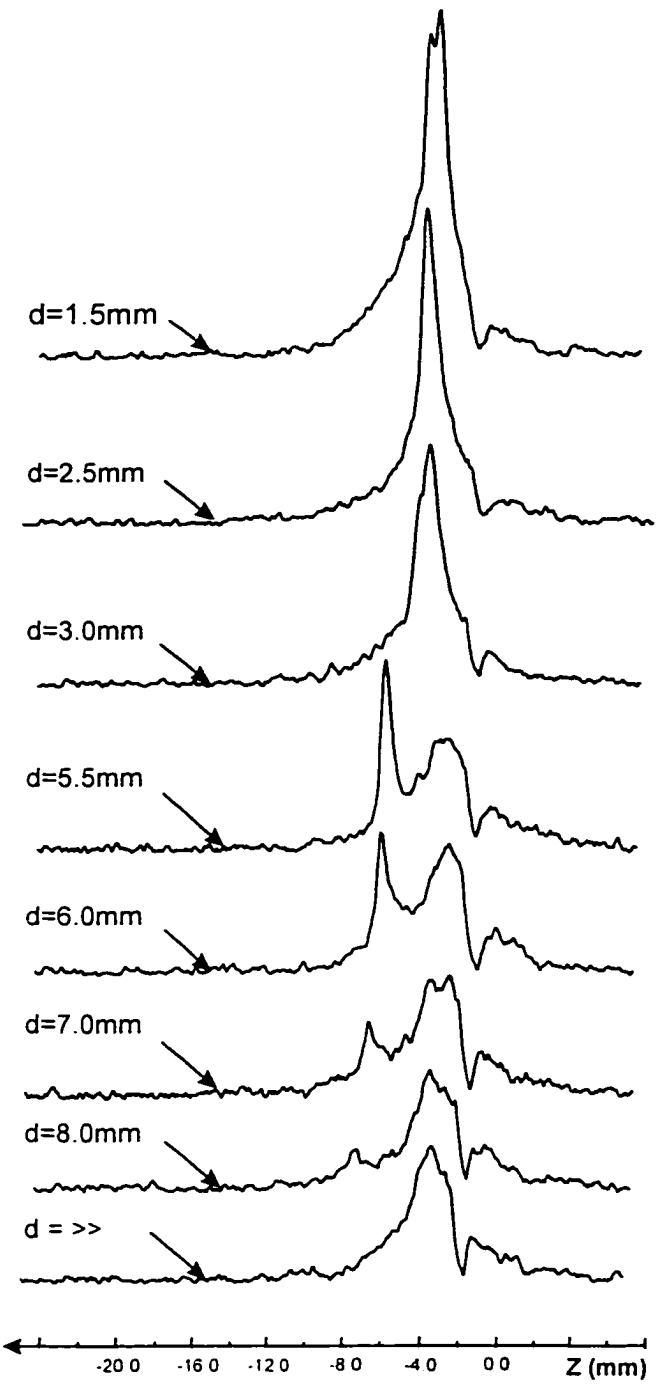

Fig. 5.6 The axially scanned profiles of second harmonic signals in modeled random scattering sample constructed with an object cell immersed in water-quartz particle suspension.

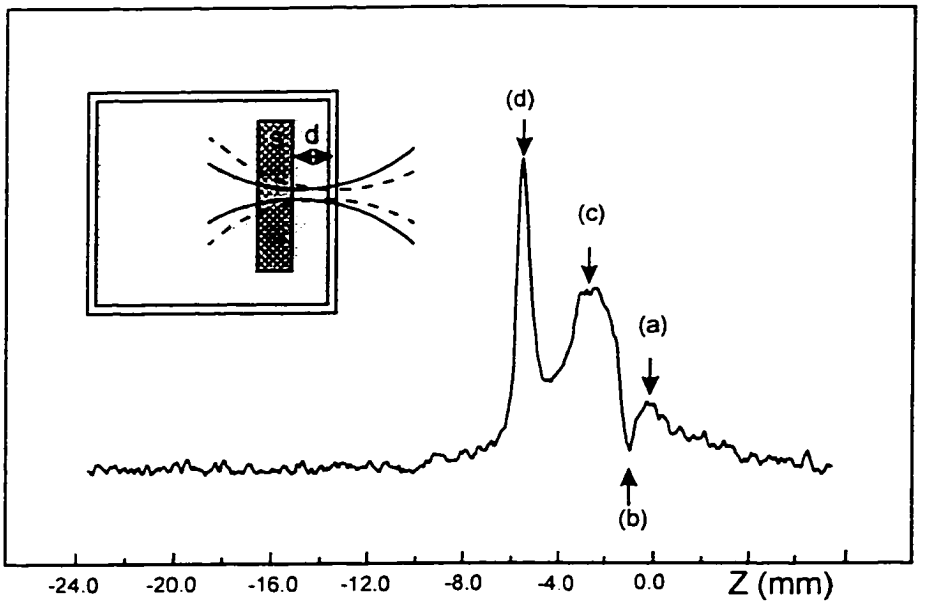

Fig. 5.7 One dimensional axially scanned second harmonic profile in a modeled scattering sample shown in the insert. Position markers (a)-(d) correspond to interfaces at different locations of the sample.

to describe the structural details. For a typical scan at d=5.5 mm, the first peak (a) encountered at rightmost along the scanned distance is resolved from the front surface of the plastic wall of the outer cell. The following dip (b) represents the signal when the laser focus is traveling inside the plastic wall. The second peak (c) after the dip is generated from the interface of the water-quartz suspension mixture; and the third peak (d) corresponds to the interface at the quartz powder in the second cell. As the distance d varies from 1.5 mm to 8 mm, the separation between the second and third peaks shown in Fig. 5.6 clearly indicates the location of the shifting embedded object.

5.4 Second Harmonic Tomography of Biological Tissues

5.4.1 Experimental Methods and Samples

The experimental setup used for studying biological tissue samples is schematically shown in Fig. 5.8. This arrangement can be used for simultaneously acquiring the second harmonic and two photon excitation of fluorescence images. The wavelength demultiplexing for isolating signals from other background is accomplished by either using different combinations of narrow band and band pass optical filters or by using grating or spectrometer incorporated multi-channel detection modules. To illuminate the sample, a laser beam is deflected by mirrors and a dichroic beam splitter which reflects the laser light and transmits the SH and TPF signals. A UV microscope objective lens is used for focusing the excitation beam and collecting the signal. At the image plane of the detector, the SH and TPF emissions are selected by appropriate optical filters which either transmit the light at half of the laser wavelength or at the peak wavelength of the fluorescence band.

An amplified colliding-pulse mode-locked dye laser system generated 100 fs pulses at 625 nm, with a repetition rate of 6.5 kHz. The incident power at the sample

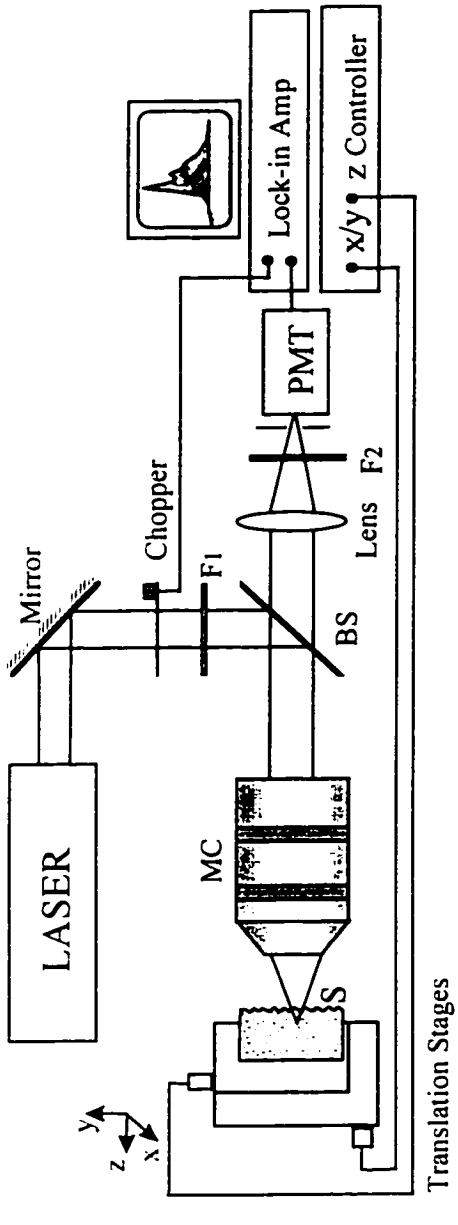

Fig. 5.8 Schematic of SH tomographic imaging setup. MC, microscope objective; BS, dichroic beam splitter; F1 and F2 long and narrow band pass filters, respectively; PMT, photomultiplier tube.

site was ~200 μW. 3-D image scanning was achieved by translating the sample relative to the laser focal spot. The axial profile versus depth was measured by a scan of the sample with a translation stage moving along the optical axis of the microscope objective lens. The z axis was directed into the tissue and the z coordinate corresponded to the focal plane position moved in air. The lateral scan was performed with a second translation stage moving in the direction across the sample surface. The scanning pixel residence time was 0.1 second which contributed to an image frame time of 2.8 hours. A photomultiplier and a computer-controlled lock-in amplifier were used to record the data. Three samples were used for the demonstration of SH tomography. The samples were frozen tissues excised from the upper thigh portion of chickens and then thawed. The samples were: a section of skin tissue, a fascia attached to a muscle tissue, and a section of muscle tissue.

5.4.2 Results

The 2-D pseudo color SHG tomographic images of the three tissue interfaces are shown in Fig. 5.9a, 5.10a and 5.11a. Fig. 5.9 shows a imaged structure of a section of chicken skin tissue. Fig. 5.10 shows a SH map associated with a tendon-like membrane of fascia attached to a muscle tissue. Fig. 5.11 shows the resultant image of only muscle tissue. Selected axially scanned SHG profiles along the z direction are displayed in Figs. 5.9b, 5.10b, and 5.11b.

5.4.3 Discussion

The layered structure in the medium is clearly resolved in the axially scanned profile. Similar to the scans in Fig. 5.6, the salient features of images in Figs. 5.9 - 5.11

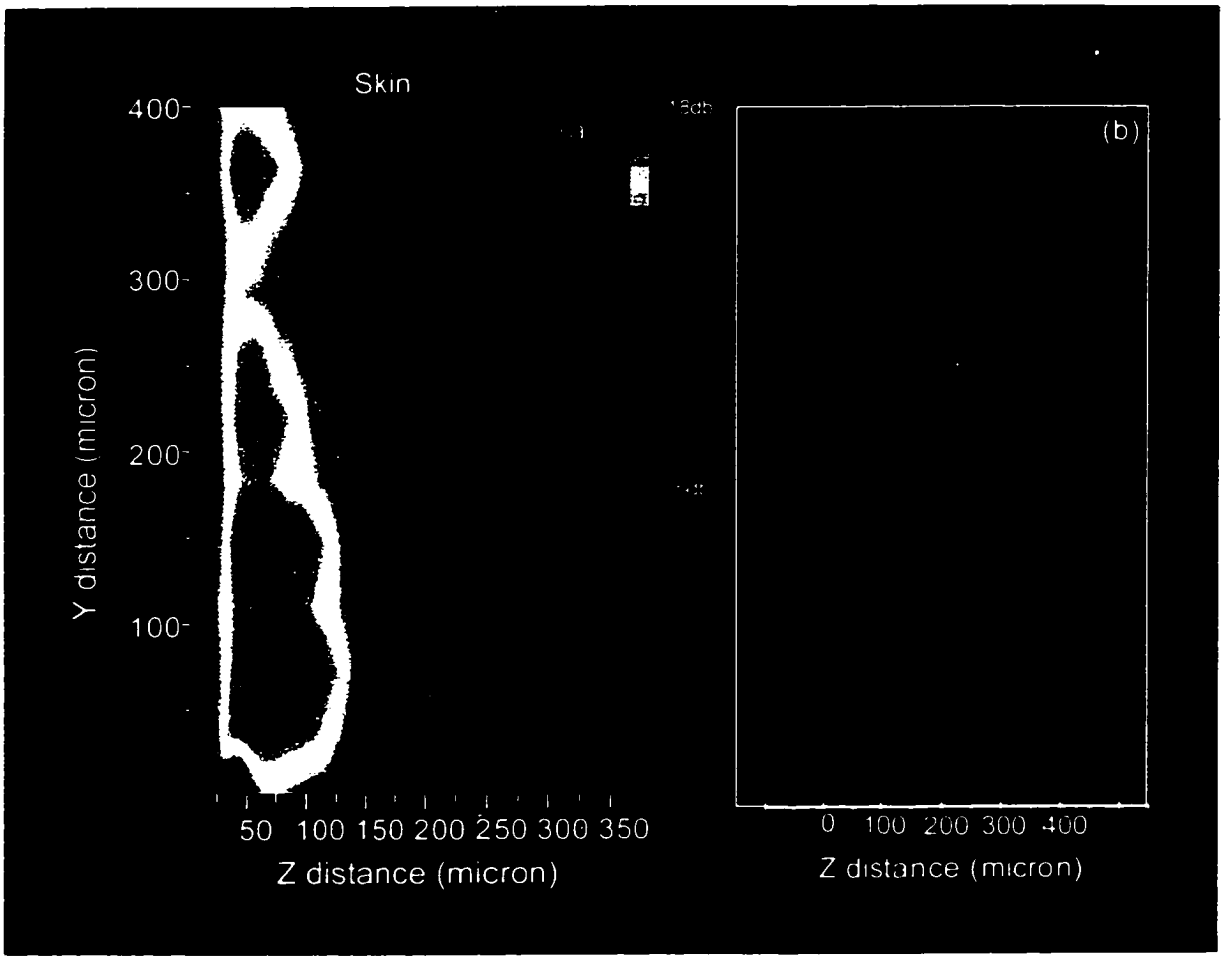

Fig. 5.9 (a) 2D SHG depth image of a chicken skin tissue, log I_{SHG} versus y, z. (b) Analog axially scanned SHG profiles in linear scale.

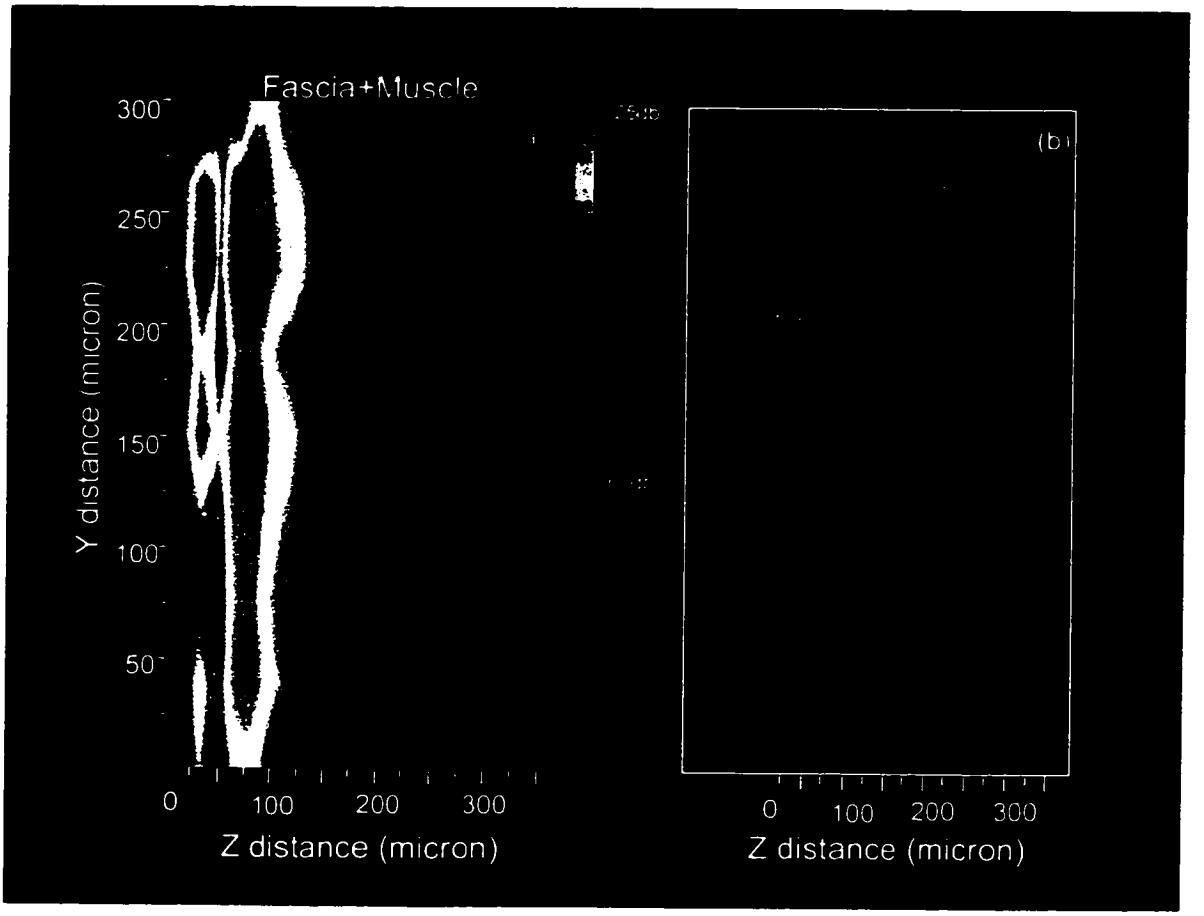

Fig. 5.10 (a) 2D SHG depth image of a fascia membrane attached to chicken muscle tissue, log I_{SHG} versus y, z. (b) Analog axially scanned SHG profiles in linear scale.

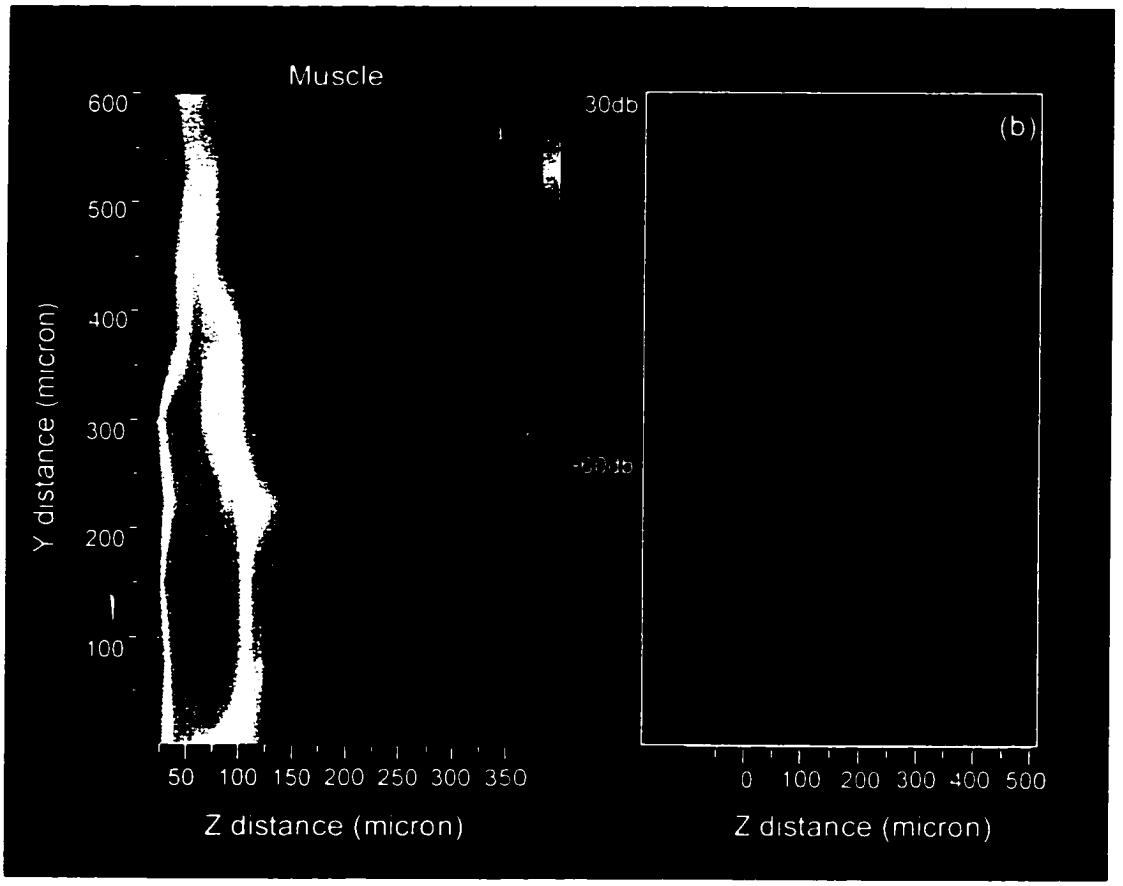

Fig. 5.11 (a) 2D SHG depth image of chicken muscle tissue, log I_{SHG} versus y, z. (b) Analog axially scanned SHG profiles in linear scale.

are evidenced by the observed apexes along the z direction, appeared before and after the dominant maximum. In Fig. 5.9b, a major peak is resolved first from the skin tissue. The second or the third subsidiary peaks are associated with the subsurface layers due to multiple interfaces as determined visually through a microscope.

In Fig. 5.10b, a minor peak emerges first from the tendon membrane, followed by the response from the muscle. The corresponding image in Fig. 5.10a also exhibits two higher intensity regions with a dip band in between. Further investigation revealed that the relative position and height of the first and second resolved peaks were strongly affected by the thickness of the fascia layer and its scattering property. An estimation of the fascia thickness is in the range of a few tens of micrometers for this particular image. Fig. 5.12 displays the comparison of two individual depth scans obtained from different tissue samples as the dominant and subsidiary peaks change their magnitude and position according to the properties of different layers. When only muscle tissue is imaged, different structures can be seen in Fig. 5.11b from the axially scanned profile. In this case, the minor variations at the tail part are magnified by scale differences due to the overall smallness of the signal. These minor structures are not from layers, but rather from the detailed variations in the local environment such as encountered muscle fibers, collagen and mesentery fibrils. These results are confirmed by the histology micrographs in Fig. 5.13a and 5.13b. Fig. 5.13a shows the cross section of the chicken skin tissue that consists of the cytokeratin layer, the basal layer, the collagen layer and the fat layer. A feather follicle is located in the fat layer. The interfaces resolved in the second harmonic image from skin (Fig.5.9) correspond to these layers. Fig. 5.13b shows a cross section of a chicken tissue comprised by a fascia layer attached to a muscle tissue. The fascia-muscle interface was resolved in the scanned SH image shown in Fig. 5.10.

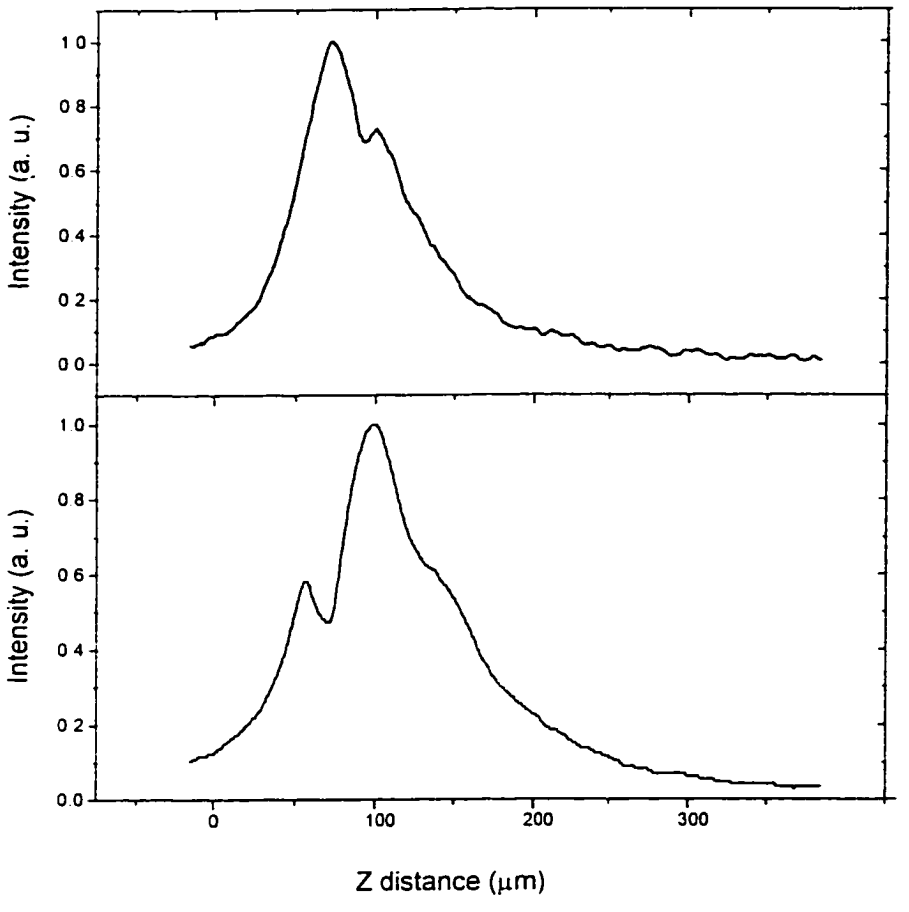

Fig. 5.12 Axially scanned second harmonic profiles from chicken tissues that consist of fascia layer attached to muscle tissues. Different thickness of the fascia layer is shown by the first emerged peak along the z distance.

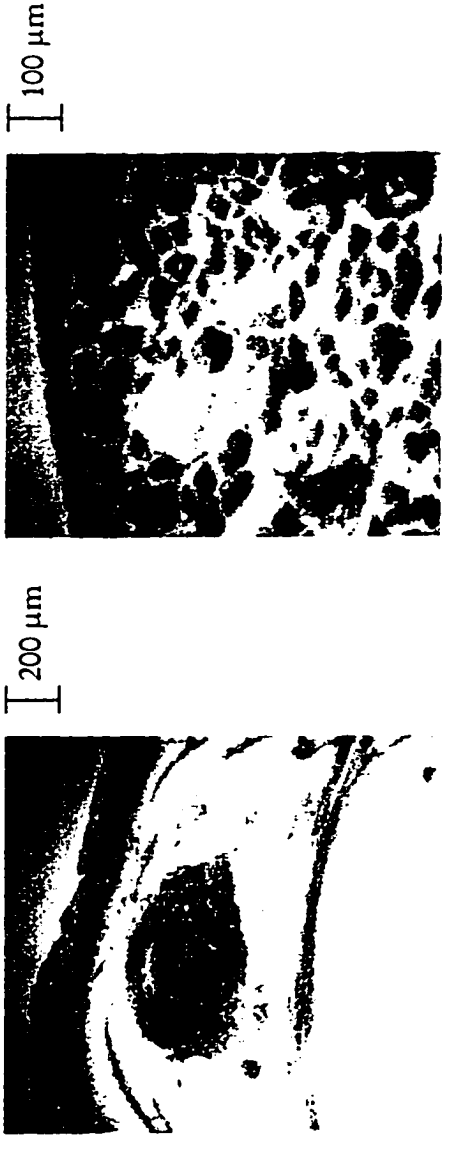

Fig. 5.13 Histology micrographs of (a) chicken skin with follicle and (b) fascia attatched to muscle tissues.

Second harmonic generation combines the high spatial resolution with optical sectioning capability and a morphology symmetry sensitivity on a microscopic level.[8] Due to symmetry dependence, $\chi^{(2)}$ is inhibited in isotropic materials.[9] Broken symmetry occurs at the boundaries and interfaces which enables surface and subsurface interfacial SHG. Compared with the reflectance based imaging technique such as optical coherence tomography, SHG has an additional advantage in its symmetry sensitivity because it depends not only on the reflection coefficients, but also on the local $\chi^{(2)}$ tensor components. The inverse quadratic dependence on the refractive index allows SHG to highlight morphological changes and small index of refraction differences.

In contrast to TPF, SHG brings image contrast from non-fluorescent molecules. SH signals arise from the $\chi^{(2)}$ tensor, which depends on the electronic configuration, molecular symmetry, local morphology and the orientation and alignment of the molecules or ultrastructures. The excitation wavelength does not depend on the molecular absorption band and thus can be further shifted to the IR region. This property is in contrast to multi-photon microscopy, where extending the source wavelength is accompanied by trading off the signal magnitude through a three photon or even higher order process. Furthermore, SHG is a second order NLO process which could generate signal orders of magnitude higher than that from a third order process (TPF), thereby enabling signal detection at a deeper depth from the scattering media.

Harmonic generation arises from a coherent process where the signal highly depends on the intensity, phase, propagation direction, and polarization of the primary wave. The nature of the harmonic generation requires a coherent excitation where the scattering length l_s is the appropriate parameter to characterize the process. The ballistic component carries the coherent information from the medium. Its

intensity depends on the scattering length l_s as $\exp(-z/l_s)$, where z is the penetration length. Up to a ~sub-mm depth beneath the tissue surface, the coherence is still considered to be largely preserved, where the signal originates.

One of the key concerns in various biomedical imaging is to extract measured data at the greatest depth while keeping the focus quality under multiple scattering events. In transparent specimens, image resolution at depth is degraded only by spherical aberration introduced through the sample along the beam path. The measured transverse and axial distributions of a 20× microscope objective of $NA = 0.4$ at a wavelength of 800 nm are shown in Fig. 5.14. Figs. 5.14a-d show the lateral spatial distribution of the laser focus obtained at different axial positions, while Fig. 5.14e shows the corresponding FWHM widths versus the axial distance giving an estimated axial resolution of ~50 μm. In scattering specimens, the image resolution becomes functions of the sample's scattering property, the *NA* of the objective lens, the wavelength, and the axially scanned depth. The system performance of a SH/TPF scanning microscope will be degraded by light scattering compared with that in transparent tissues.

5.5 Nonlinear Optical Biopsy for Normal and Diseased Tissues

The basic goal of optical biopsy is to noninvasively give histological information and characterize the state and structure of tissue. In this section, initial results on nonlinear optical biopsy spectroscopy and imaging for *in vitro* human and animal tissues using second harmonic generation will be presented.

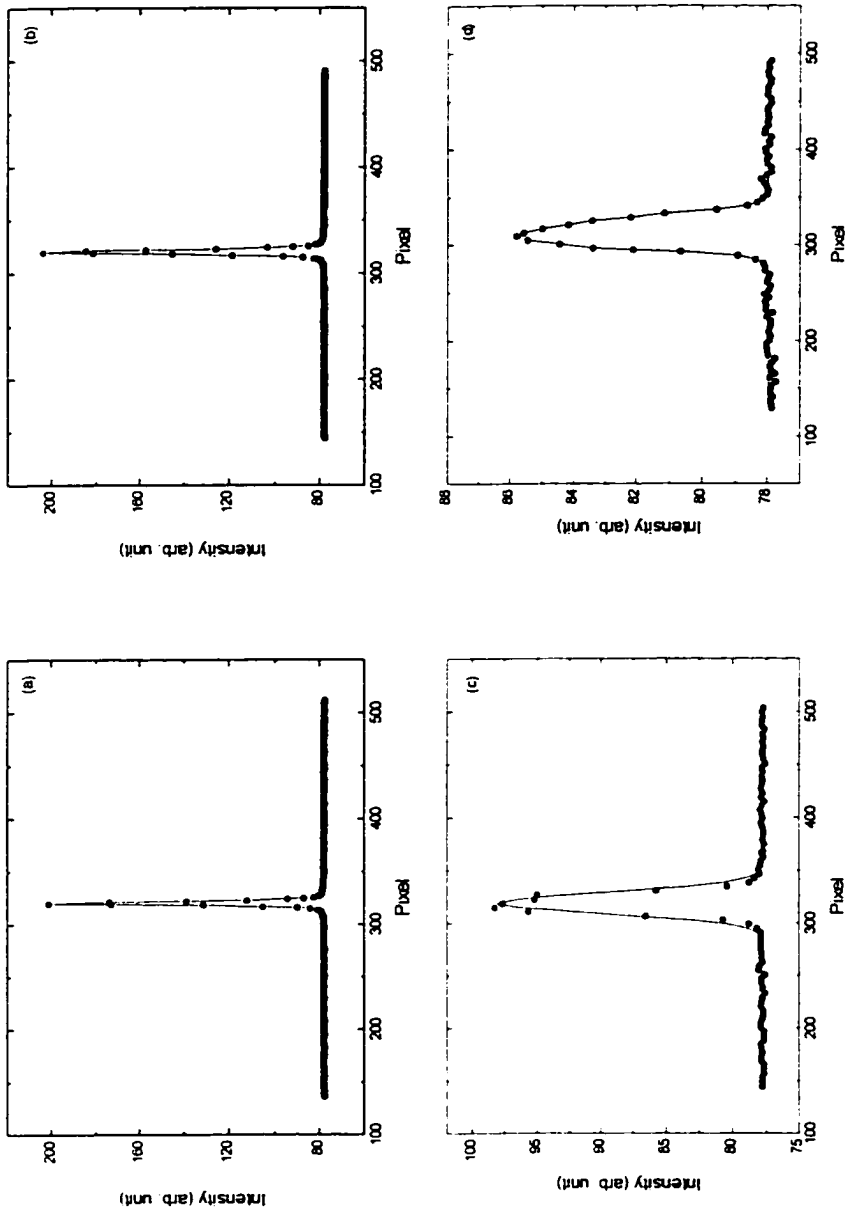

Fig. 5.14 Lateral intensity distributions of laser focus at 800 nm obtained from optical cover glass. (a)-(d), at z=0, 10 μm, 20 μm, and 30 μm, respectively.

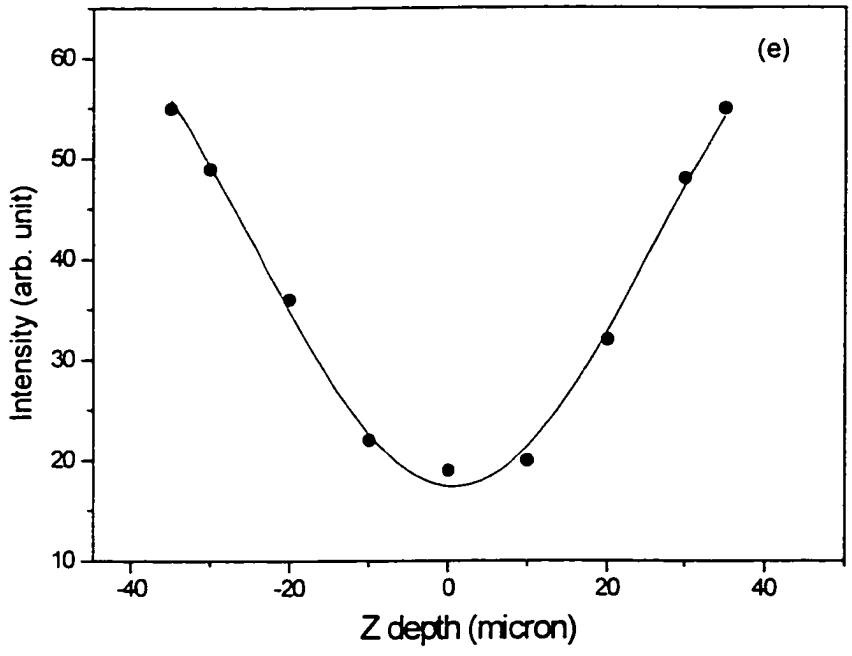

Fig. 5.14 cont. Axial profile of laser focus of a 20X microscope objective obtained at 800 nm. The fitted Guassian distribution gives an axial resolution of 50 μm.

5.5.1 Nonlinear Optical Approaches to Diagnose Cancer

Cancers are determined from histological examination of tissue. The process of cancer development in epithelial tissues progresses in five stages[10]: (1) genetic alteration, (2) hyperplasia, (3) dysplasia, (4) *in situ* cancer, and (5) invasive cancer. Genetic alteration is the mutation happening at molecular level, which increases the cell's propensity of proliferation. Hyperplasia refers to over proliferation of the altered cell and its descendants. Although hyperplastic cells appear normal in shape, a chance of further mutation on growth control may lead to dysplasia. Dysplasia refers not only to excessive proliferation, but also to abnormal shape, orientation, and behavior of cells. Dysplasia is also called precancer. At the *in situ* cancer stage, the tumor cells continue to become more atypical in growth, shape and size, but are still confined to the site with a defined boundary. An invasive cancer is the stage where tumor cells begin to invade underlying tissues, blood vessels, and lymph nodes. The tumor can metastases throughout the body, which is lethal when disrupting a vital organ.

The basis for using optical approach to detect cancer builds upon the characteristics of either chemical or physical (morphological) changes related to the diseased tissue site. To detect in chemical changes, absorption, excitation, fluorescence, and Raman spectroscopy are well established optical methods for quantitatively labeling and analyzing tissue compositions at a molecular level. These optical techniques can be used to highlight changes related to specific substances generated from abnormal activities in protein synthesization, changes in both cell membrane and cell adhesion, secretion and necrosis accompanied by tumor development.

The application of fluorescence technology to distinguish normal and cancerous tissues was first pioneered by Alfano's group in 1984.[11] Over the past fifteen years, this research direction has been actively pursued with widespread interest and positive results.[11-16] Fluorescence technology holds the promise for precise, high throughput, and wide spectrum diagnosis of diseases. Two-photon fluorescence microscopy may add a further advantage by its non-ionizing, deep penetration and optical sectioning properties.[17] Fluorophores naturally fluorescing in cells are believed to carry information about the state of the tissue. The fluorescence from native biochemical intermediates may give distinctive signals as the tissue undergoes normal to cancerous transformation. Unlike methods of using chemical dyes to mark structures, the intrinsic signals from native molecules carry information free of interactions between extrinsic agent and tissue components. TPF technique is well suited for identifying the characteristics of native fluorescent molecules and facilitating fast and wide area medical diagnosis.

On the structural side, abnormalities of morphological alterations in tumor growth are likely to be detected by structure- or symmetry-sensitive methods such as second harmonic tomography[8] and optical coherence tomography.[18,19] By utilizing dependence on symmetry and on reciprocal higher powers of refractive index, SHG is capable to highlight changes associated with the shape, orientation, alignment and organization of ultra-structures within the scale of the illuminating light wavelength. These ultra-structures can be any aligned or partially aligned asymmetric molecules, macromolecules, cellular components, and segments of intercellular matrix. For tissue constituents larger than the wavelength scale or randomized on the scale of the wavelength, the interfacing effect is likely to dominate over bulk contribution in SHG.

Boundaries at the cell membrane and cell nucleus are of primary interest as the source objects for surface SHG. Image contrast mechanisms based on these nonlinear properties may be used to resolve structural details, especially during the early stage of cancerous lesions that are difficult to be determined in a conventional linear optical biopsy.

5.5.2 Nonlinear Optical Spectroscopy of Human Breast Tissues

To demonstrate the feasibility of nonlinear optical biopsy, the spectral characteristics of SHG and TPF have been studied in normal and diseased human breast tissues. The experimental setup and laser source have been described in Fig. 4.6. Specimens of normal and tumor human breast tissues were obtained from patients who have undergone surgery at Memorial Sloan Kettering Cancer Center (MSKCC). The samples averaged a dimension of ~0.5×0.5×1.0 cm^3, were stored at 4°C and measured within 72 hrs after excision. Normal and tumor tissues from the same patient were paired and labeled for comparison. No chemical treatment was done to the samples prior to the measurements. A total of four sample pairs were measured. To check for reproducibility, several spots were selected and labeled within each specimen, and 10 to 20 measurements were averaged for each single spot. After the measurements, the samples were sent to Dr. H. E. Savage at MSKCC for histology and pathology analysis.

Steady state SHG/TPF lineshape and intensity were measured as a function of the emission wavelength. The typical spectral responses between 300-400 nm for normal and tumor breast tissues under 625 nm femtosecond laser excitation are displayed in Fig. 5.15.

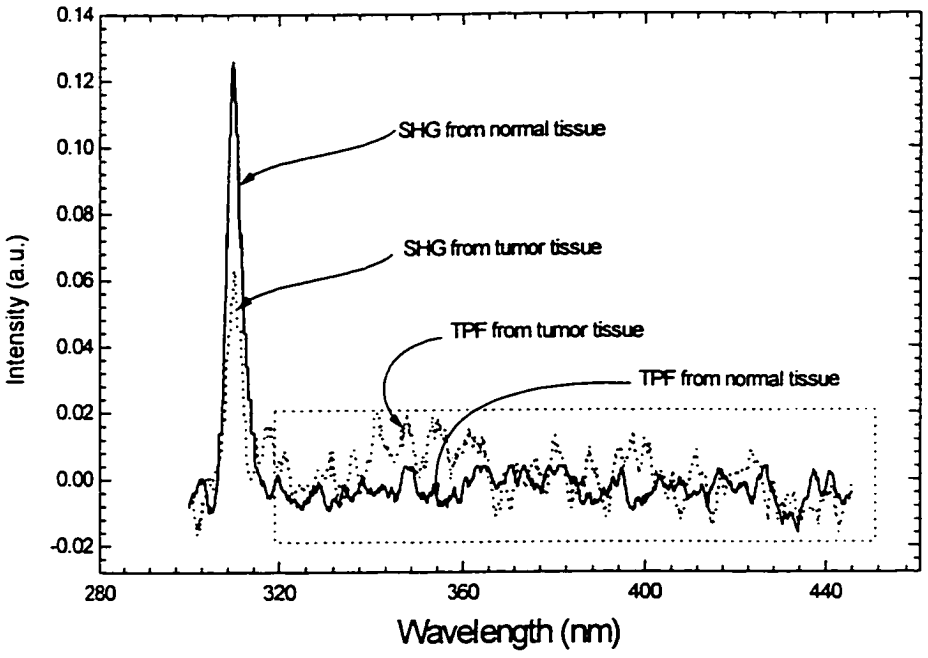

Fig. 5.15 TPF and SHG spectra of human breast normal and tumor tissues under 625nm, 100fs laser pulse excitation.

Three salient features were observed:

(i) Both normal and tumor breast tissues exhibited SHG at 312 nm and TPF intensity maxima at approximately 345 nm.

(ii) The SHG intensity at 312 nm of normal breast tissue was larger than that of its tumor counterpart by a factor varying between 1.3 to 2 times.

(iii) The TPF intensity around 340 nm of tumor breast tissue was larger than that of normal tissue by a factor varying between 1.3 to 1.5 times.

The peak intensities of SHG and TPF (tryptophan band) thus indicated differences between tissue states. The intensity ratio at 312 nm and 345 nm (I_{312}/I_{345}) is therefore a possible optical marker for discriminating normal and cancerous tissues. A number of factors could contribute to the observed differences. From the view of chemical changes, the elevated Trp fluorescence from tumor tissues might have resulted from byproduct of tumor growth, which has been also confirmed by the single photon excited fluorescence measurement.[12] On the other hand, morphological changes are mostly reflected by SHG whose lower signal strength might result from the disorganization at the fine structural levels in the tumor region. To test the structural correlation, spectral lineshapes from cell culture samples were measured under the same experimental setup. Human head and neck malignant cell line 1483 samples and SV40 virus infected stem cell samples were supplied by Dr. P. G. Sacks and Prof. M. L. Steinberg from MSKCC and The Biochemistry Laboratory at CCNY, respectively.[20,21] Trypsin washed cell suspension and cell cultures growing on collagen matrices obtained by scraping method were prepared at MSKCC. The centrifuged SV40 virus infected stem cell pellet was prepared in the biochemistry laboratory at CCNY. Although the TPF signals in the designated Trp band were confirmed by the

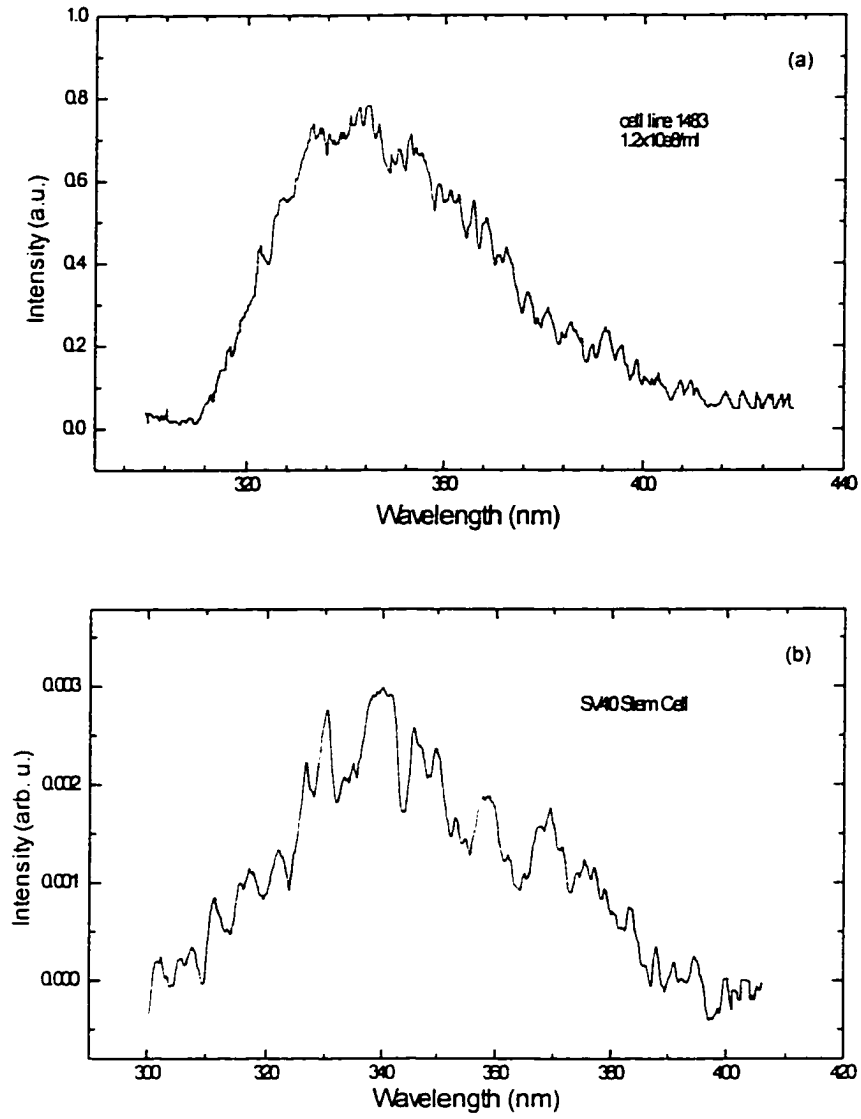

Fig. 5.16 TPF spectra of (a) malignant head and neck epithelial cell line 1483, and (b) SV40 infected stem cells, excited with 100fs, 625nm laser pulses. The difference between spectra of cell and tissue is partially due to the self-absorption effect in the tissue.

spectrum, the SH signals from all cell culture samples were found below the detection limit of the instrument. Thus the SHG components at 312 nm are absent in the spectra shown in Fig. 5.16. These observations were expected based upon the differences in cell organization, cell density and composition changes when samples were changed from tissue to cell cultures. The structure-associated contribution to SHG in the bulk region was greatly reduced in cell culture samples, where only surface SHG at cell membrane and intracellular interfacial structures play roles in signal generation.

5.5.3 Second Harmonic Tomography of Normal and Diseased Human Breast Tissues

In addition to spectroscopic analysis, the spatial distribution of NLO signal was investigated in normal and diseased human breast tissues as a function of the tissue's three dimensional positions using the laser scanning technique. Second harmonic tomography was obtained by photoexciting the breast tissue samples using femtosecond laser pulses from a Ti:Sapphire laser oscillator, and recording the NLO signal intensity along the (x, y, z) coordinates. A similar imaging system described in Fig. 5.8 was used for the investigation. The average power delivered to the sample through a 20× microscope objective lens was approximately 80 mW, at a wavelength of 780 nm and a pulse repetition rate of 76 MHz.

Normal and tumor human breast tissues were supplied by The National Disease Research Interchange Program (NDRI). The samples were handled following a similar procedure as described in section 6.2. Because blood content in tissue specimens generates strong hemoglobin absorption at 400 nm, the laser wavelength was tuned away from the center wavelength 800 nm to 780 nm.

Figs. 5.17 to 5.20 display the results of pseudo color SH images obtained from normal and tumor human breast tissues. In these lateral scanned images, the tumor tissues exhibited a lower SH intensity as compared to their normal counterparts. An image obtained from a section of breast tissue consisting of partial tumor (upper right quadrant) regions and partial normal (left side) regions is shown in Fig. 5.19. The tumor region was recognized by an area with a lower SH intensity while the normal region was marked by a higher SH intensity response. The corresponding axially scanned depth SH images at the two corresponding regions are displayed in Figs. 5.20a and b, respectively.

The microstructural NLO signal appeared to be quite fluctuating within each tumor or normal region, which indicated the heterogeneity in tissue composition as well as structural organization on a microscopic level. Human breast is one of the most complex organs since it comprises of various structural components such as glandular, adipose, ductal, and fibrous constituents. The chemical and physical inhomogenity poses difficulties for differentiating the normal state from the tumor state and subjects the measurements to uncertainty. For a total number of 10 pairs of specimens, the average percentage of SH intensity from normal breast tissues to be larger than that of tumor tissues was estimated approximately to be 65%. About 25% of the measurements showed comparable responses of SH intensity from both tissue states, and 10% showed reversed responses as compared to the results in Figs. 5.17 to 5.19, i.e., the SH intensity in normal tissues was lower than that in the tumor tissues.

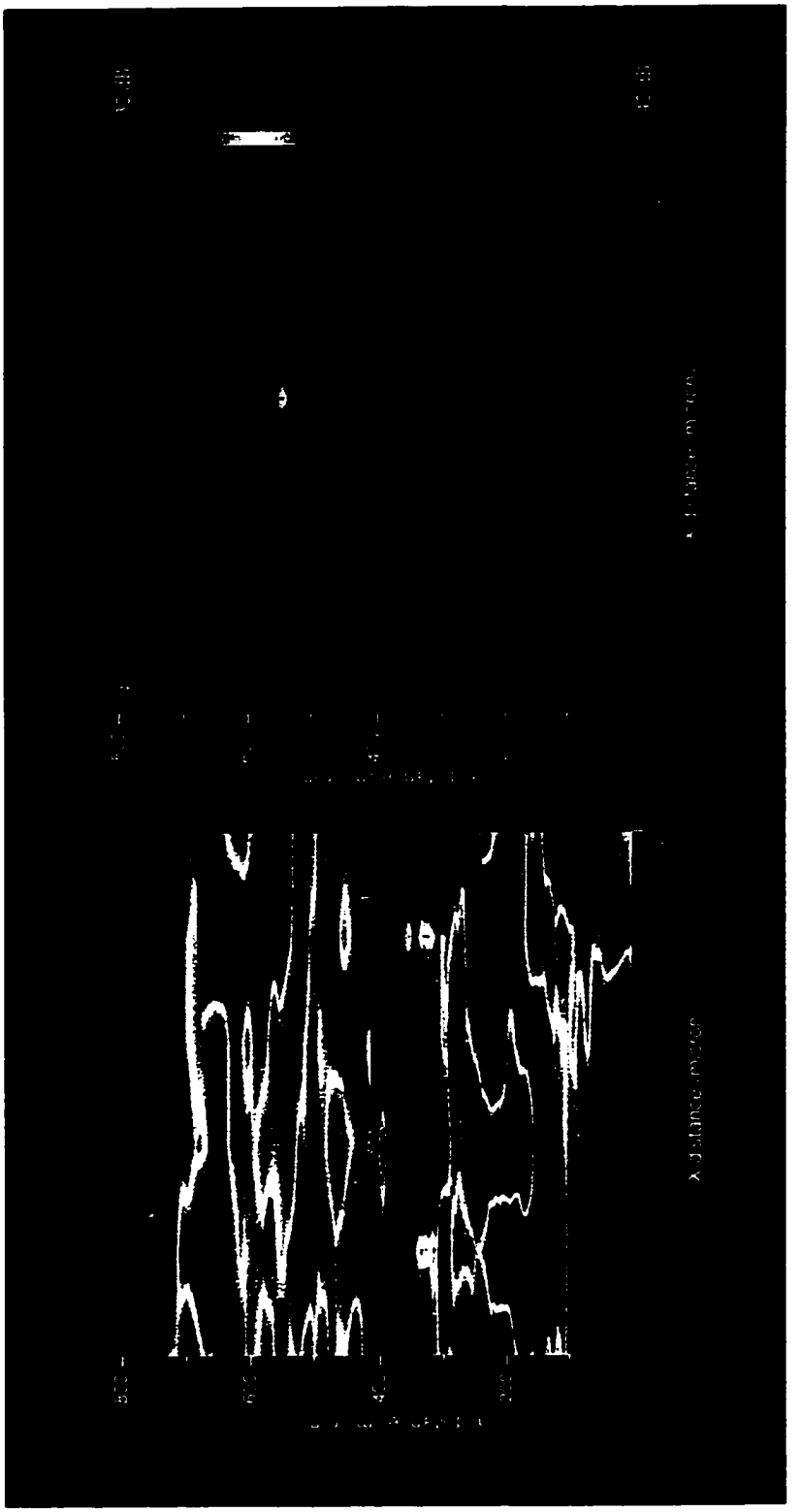

Fig. 5.17 Second harmonic imaging of normal and tumor human breast tissues: (a) the SH intensity map of normal breast tissue, and (b) the SH intensity map of cancer breast tissue, under 780 nm femtosecond laser excitation.

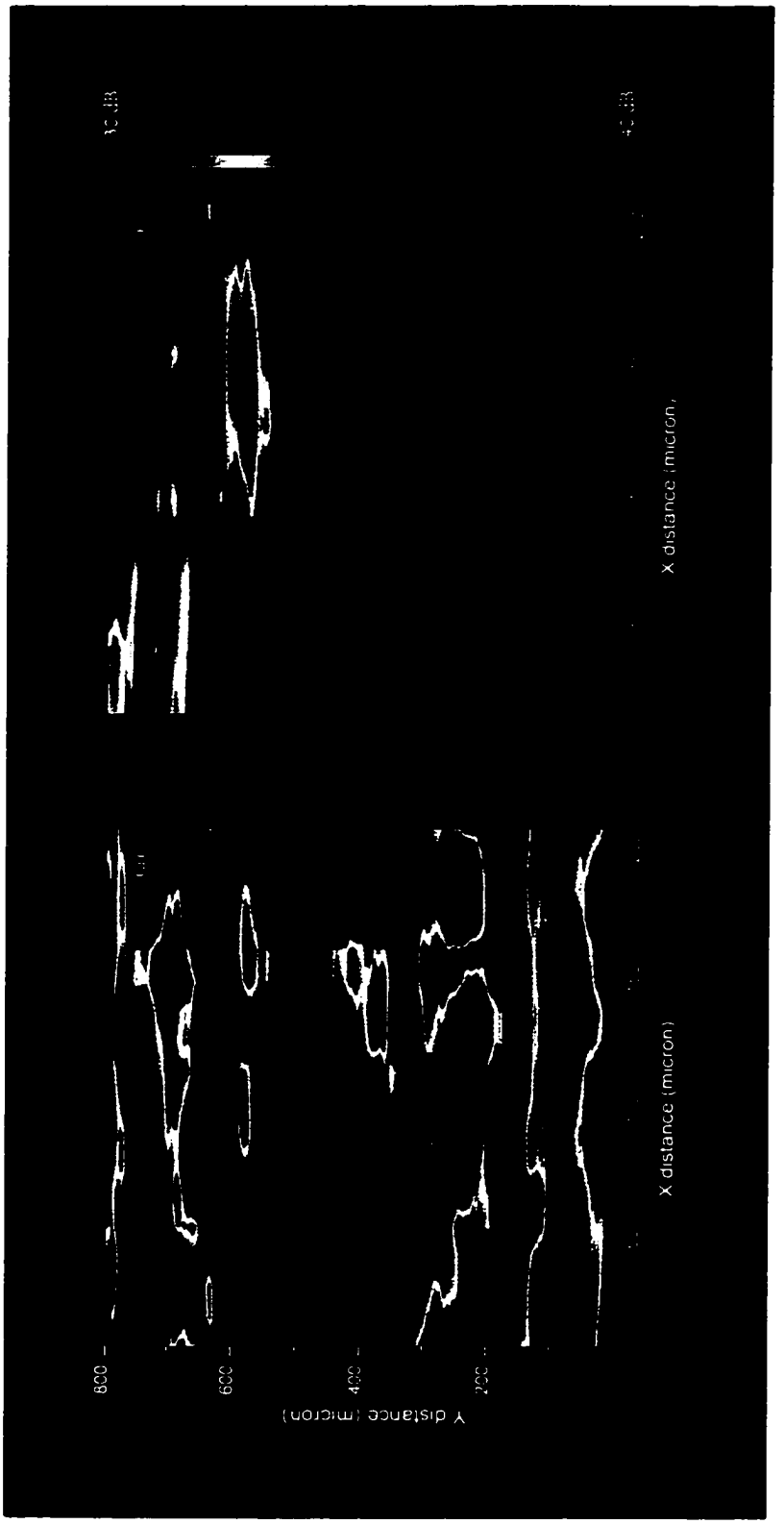

Fig. 5.18 Second harmonic imaging of normal and tumor human breast tissues: (a) the SH intensity map of normal breast tissue, and (b) the SH intensity map of cancer breast tissue, under 780 nm femtosecond laser excitation.

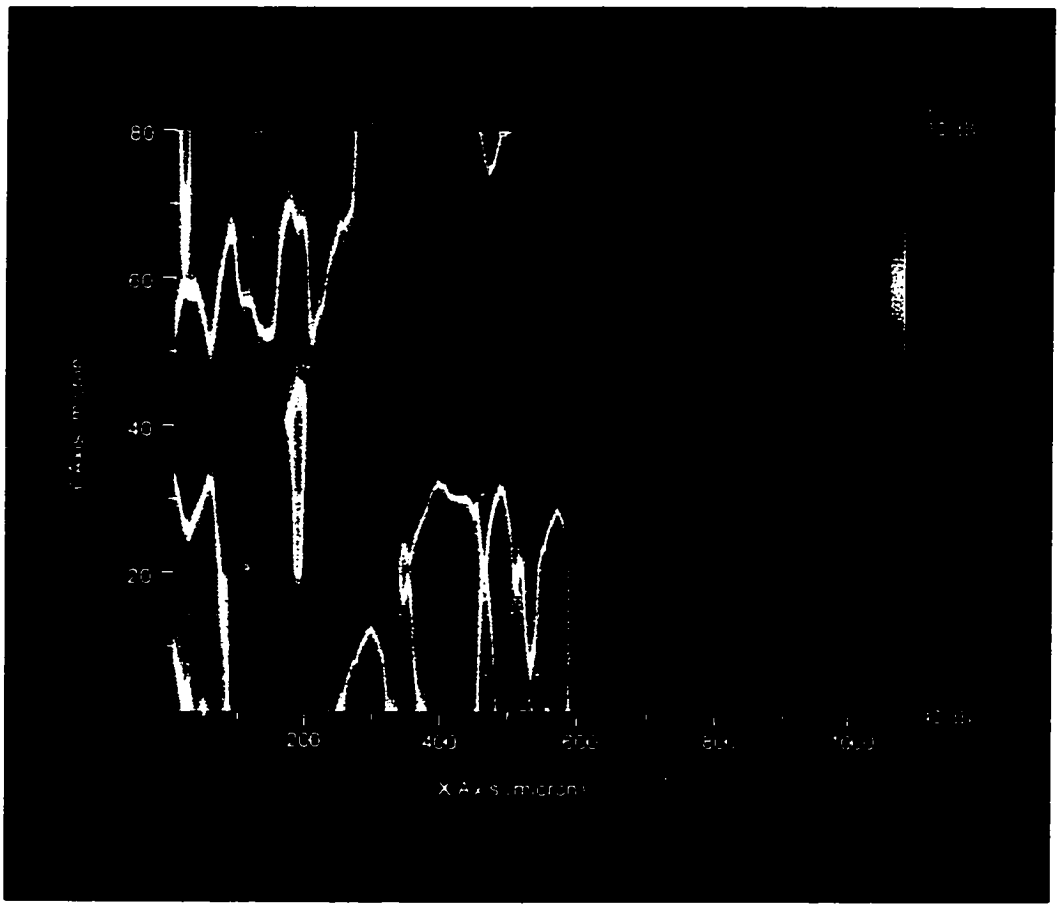

Fig. 5.19 Laterally scanned second harmonic image of breast tissue consisting of partial tumor (upper right quadrant) and partial normal (left side) regions.

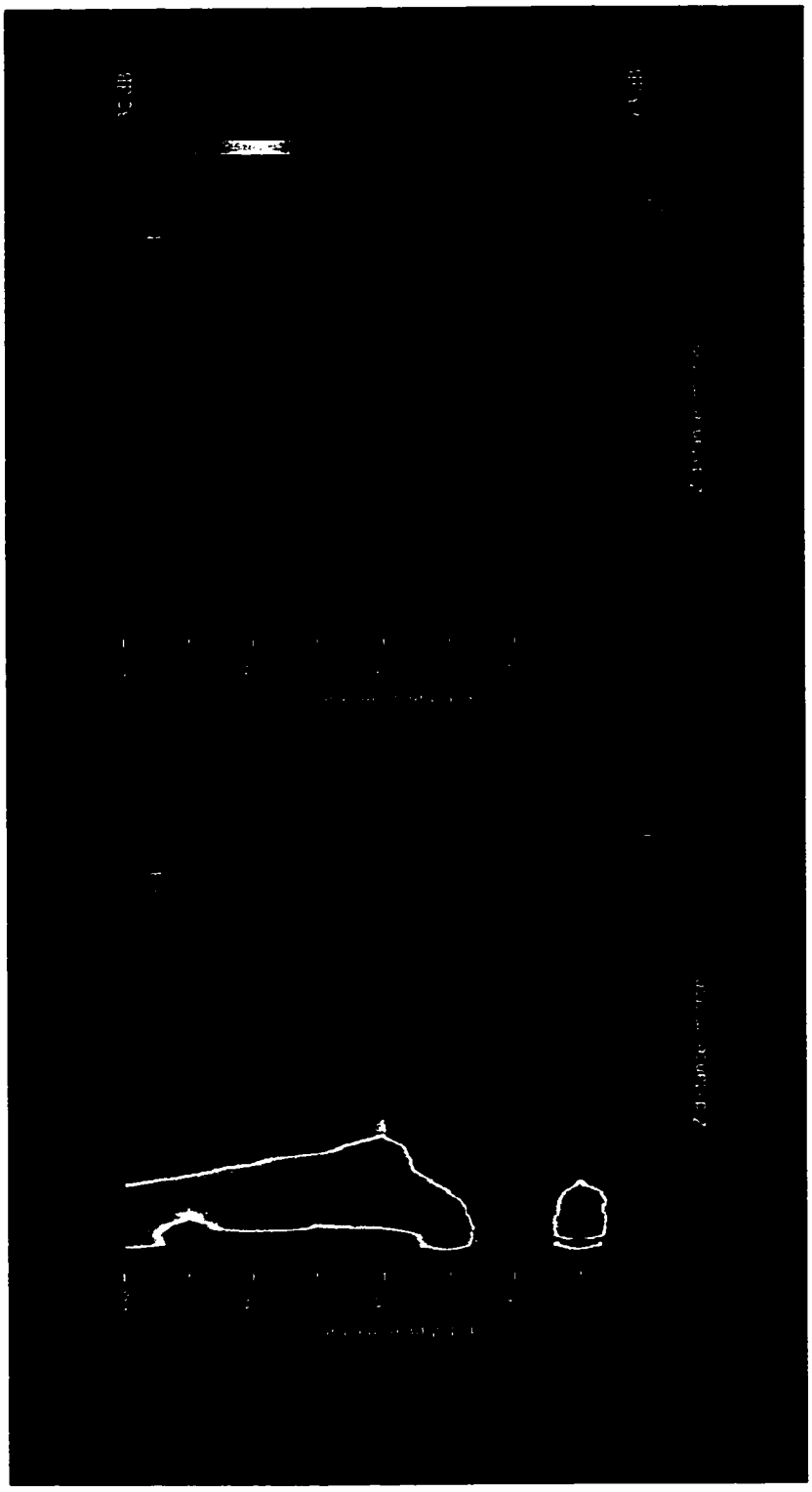

Fig. 5.20 Axially scanned second harmonic intensity profiles of (a) normal breast tissue, and (b) cancer breast tissue under 780 nm, 120 fs laser excitation.

5.5.4 Subsurface Tumor Progression Evaluated by Second Harmonic Tomography

One of the interesting biological systems for studying SH tomography is the skin and mucosa tissues that line up both the external surface and internal cavities of human and animal bodies. These systems are made up of multiple interfacial layers and sub-layers consisting of cells with different types and functions. Fig. 5.21 displays the pictorial arrangements of the cross sectional human skin and Synian hamster cheek pouch mucosa, respectively. Fig. 5.22 displays the cross sectional micrographs of human colon mucosa and human esophagus wall.

Human skin (Fig. 5.21a) is divided into two main layers: the epidermis and the dermis. Several sub-layers exist in the epidermal region. Starting at the top these are: (1) the stratum corneum of keratin consisting of flattened dead cells, (2) the stratum granulosum containing many granules, (3) the stratum spinosum consisting of cells with prickly appearance, and (4) the stratum germinatum or the basal layer. The thickness of the epidermis and dermis is ~100-200 μm and ~3 mm, respectively. Table 5.1 lists some typical values of the epidermal thickness of the skin tissue at different locations.[23]

The normal hamster cheek pouch (Fig. 5.21b) has five distinct layers. Starting at the lumen surface and traversing through the pouch these are: 1) a surface layer of keratin, 2) an epithelial layer consisting of a basal cell layer of flat stratified squamous epithelium without rete pegs and a supra-basal layer that grows over time, 3) a submucosa of dense fibrous connective tissues, 4) a layer of longitudinal striated muscle fibers, and 5) a layer of loose areolar connective tissues. The basal layer produces cells.

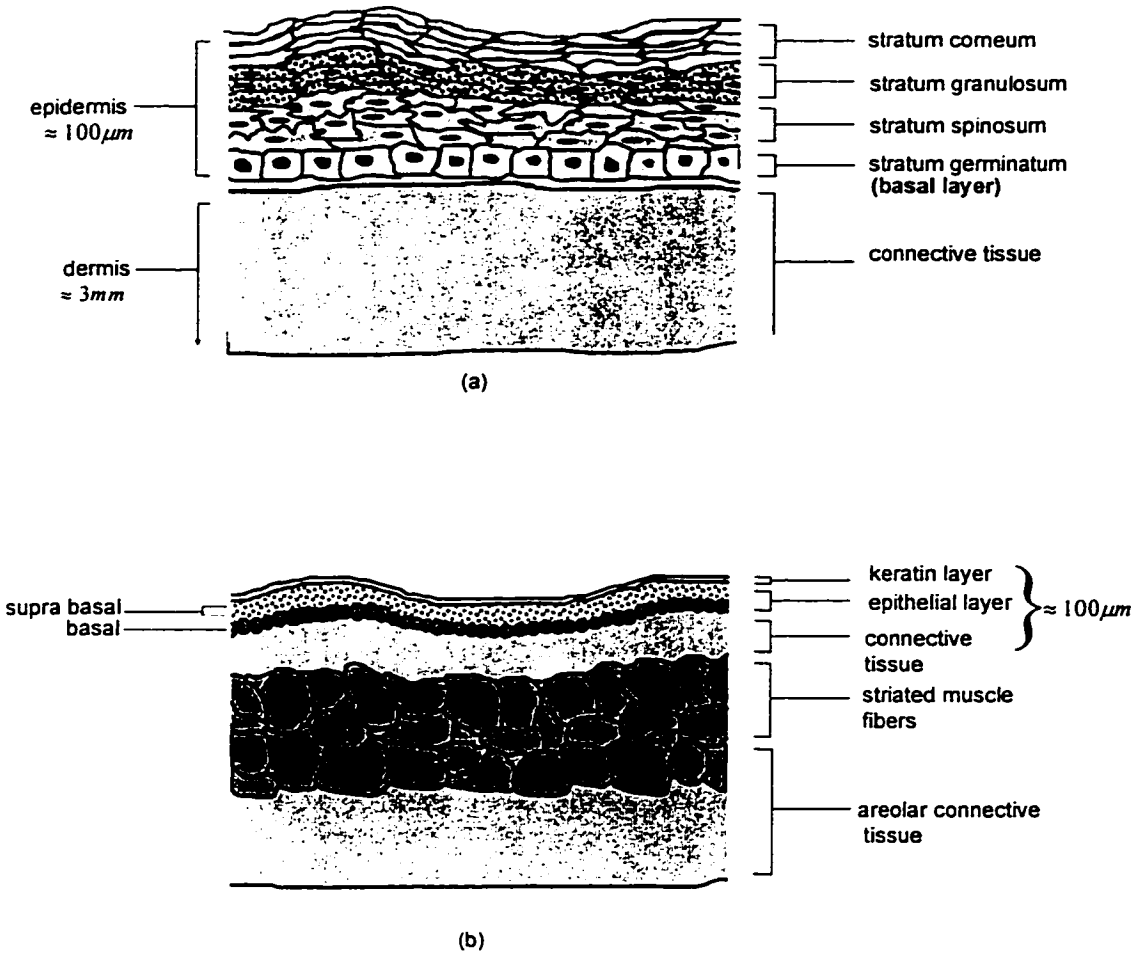

Fig. 5.21 (a) pictorial cross sectional diagram of human arm skin, and (b) cross sectional diagram of hamster cheek pouch mucosa.

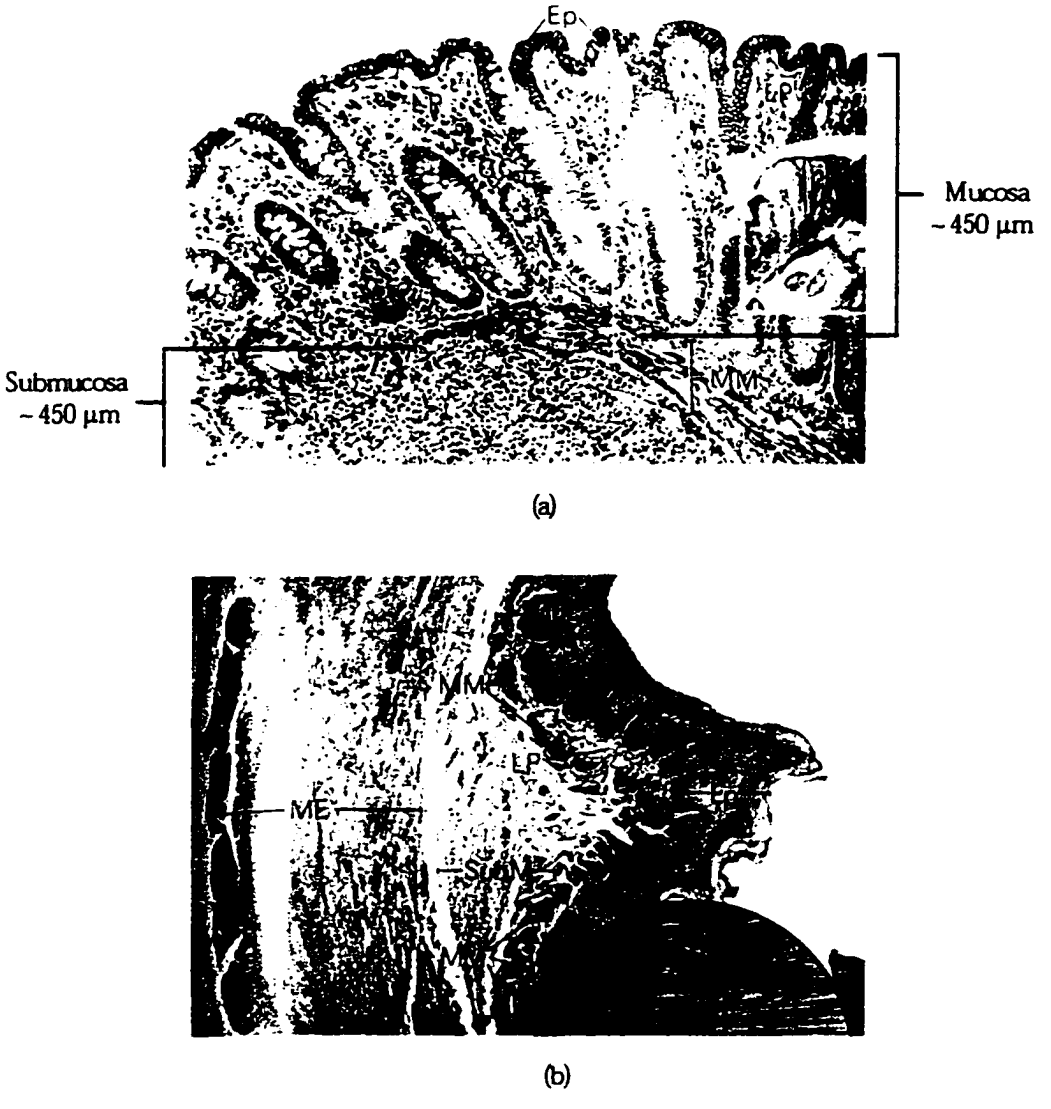

Fig. 5. 22 Light micrographs of (a), colon mucosa. Ep, epithelium; Lp, lamina propria; GC, goblet cell; MM, muscularis mucosa.(b), monkey esophagus. Ep, stratified squamous epithelium; Muc, mucosa; LP, lamina propria; MM, muscularis mucosa; SubM, submucosa; ME, muscularis externa; L, longitudinal layer of muscularis externa; StM, striated muscle.

After M. H. Ross and E. J. Reith, "Histology", Harper & Row Publishers, J. B. Lippincott Co., New York (1972).

Table 5.1 Typical epidermal thickness of human skin tissues.[22]

Tissues	Epidermal thickness*
Eye lids	50 - 60 μm
Cheeks	90 - 220 μm
Arms	100 - 150 μm
Colon	450 μm
Esophagus	300 μm
Palms and Soles	0.5 - 1.5 mm

* also approximately indicates the location of the basal cell layer from the top surface.

The top region of human colon tissue (Fig. 5.22a) is divided into mucosa and sub-mucosa layers. The mucosa layer consists of oval shaped crypts surrounded by lamina propria and epithelial cells. The sub-mucosa layer contains mainly collagen. The mucosa and sub-mucosa are approximately 450 μm in thickness in each section.

The esophagus wall is divided into mucosa and submucosa layers (Fig. 5.22b). The mucosa consists of stratified squamous epithelium, a lamina propria, and a muscularis mucosae. The basal layer of the epithelium stains intensely, appearing as a dark band. The submucosa consists of irregular dense connective tissue which contains the larger blood vessels and nerves.

The basal layer located in the stratified squamous epithelium is signified by the round shaped basal cells which are continuously differentiating, providing a constant supply of new cells for the upper strata. This cell layer is of particular importance as it

is the site where mutated cells begin to grow uncontrollably resulting carcinoma, the most frequently occurring form of cancer.

The hamster cheek pouch mucosa was selected as an experimental model for studying SH tomography to detect tumor progression. Since carcinoma originating from the epithelium first develops at the basal cell layer, the focus in this study was designed to locate the layered structure and its thickness in the epithelial region. These features were investigated by image mapping the backscattered SH intensity from various hamster cheek pouch mucosas at controlled and time extended carcinogen treatment stages.

The hamster cheek pouch carcinogenesis process was accomplished using the method developed by Salley.[23] The hamster cheek pouches were painted thrice weekly with mineral oil containing 0.5% dimethyl-benzanthracene (DMBA) or with mineral oil alone. At the time points, eight and fourteen weeks after the start of the painting, the hamsters were euthanized by CO_2 asphyxiation, the cheek pouches removed, cut down the midline, placed on filter paper with the lumen side up and then both transferred to 10% buffered formalin for a minimum of 48 hours. Prior to optical analysis, the cheek pouch tissue was washed in 0.01M phosphate buffered saline pH 7.0.

The detailed histological changes in the hamster cheek pouch over time under treatment with DMBA have been described by Salley in 1954.[23] With increased time of treatment, the cheek pouch progresses through distinct changes that include hyperplasia, benign papilloma, squamous carcinoma *in situ* and squamous cell carcinoma with local invasion and metastasis. The cross sectional microphotographs obtained by the standard hematoxylin-eosin histology procedure document these

Fig. 5.23 (a), hematoxyln-eosin stain of a cross section of a hamster cheek pouch from an 8 week saline control animal; (b), hematoxyln-eosin stain of a cross section of a hamster cheek pouch from an animal that had its cheek pouch painted with mineral oil containing 0.5% DMBA three times a week for 8 weeks; and (c), hematoxyln-eosin stain of a cross section of a hamster cheek pouch from an animal that had its cheek pouch painted with mineral oil containing 0.5% DMBA three times a week for 14 weeks.

changes in Figs. 5.23a-c. These histological graphs reveal tumor progression changes in the epithelial layer. The prominent change happens at the basal/supra-basal layer which develops over time under treatment with DMBA, extending from normal (Fig. 5.23a) of 2-4 cell layers to 15-20 cell layers thick at fourteen weeks of DMBA treatment (Fig. 5.23c).[23]

Using the scanning setup described in section 5.3, the hamster mucosa samples were mounted in a glass cuvette with the lumen surface facing the microscope objective lens in the x-y plane. The SH signal was scanned along the axial depth by transversing the laser focus from the keratin layer down to an axial position ~300 μm. According to histological analysis, this distance starts at the epithelial layer up to the areolar connective tissue.

A typical y-z plane scanned pseudo color SH image obtained from the controlled normal cheek pouch tissue is displayed in Fig. 5.24a. The cross sectional SH images obtained from DMBA treated cheek pouches at 8 and 14 week carcinogensis time points are displayed in Figs. 5.24b and c, respectively. A spatial correlation with the respective histology graphs indicates that the epithelial (basal/supra-basal) layer is marked by the yellow and red regions in the SH images. These yellow-red regions gradually thicken corresponding to the time period of carcinogen treatment. One would also notice the spatial width variations in the green regions from the controlled (Fig. 5.24a), dysplasia (Fig. 5.24b) to the cancerous (Fig. 5.24c) stages. These optically resolved multi-interfacial regions are believed to arise from the symmetry dependence on the tissue structures of the second harmonic signal. This spatial correlation between the SH map and the histology images indicates the potential of SH tomography as a noninvasive modality for *in vivo* detection of cancers with epithelial origins.[25]

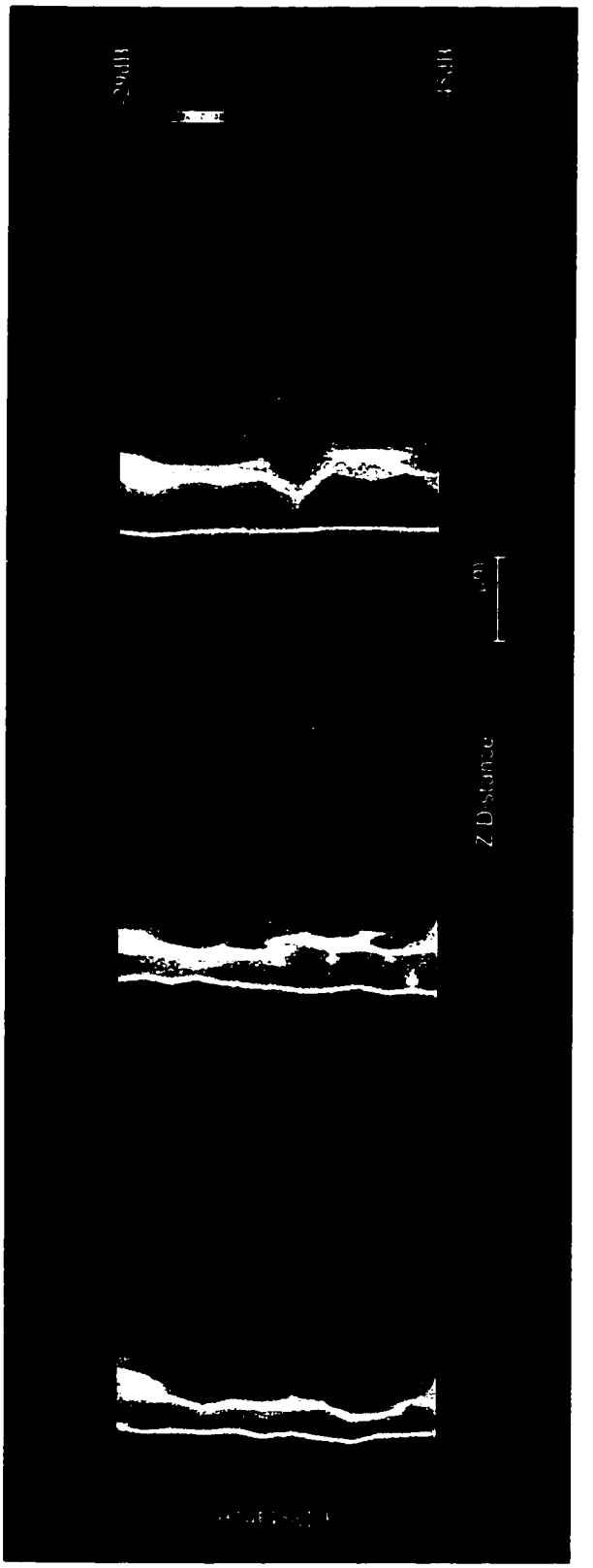

Fig. 5.24 Two dimensional tomographic second harmonic images of (a), normal hamster cheek pouch tissue; (b) hamster cheek pouch tissue under 8 weeks of carcinogen treatment; and (c) hamster cheek pouch tissue under 14 weeks of carcinogen treatment. The images were obtained with 800 nm femtosecond laser excitation.

References

1. For a brief review, techniques in microscopy are summarized in Fig. 5.1.
2. C. J. R. Sheppard, J N. Gannaway, R. Kompfner, and D. Walsh, IEEE Trans. QD-13, 100D (1977).
3. I. Freund, M. Deutsch, and A. Sprecher. Biophys. J. 50, 693 (1986).
4. Min Gu and C. J. R. Sheppard, J. of Microsc. 177, 128 (1994).
5. J. Manni, Biophotonics International, Jan./Feb. Issue, 66 (1996).
6. D. R. Sandison and W. W. Webb, Appl. Opt. 33, 603 (1994).
7. Min Gu and C. J. R. Sheppard, J. Opt. Am. A. 9, 151 (1992). P. T. C. So, T. French, W. M. Yu, K. M. Berland, C. Y. Dong, and E. Gratton, "*Fluorescence Imaging Spectroscopy and Microscopy*", Chapter 11, John Wiley & Sons , New York (1996).
8. Yici Guo, P. P. Ho, H. E. Savage, D. Harris, P. Sacks, S. Schantz, F. Liu, N. Zhadin, and R. R. Alfano, Opt. Lett. 22, 1323 (1997).
9. Y. R. Shen, "*Principles of Nonlinear Optics*", Chapter 12, John Wiley and Sons, New York (1984).
10. R. A. Weinberg, Scientific American Sept., 62 (1996).
11. R. R. Alfano, D. B. Tata, J. Cordero, P. Tomashefsky, F. W. Longo, and M. Alfano, IEEE J. Quant. Electron. QE-20, 1507 (1984).
12. R. R. Alfano, G. C. Tang, A. Pradhan, W. Lam, D. C. Choy, and E. Opher, IEEE J. Quant. Electron. QE-23, 1806 (1987).
13. R. R. Alfano, A. Pradham, and G. C. Tang, J. of Opt. Soc. Am. B. 6, 1015 (1989).
14. R. Richards-Kortum, R. P. Rava, R. E. Petras, M. Fitzmaurice, M. Sivak, and M. S. Feld, Photochem. Photobiol. 50, 777 (1991).
15. J. Hung, S. Lam, J. C. Le Riche, and B. Palcic, Laser Surg. Med. 11, 99 (1991).

16. Yuanlong Yang, G. C. Tang, M. Bessler, and R. R. Alfano, Laser in the Life Sci. 6(4), 259 (1995).

17. W. Denk, J. H. Strickler, and W. W. Webb, Science **248**, 73 (1990).

18. D. Huang, E. A. Swanson, C. P. Lin, J. S. Schuman, W. G. Stinson, W. Chang, M R. Hee, T. Flotte, K. Gregory, C. A. Puliafito, and J. G. Fujimoto, Science, **254**, 1178 (1991).

19. E. A. Swanson, J. A. Izatt, M. R. Hee, D. Huang, C. P. Lin, J. S. Schuman, D. A. Puliafito, and J. G. Fujimoto, Opt. Lett. **18**, 1864 (1993).

20. P. G. Sacks, H. E. Savage, J. Levine, V. R. Kolli, R. R. Alfano, and S. P. Schantz, Cancer Letts. **104**, 171 (1996).

21. M. L. Steinberg and V. Defendi, Proc. Natl. Acad. Sci. **76**, 801 (1979).

22. H. E. Savage, New York Eye and Ear Infirmary, personal communication.

23. J. J. Salley, J. D. Res. **33**(2), 253 (1954).

24. H. E. Savage, New York Eye and Ear Infirmary, personal communication.

25. Yici Guo, Howard E. Savage, Feng Liu, Stimson P. Schantz, P. P. Ho, and R. R. Alfano, submitted to Cancer Research.

Chapter Six

Second Harmonic Microscopy of Biological Tissues and Cells

This chapter presents second harmonic microscopy of modeled objects, biological tissues and cells using the CCD camera based microscope. Second harmonic images obtained by this technique have demonstrated its advantages for noninvasive, direct, and high resolving power studies of microscopic and cellular structures over conventional linear imaging methods.

6.1 CCD Camera Based Second Harmonic Microscopy

The charge-coupled device (CCD) is a high resolution and low noise 2-D imager for quantitative imaging acquisitions.[1] The CCD camera achieves its performance by employing signal processors, solid-state coolers, precision digitizers, and high speed digital controllers. The most common material making up the CCD is silicon, based upon its sensitivity to electromagnetic radiation in the visible spectrum. The special coating of Metachrom[1] extends the response spectrum down to the UV region. To measure the electronic charge produced by incident photons, a potential well is used as a collecting unit. A thin layer of silicon dioxide is grown on a section of silicon. A conductive gate structure is applied over the oxide. Applying a positive electric potential to the gate creates a depletion region where free electrons generated by the incoming photons can be stored in a register. On the other hand, electrons freed by thermal agitation or high energy particles are indistinguishable from those generated by photon interaction. These non-photon induced charge/dark electrons degrade the detection limit of real photo-signals.

When a CCD imager is exposed to light, charge accumulates over an extended period of time in the potential wells of the parallel register. The total amount of charge is proportional to the product of the light intensity and the exposure time. After an integration, the stored charge packets in the parallel register are shifted by one pixel towards the serial register. Once in the serial register, charge packets are individually shifted toward the output amplifier which produces a signal proportional to the charge in each packet. When the charge is emptied from the serial register, a second row of charge repeats the process until all the charge is shifted out of the parallel register. The efficient transport of charge from the photo-sites to the output amplifier is important, because the charge from wells located far from the output amplifier must undergo hundreds of transfers.

The use of the CCD camera brings together several advantages over scanning instruments. First, direct images are acquired, for there are no electronic or mechanical scanning parts and descanning units, which simplifies the system alignment and reduces size and cost.[2-4] Second, image processing complexity and time are greatly reduced due to the two dimensional array detection layout and image processing software development. Third, the spatial resolution of the system is not restricted by the focal spot of the objective lens, thus enabling structures within the laser focus to be resolved with a resolution determined by the diffraction limit. Fourth, variable magnification can be easily achieved which provides the ability to accommodate different sizes of the objects and to study samples with a desired scale.

6.2 Experimental Methods

A CCD camera based reflection SH/TPF microscope is schematically shown in Fig. 6.1. The excitation source was either the pulse train from a Ti:Sapphire laser oscillator or the pulse train from a regenerative amplifier that subsequently amplified

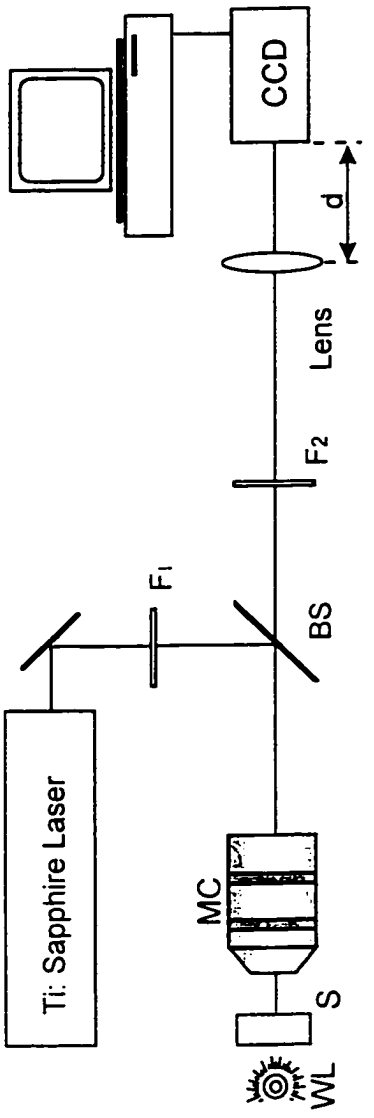

Fig. 6.1 Experimental setup of reflection mode SH microscope. BS, dichroic beam splitter; MC, microscope objective lens; S, sample; F1 and F2, long and short pass filters, respectively; CCD, charge coupled device camera. Apmlification can be adjusted by changing the distance between focusing lens and CCD camera.

the seeding output from the oscillator. The energies carried per pulse from the output of the oscillator and the amplifier were ~nJ and ~mJ, respectively. The wavelength of the excitation light was centered at 800 nm, and the pulse repetition rates of the oscillator and the regenerative amplifier were 76 MHz and 250 kHz, respectively. The laser beam was directed by a dichroic beam splitter and focused by a 20× or a 5× microscope objective lens onto the sample. The SH/TPF signal emitted from the focal spot in the sample was transmitted through the beam splitter, and imaged by a camera lens onto the CCD camera. An incoherent white light source positioned behind the sample was used to illuminate the sample in a transmission mode and to generate images for comparison with the reflection mode linear and second harmonic images. The position of the camera lens relative to the image plane at the CCD camera was adjustable and thus variable magnification can be achieved. The average power at the sample site was between 100 to 200 mW. The average exposure time for capturing a single image was 20 second.

The samples used for the investigation were micro-polystyrene beads, microcrystal KDP powder particles, frozen then thawed chicken muscle tissues, sections of the crust and the fresh inner portion of a onion, and fixed amoeba cells.

6.3 Results and Discussion

The experimental results obtained using the second harmonic microscope for the samples described above are presented in Fig. 6.2 to Fig. 6.9.

The typical transmission linear and backscattered second harmonic images obtained from unstained polystyrene beads are displayed in Figs. 6.2 to Figs. 6.4. These beads having a nominal diameter ~11.9 μm were attached to an optical slide. The sample was first imaged under transillumination mode using white light source (Fig.

6.2a). Each bead formed a dark shadow with a bright spot at its center. The bright spot is due to the diffraction from a disk aperture. The corresponding image is shown in Fig. 6.2a. The reflection second harmonic image obtained under pulsed laser excitation for the same sample is shown in Fig. 6.2b, where the spherical shape of the microscopic bead is clearly resolved. The best resolution under this imaging setting is lower than the size of the microsphere which is estimated to be 3-4 μm. The magnification of the microscope with a 20× objective lens for acquiring these images was set at 110.

In Fig. 6.3, several polystyrene beads were imaged as the magnification of the microscope was adjusted to 11, while other imaging parameters were kept the same as in Fig. 6.2. The transmission mode white light image is shown in Fig. 6.3a, and the reflection second harmonic image under pulsed laser excitation is shown in Fig. 6.3b, in which structures of three individual beads were resolved. These images demonstrated the flexibility of the imaging setup to accommodate objects at different scales.

In order to further investigate the resolving power of the SH microscope, results were compared for (a) white light imaging under transmission mode; (b) laser imaging at fundamental wavelength under reflection mode; and (c) second harmonic imaging using laser excitation under reflection mode. The images of polystyrene microspheres for condition a, b and c are shown in Figs. 6.4a-c, respectively. The shape and structure of the objects are clearly resolved in the second harmonic images as evidenced by a comparison between the SH image in Fig. 6.4c and the transmission white light image in Fig. 6.4a. The linear reflectance image illuminated and detected at the fundamental wavelength in Fig. 6.4b exhibits interference patterns obscuring the bead's spherical shape. These interference patterns are clearly absent in the SH image, which indicates the advantage of the nonlinear optical technique. In addition, a bright background (right side of Fig. 6.4c) can be observed in the linear reflection image at the

laser wavelength. This bright background came from the laser spot partially incident on the optical slide that is not covered by the microspheres. Clearly, the SH image has eliminated this background. Figs. 6.4d,e demonstrate another set of white light transmission and its respective second harmonic images from a cluster of beads, in which the geometric shape and positions of the microspheres are clearly matched between the two images.

The images of chicken muscle tissue placed between two optical slides are shown in Fig. 6.5. Fig. 6.5a shows the transmission mode image of the tissue sample under white light illumination when the tissue fibers were parallel to the optical slide. Fig. 6.5b shows the transmission mode images of the tissue sample when the tissue fibers were perpendicular to the optical slide. The magnification of the microscope in these images was 71 with a 20× objective lens. Figs. 6.5c,d are the corresponding backscattered second harmonic images that match to the positions in Figs. 6.5a,b. These two SH images display different features corresponding to the longitudinal and cross sectional substructures inside the muscle fiber. The detailed structure resolved from the SH image shows micro scale bright regions corresponding to the tissue regions possessing large $\chi^{(2)}$ responses. These large SH signals might be generated from those substructures that consist of more organized asymmetric molecules or substructures that have a larger scattering coefficient at the second harmonic wavelength.

Fig. 6.6 shows the images obtained from a layer of onion crust. The transmission mode images under white light illumination are shown in Figs. 6.6a, b. In these linear images, the selected onion cells were observed with tiny water bubbles attached to the center of the cell. The water bubbles had an estimated size of ~12 μm. The backscattered second harmonic images are displayed in Figs. 6.6c-g. These second harmonic images correspond to different structures as the laser focus was translated

across the onion cell. In Figs. 6.6c-e the water bubbles are resolved. The total magnification of the microscope was 9.4 using a 20× objective lens.

Fig. 6.7 shows the backscattered second harmonic images obtained from a section of fresh onion. Figs. 6.7a-d show structure changes as the laser focus was translated across the sample. The thickness of the sample was about 1 mm, which obstructed the transmission linear image. Amplification was adjusted at 12.

Fig. 6.8 shows the images obtained from amoeba cells. Figs. 6.8a,b are the transmission linear images with white light used as the illumination source. Fig. 6.8b shows the laser focus spot on one of the cells when the image was acquired at the fundamental wavelength in addition to the white light illumination. The corresponding backscattered second harmonic image is displayed in Fig. 6.8c. The cellular structures have been resolved from this image. The magnification of the microscope with a 5× objective lens is 6.3. Figs. 6.8d,e are the linear transmission and backscattered SH images obtained from a second amoeba cell under same image setup. In Figs. 6.8f-h, the magnification is adjusted to 31.5. Figs. 6.8f,g are the linear transmission images while Fig. 6.8h is the corresponding second harmonic image.

Fig. 6.9 shows images of cellular structures in an amoeba cell when the system employs a 20× objective lens with a magnification of 178. Fig. 6.9a corresponds to the linear transmission image under white light illumination. Fig. 6.9b is the reflection SH image from part of the ameba cell. Intracellular structures of granules of hydrocarbon and lipids within the laser focal region have been resolved. The frame in Fig. 6.9a indicates the imaged area of the amoeba cell.

Directly recorded 2D backscattered SH images obtained using a CCD camera have demonstrated the capability of this nonscanning technique in biological and medical applications. Compared with the transmission white light imaging mode, back scattered image acquisition has the ability to provide noninvasive visualization of

structures that can be dynamically and functionally interrogated over time. Because the image formation wavelength in NLO methods is at half or significantly shorter than the fundamental wavelength, advantage in eliminating diffraction interference has been observed. Using the current image setting parameters, i.e. a 20× objective lens and a magnification of ~100 -200, substructures on the scale of ~3 - 4 μm can be resolved to provide more structural details than the conventional linear imaging methods.

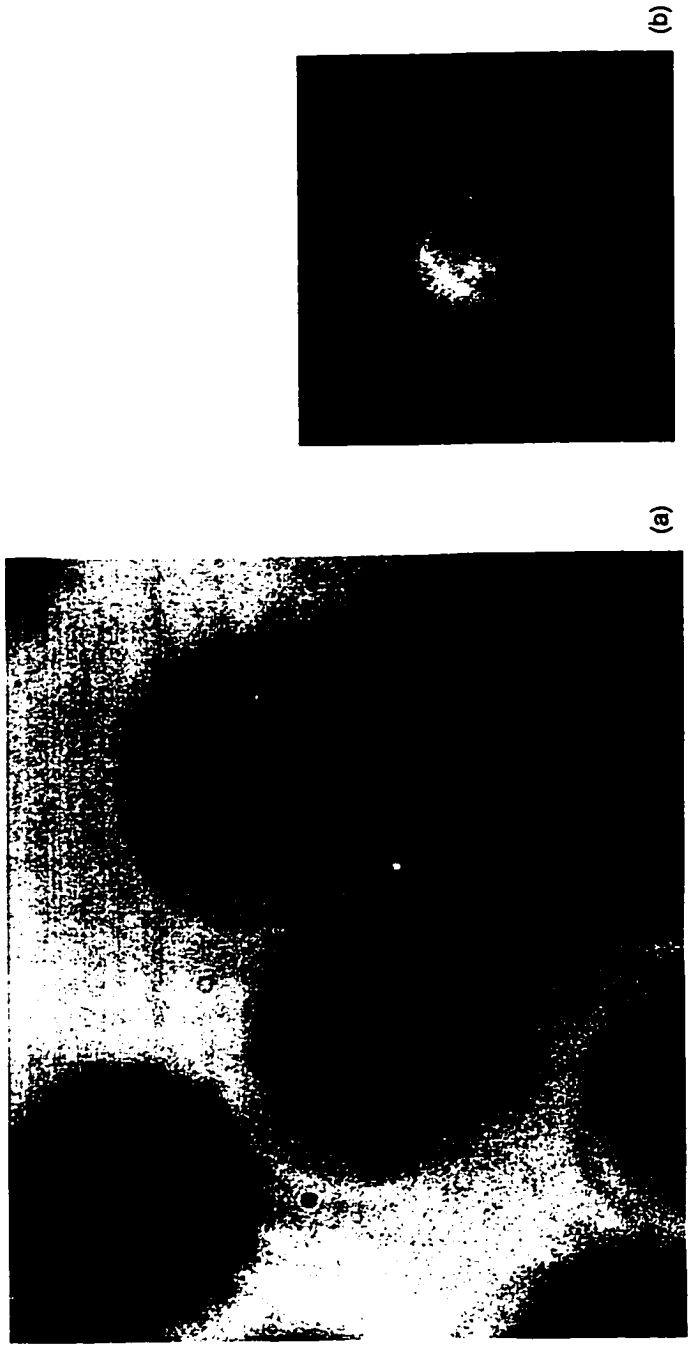

Fig. 6.2 (a), linear transmission image under white light illumination; and (b), corresponding reflected second harmonic image under 800 nm laser illumination of unstained polystyrene beads. The nominal size of beads are 11.9 μm.

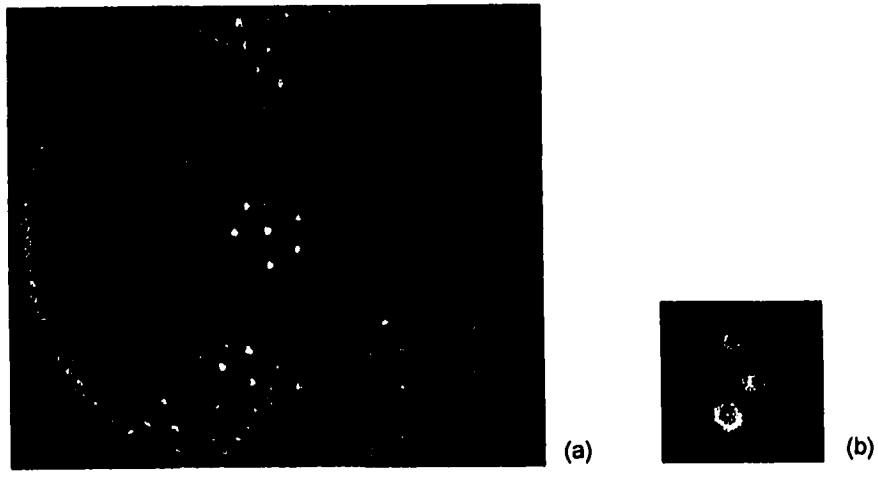

Fig. 6.3 (a), linear transmission image under white light illumination; and (b), corresponding backscattered second harmonic image under 800 nm laser illumination of unstained polystyrene beads.

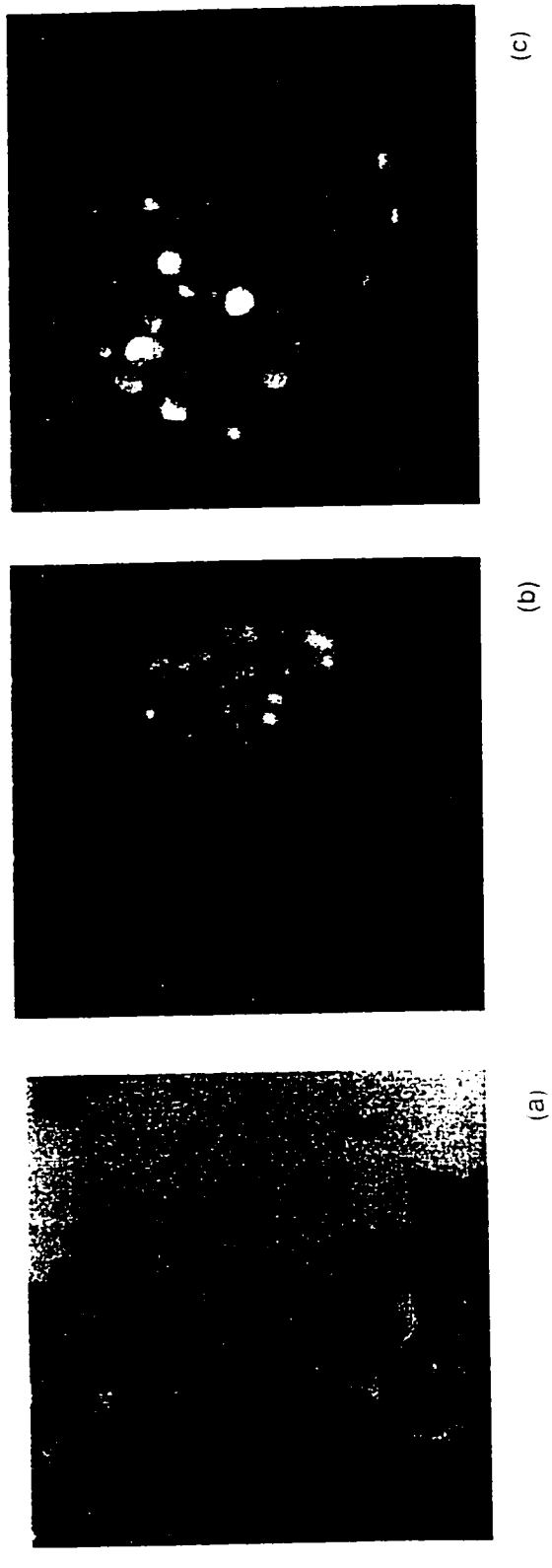

Fig. 6.4 (a), white light transmission image; (b), reflection fundamental light image; and (c), backscattered second harmonic image of polystyrene beads.

(e)

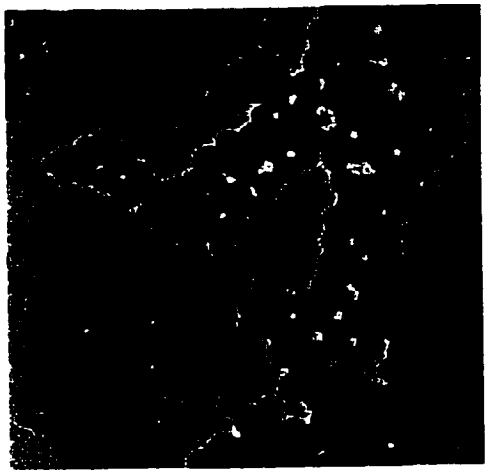

(d)

Fig. 6.4 cont. (d), white light transmission image of the polystyrene beads; and (e) the corresponding backscattered second harmonic image.

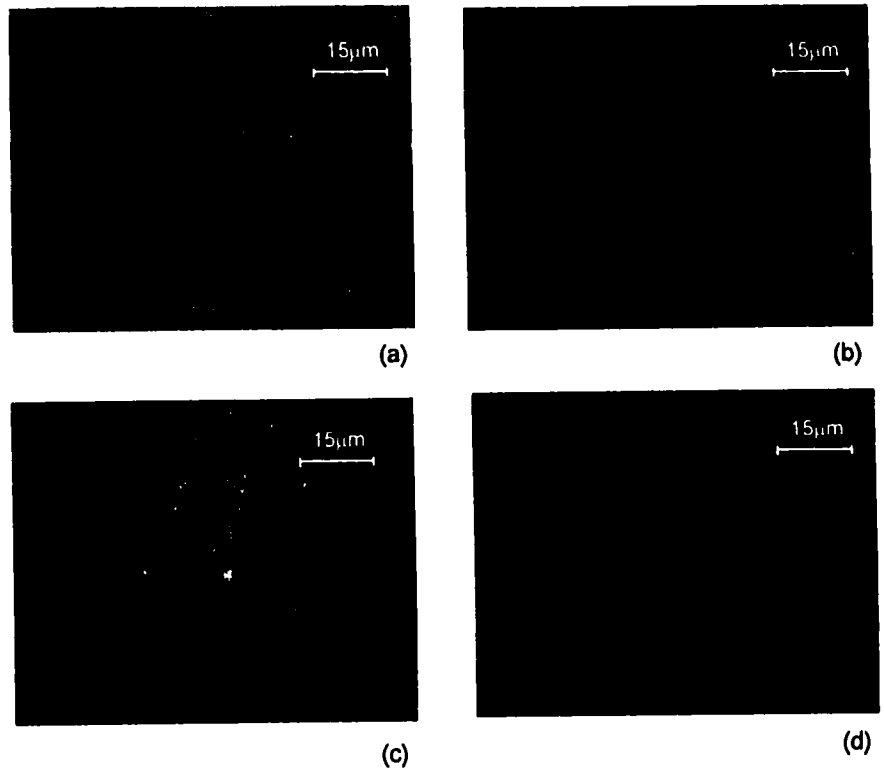

Fig. 6.5 (a) and (b), white light transmission mode images of chicken muscle tissue with different fiber orientations; (a), fiber parallel to optical slide; (b), fiber perpendicular to optical slide; (c) and (d), corresponding reflection second harmonic images to (a) and (b), respectively.

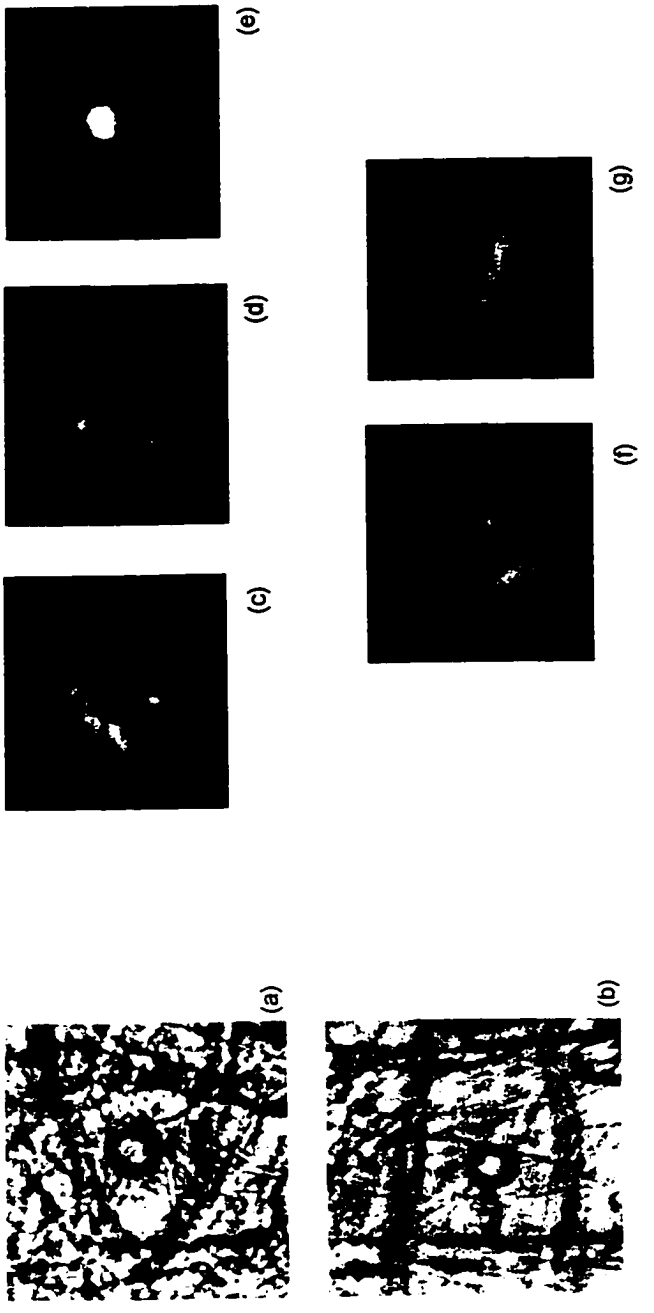

Fig. 6.6 (a) and (b), white light transmission images of two onion cells with water bubble attached at the center. (c)-(g), corresponding backscattered second harmonic images at different sample locations.

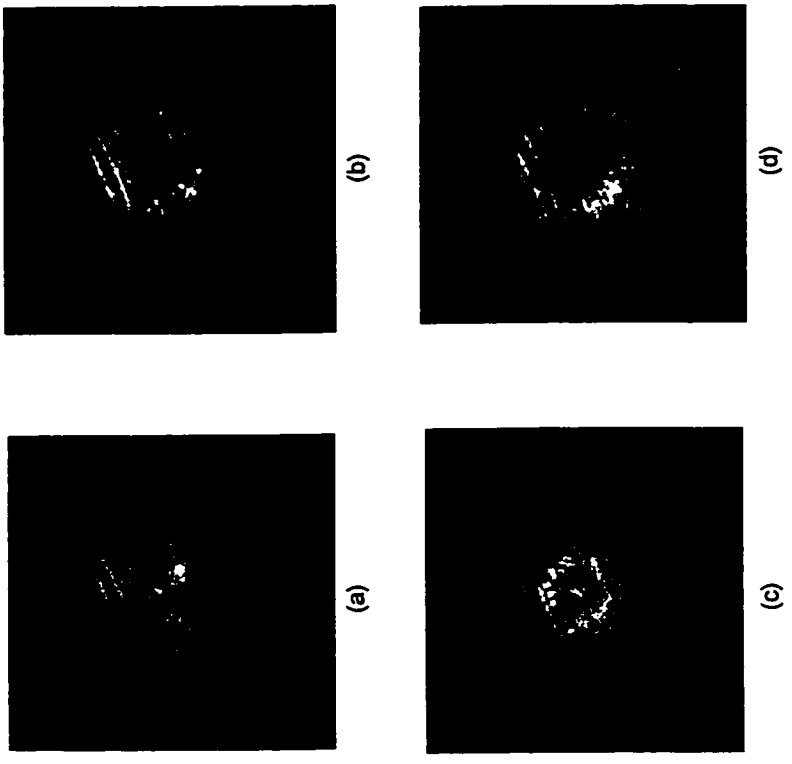

Fig. 6.7 Backscattered second harmonic images of a section of fresh onion. (a)-(d), laser spot transverses across the sample at different positions.

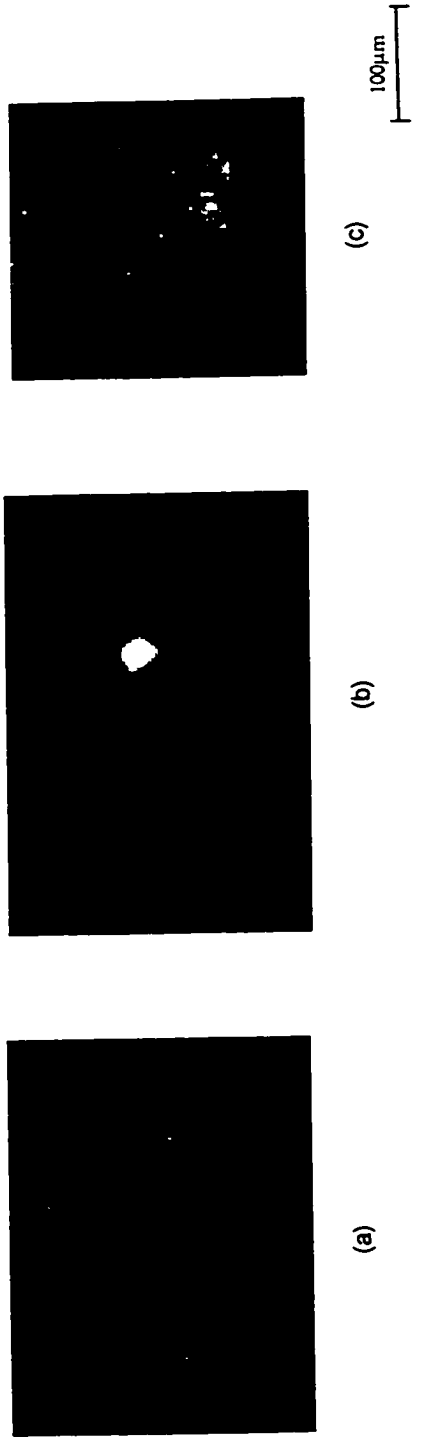

Fig. 6.8 (a), transillumination white light image of amoeba cells; (b), laser spot on the cover slide and one of the cells; (c), corresponding second harmonic image of the ameba cell.

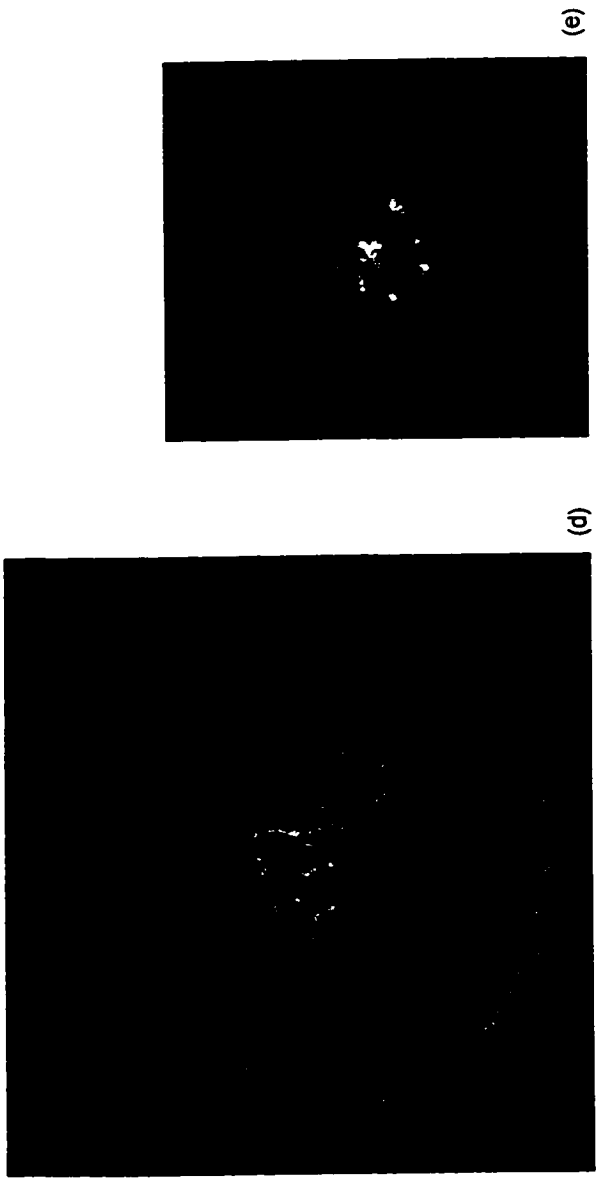

Fig. 6.8 cont. (d), white light transmission mode images of amoeba cells; (e), corresponding second harmonic image of the cell.

Fig. 6.8 cont. (f) and (g), white light transmission images of amoeba cell at different illumination angles; (h), the corresponding backscattered second harmonic image.

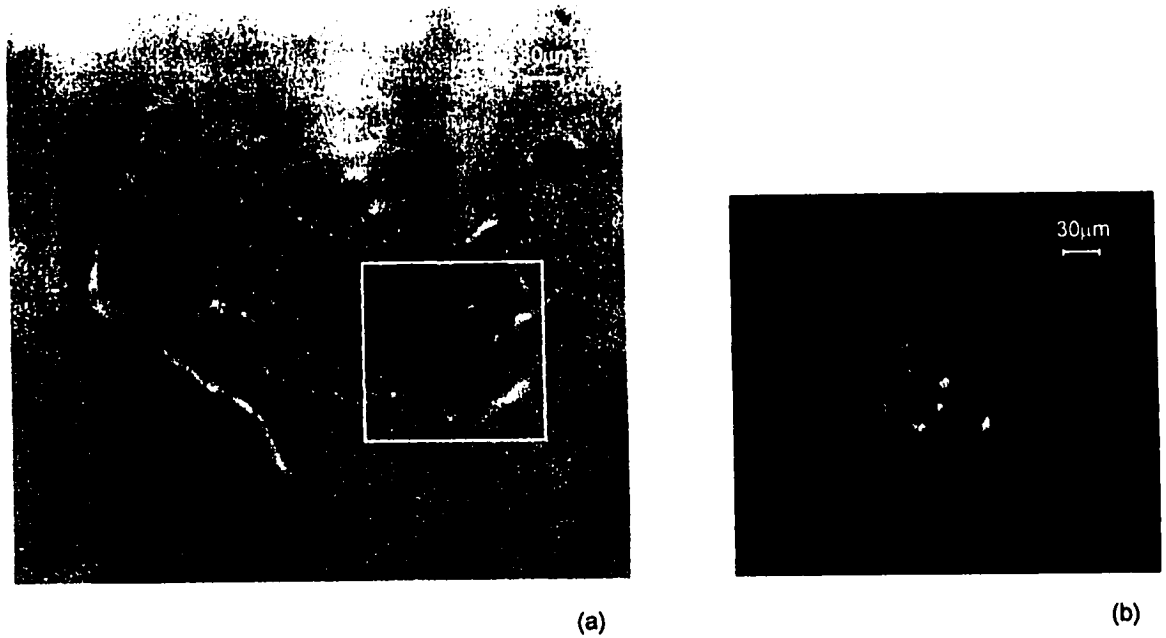

Fig. 6.9 Cellular structure of amoeba cell. (a), transmission white light image of the cell; and (b), the backscattered second harmonic image of the cellular structure indicated within the frame in (a).

References

1. Hardware Reference Manuel, Photometrics Ltd., 3440 East Britannnia Drive, Tucson, Arizona (1990).
2. E. L. Dereniak and D. Crowe, "*Optical Radiation Detectors*", John Wiley and Sons, New York (1984).
3. Yici Guo, P. P. Ho, H. Savage, D. Harris, P. Sacks, S. Shantz, F. Liu, N. Zhadin, and R. R. Alfano, Opt. Lett. **22**, 1323 (1997).
4. R. Cubeddu, A. Pifferi, P. Taroni, G. Valentin, and G. Canti, Opt. Lett. **20**, 2553 (1995).
5. Q. Z. Wang, Yici Guo, R. Zuzolo, P. P. Ho, and R. R. Alfano, to be submitted to Opt. Lett.

Chapter Seven

Two Photon Excitation of Fluorescence Imaging of Tryptophan Distributions in Animal Tissues

This chapter presents the research on two photon fluorescence imaging of tryptophan spatial distribution in animal tissues. Fluorescence from tryptophan molecules in tissue samples was excited by two-photon absorption of 625 nm, 100 fs light pulses from a colliding-pulse-mode locked dye laser. TPF imaging has demonstrated specificity with respect to intrinsic fluorophore variation *in situ* to provide subsurface map of histology and histo-chemical content of molecules.

7.1 Overview of Two Photon Excitation of Fluorescence Imaging

Two photon fluorescence microscopy in biological media was first demonstrated in 1990 by Webb's group at Cornell University.[1,2] DNA (Hoechst 33258) stained pig kidney cells were imaged under 630 nm laser excitation. A two photon imaging system uses the combined energy of two incident photons at VIS or NIR wavelength to excite transitions that are only accessible through the UV source in the conventional fluorescence microscopy. Because unwanted light scattering and photo-bleaching/toxic effects are greatly reduced, the technique offers special effectiveness for exploring functions of living cells that are sensitive to incident photo-energy. Since the first two photon bio-imaging report, multiphoton microscopy has become an subject actively studied both theoretically and experimentally.[3-7] TPF microscopy has been applied to functional imaging of free $[Ca^{2+}]_i$ activity in rat cardiac

myocyte and dentritic spines[8,9], and steady state or time resolved metabolic functional imaging of NAD(P)H in *in situ* rabbit cornea and *in vivo* human skin.[10,11] Three photon excitation of serotonin and tryptophan has been used to determine neurotransmitter concentration of individual granules in cell cultures.[12]

The basic model of a two photon microscope is shown in Fig 7.1.[13] It consists of a focusing objective lens, a scanning unit, wavelength selection components and photo-detection modules. The system uses the so called epi-illumination which refers to the surface illumination of specimen through the objective lens rather than through a separate condenser. A wavelength discriminating dichroic beam splitter diverts the laser beam into the objective lens which acts both as a condenser and a collector of signal emitted from the sample. A key element in TPF imaging is the mode-locked femtosecond laser source which supplies the necessary energy and power density to create sufficient fluorescence signal. In order to construct a 3-D image, the laser focus is scanned in three dimensions to study a sample. First, rapid 2-D scanning by moving the laser beam with two galvanometer-driven mirrors creates an image slide at a particular depth. Second, multiple 2-D scanned slides are acquired at consecutive resolvable depths to build up a 3-D image using computer software. A two photon microscope differs from a single photon confocal microscope in the way it rejects the background signal from off-focus planes. A two photon instrument can obtain a desired signal to background ratio in the focal plane while not necessarily depending on a confocal pinhole at the image plane, thus avoiding descan, i.e., tracing back the signal through the galvanometer-mirror unit. This increases signal collection efficiency and detection flexibility. By incorporating descan and a confocal pinhole, a two photon microscope can effectively enhance its performance through an increased image resolution at the expense of a lower signal collection efficiency.

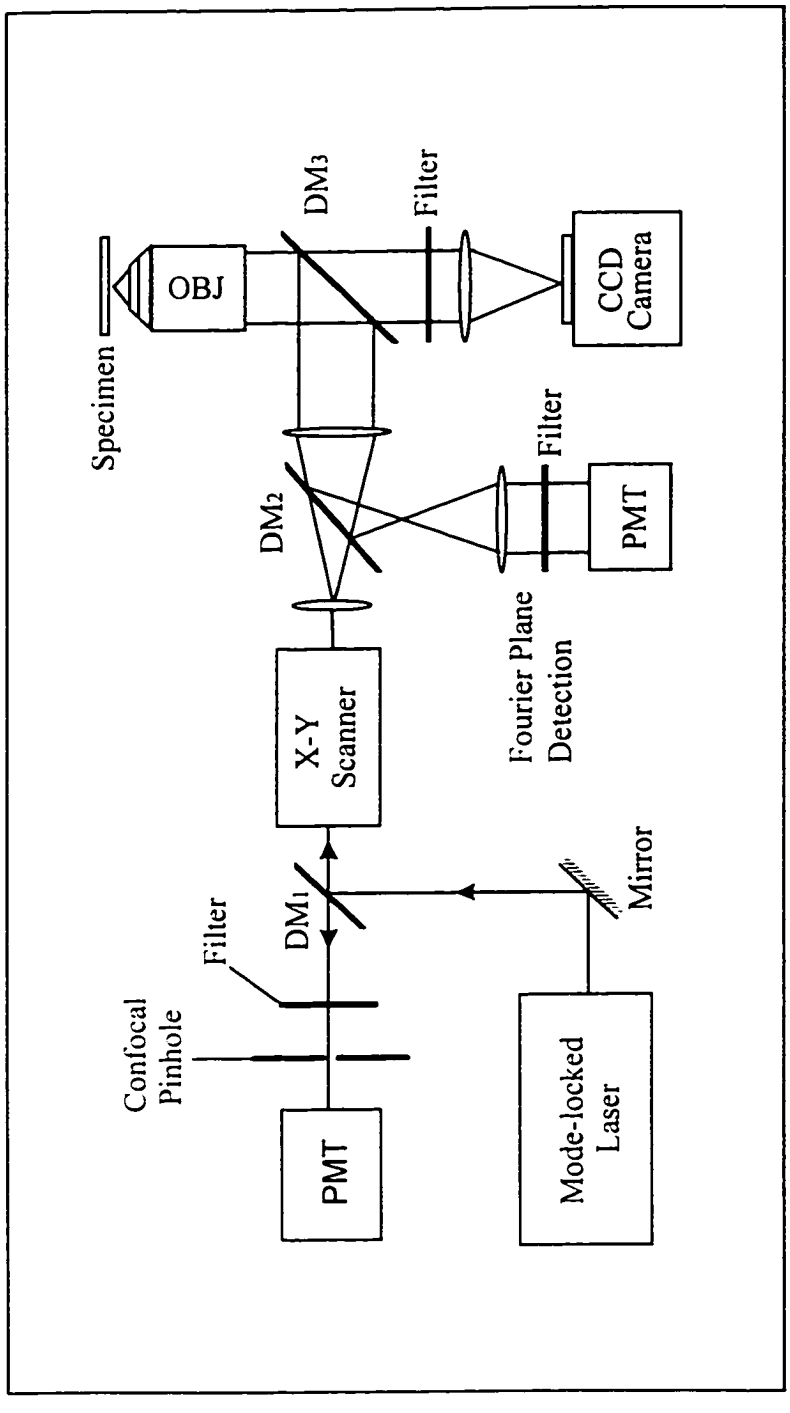

Fig. 7.1 Schematic diagram of a two photon scanning microscope. DM_i are dichroic beam splitters, OBJ is the microscope objective lens, and PMT are photomultiplier tubes.

7.2 Two-photon Fluorescence Imaging of Tryptophan

Fluorescence from intrinsic fluorophores inside biological tissues has been demonstrated as optical fingerprints of the tissue's physiological state in various applications.[15-17] Tryptophan (Trp) has been recognized as one of the key fluorescing species that accounted for up to ~90% protein fluorescence.[18-21] The emission of Trp spans the 300-400 nm spectral range and provides a consistent marker for evaluating cellular and tissue state. In particular, the emission intensity ratio of Trp to some other key fluorophores such as NADH, collagen and flavin, has been used to distinguish between normal and malignant tissues.[16,17] The fluorescence spectra and lifetime changes of Trp are found to depend on the local environment and have been used to monitor protein structural and conformational changes.[20,21] In this chapter, spatial distributions of tryptophan molecules have been measured by monitoring two photon excited fluorescence point by point from animal tissue samples.

7.3 Experimental Method and Sample

The experimental setup for TPF of Trp imaging is shown in Fig. 7.2. The setup is identical to the one that has been described in section 5.4.1; except for the signal wavelength was selected at the tryptophan fluorescence band. The muscle chicken tissue samples used for this image demonstration were excised from the frozen upper thigh portion and then thawed.[22] Two particular sample orientations were investigated. In the first orientation, the dissected tissue was positioned such that the muscle fibers were oriented along the y axis, perpendicular to the laser beam propagation direction (z axis). In the second orientation, the fibers were aligned along the z axis.

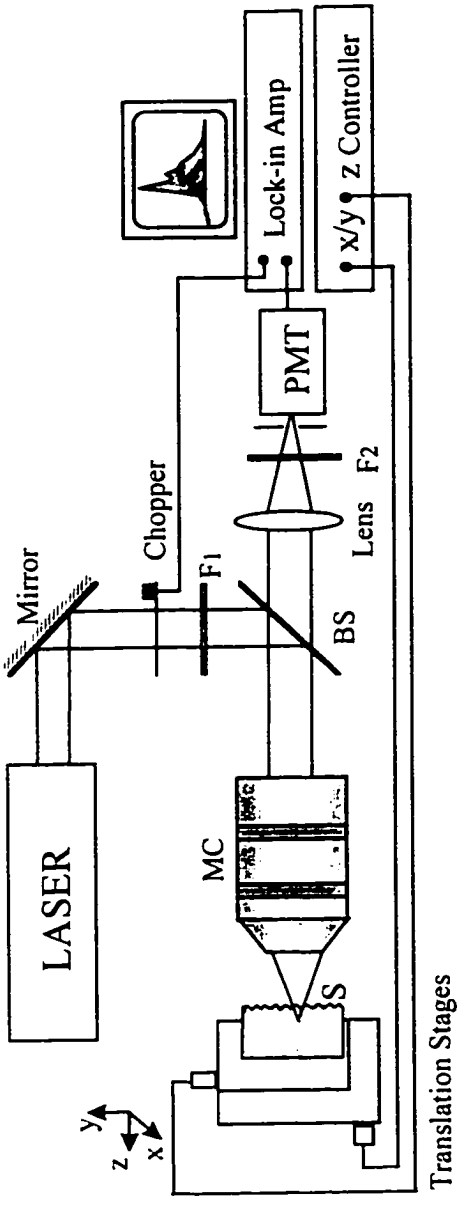

Fig. 7.2 Schematic of TPF imaging setup. MC, microscope objective; BS, dichroic beam splitter; F1 and F2 long and narrow band pass filters, respectively; PMT, photomultiplier tube.

The fluorescence over the 335-345 nm range was selected using narrow band filters (NB340). A long wavelength pass filter (LP550) was inserted in the excitation path to eliminate the possible contribution of dye fluorescence from the laser cavity. In order to verify whether the fluorescence is indeed excited by the absorption of two photons, the fluorescence signal was measured by changing the incident intensity using a set of calibrated neutral density filters. A quadratic dependence of fluorescence intensity on excitation intensity verified the TP nature of the signal. Furthermore, a reasonable level of signal strength showed that the high quantum yield of tryptophan molecules resulted in a fluorescence signal strong enough for studies even when the excitation wavelength was at the edge of the absorption band (i.e., at 312.5 nm, half of the excitation wavelength of 625 nm).[22]

7.4 Results

The raster-scanned TPF images of Trp distribution over the (x, y) plane for two different depths, and for the first orientation of the sample (muscle fibers aligned perpendicular to beam propagation direction) are shown in pseudo color in Figs. 7.3a, b. The region in red indicates a higher signal intensity corresponding to a higher Trp concentration. The longitudinal orientation of the muscle fibers is clearly resolved from these images, offering a visualization of the Trp concentration variation. The lateral scans were measured with z fixed at the peak signal location (Fig. 7.3a), and then at the next axial position of 200 μm into the sample (Fig. 7.3b). In Fig. 7.3b, some of the lateral structures were smeared out due to scattering and absorption.

To test the structure resolving capability, the muscle tissue was laterally scanned by changing the orientation of the fiber's axis along the z coordinate. In this

Fig. 7.3 Laterally scanned TPF image of Trp from chicken muscle tissue, with fiber's long axis oriented along the y axis. The z positions are: (a) at ~50 μm and (b) at next 200 μm.

arrangement, a TPF map shows the cross section of the muscle fiber at different depth. The images shown in Figs. 7.4a,b clearly present features that are different from those observed along the longitudinal fiber axis. The nearly circular patterns in Fig. 7.4a represent the cross section of individual fibers. The optical contrast defined as $C = \frac{I_{max} - I_{min}}{I_{max} + I_{min}}$ in these transversal scans was ~0.11, as compared to ~0.45 for scans along the longitudinal direction. The lower contrast level along the transversal scan suggested a relatively more homogeneous distribution of tryptophan molecules.

Figs. 7.5a,b show the laterally scanned TPF images of fat strips embedded in a muscle tissue at an axial z position of 50 μm and 150 μm, respectively. Compared with the muscle tissue region, the fat tissue regions exhibited a low TPF response of Trp, and were indicated by the purple color area in Figs. 7.5a and b. This result is consistent with the low concentration of Trp in the fat tissue.

The TPF images of the sample scanned along the axial (y, z) direction are shown in Fig. 7.6. For z direction scans, two particular types of tissue were investigated: (a) a tendon-like membrane of fascia attached to a section of muscle tissue, and (b) muscle tissue alone (the fascia layer was surgically removed). Figs. 7.6a, b show the depth images of the first and second types of tissues, respectively. The tissues were orientated such that the muscle fibers were parallel to the y axis. The measured TPF signal of tryptophan from surgically separated fascia was lower by an average factor of ~3, compared with the signal generated from muscle tissue alone. It is known that the physical thickness of the fascia generally lies in the range of ~50 to ~150 micrometers. The depth profiles of TPF from samples a and b are compared. With the presence of fascia, the observed axially scanned TPF profile in curve b of Fig. 7.7, reveals a narrower nominal spatial width at FWHM from the fasica-muscle sample, as compared with the profile observed from the muscle sample alone. This result is consistent with

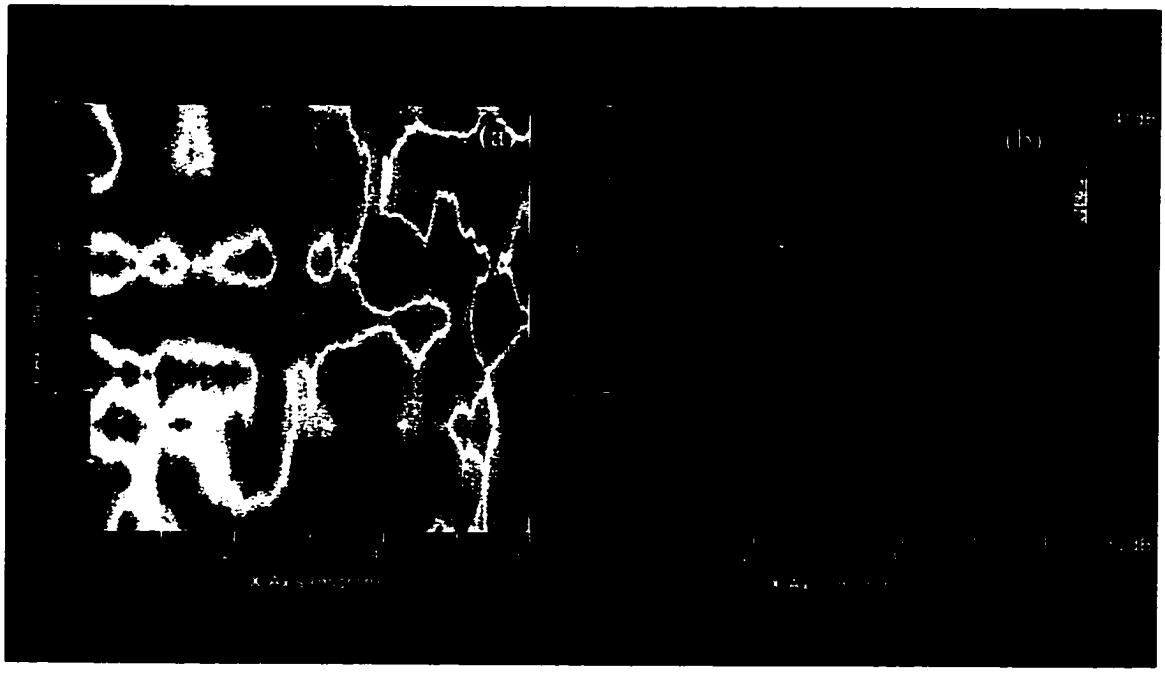

Fig. 7.4 Laterally scanned TPF image of Trp from chicken muscle tissue, with fiber's long axisoriented along the z axis. The z positions are: (a) at ~50 μm and (b) at next 200 μm.

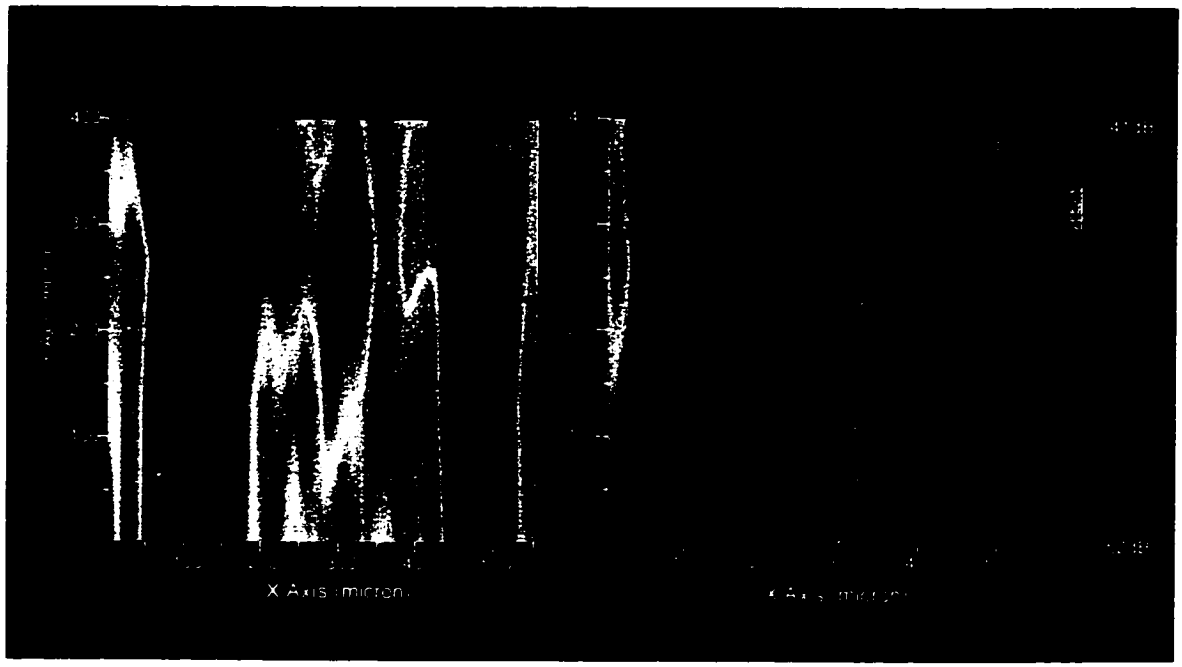

Fig. 7.5 Laterally scanned TPF image of Trp from chicken fat tissue embedded in muscle tissue, with fiber's long axis oriented along the y axis. The z positions are: (a) at ~50 μm and (b) at next 150 μm.

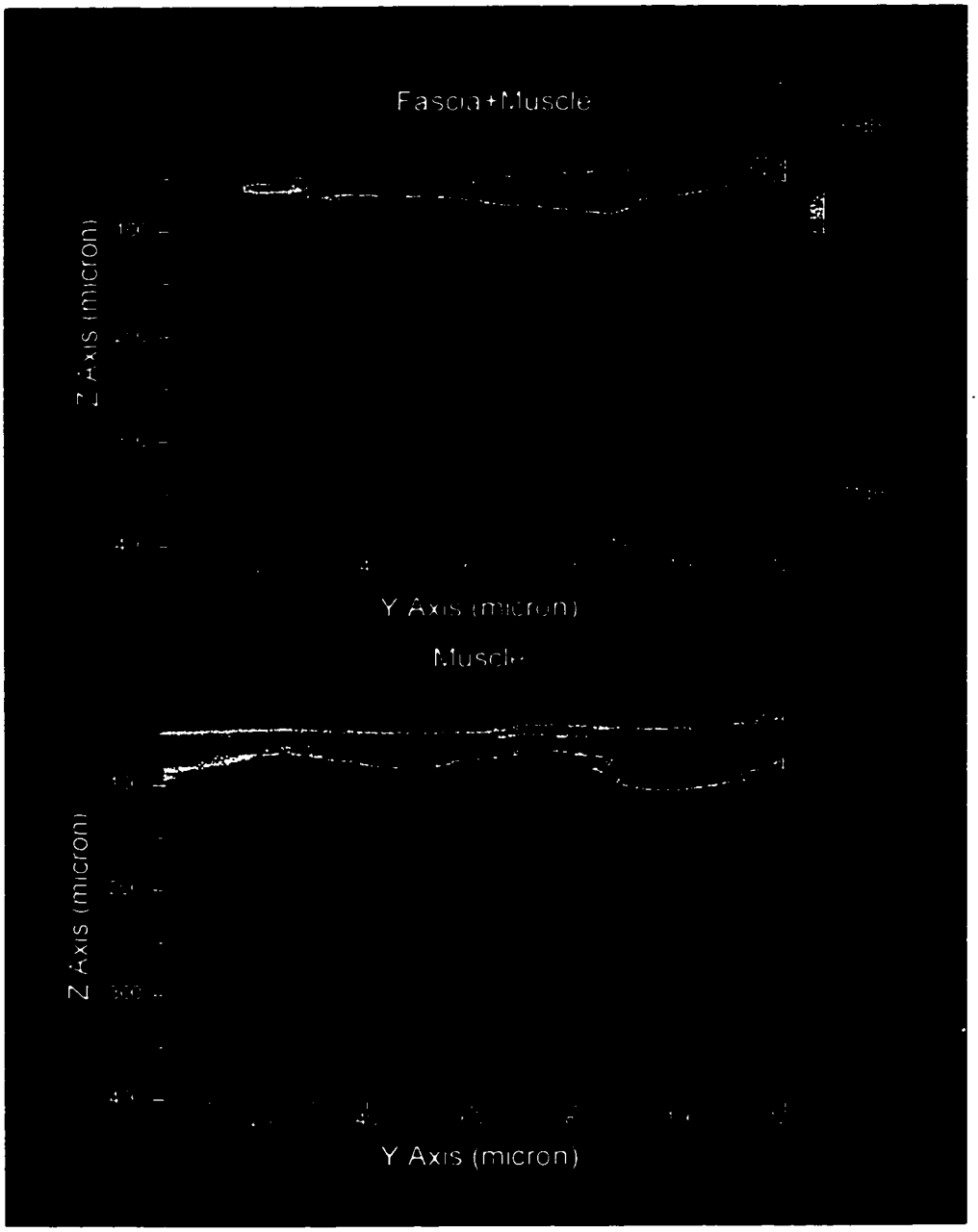

Fig 7.6 Two dimensional axially scanned TPF images of Trp from (a) fascia+muscle, and (b) muscle chicken tissues.

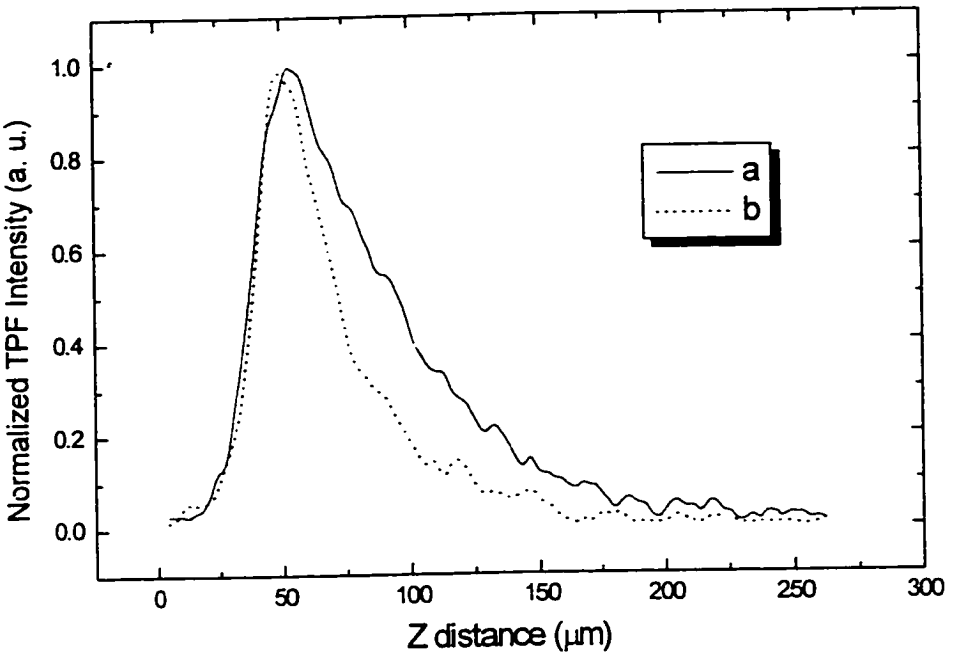

Fig. 7.7 Averaged axial profiles of z scanned TPF signals from samples of a muscle, and b facsia plus muscle.

the fact that the level of collagen, the main constituent in the fascia, is higher than that in the muscle tissue and most likely results in a low Trp concentration, leading to an observed narrower spatial depth width.

7.5 Discussion

The axial scan was not able to resolve the multiple-interface structure unambiguously. Two photon absorption cross section is related to the imaginary part of the third order nonlinear optical susceptibility $\mathrm{Im}\chi^{(3)}$. TPF emission after TPA is an incoherent process and is not interface-sensitive as much as second harmonic generation.

Using Tryptophan as a readily-detectable native fluorescence probe, two dimensional two-photon laser scanning images have been obtained to produce tomographic images revealing structures associated with Trp concentration variations inside tissues. The technique utilizes the nonlinear dependence of TPF signal on the excitation intensity to achieve noninvasive histo-chemical map of tissues. Besides Trp, other key native fluorophores, such as collagen, elastin, NADH and flavins are well suited for TPF imaging with selected excitation wavelengths. A direct application of two-photon excitation technique to medicine is to detect subsurface abnormalities via changes in Trp, collagen, elastin, NADH, flavin and other molecules from morphological alterations. Table 7.1 lists the fluorescence band of key fluorophores in tissue and the suitable laser wavelength for TPF excitation. By selectively exciting different native fluorescent molecular groups, the TPF imaging technique can be especially effective for mapping the spatial distribution of molecules or evaluating *in situ* chemical composition changes.

Table 7.1 Fluorescence band and excitation wavelength of TPF for key fluorophores in tissues.

Molecules	TPF Band	Excitation λ	Laser System
Tryptophan	340 nm	560 - 630 nm	Dye, Forsterite (SHG)
Collagen	380 nm	680 - 700 nm	Dye, Ti:Sapphire, Cr:YAG (SHG)
Elastin	410 nm	700 - 740 nm	Dye, Ti:Sapphire, Cr:YAG (SHG), CUNYITE (SHG)
NADH	460 nm	700 - 730 nm	Dye, Ti:Sapphire, Cr:YAG (SHG), CUNYITE (SHG)
Flavin	525 nm	900 - 940 nm	Dye, Ti:Sapphire
Porphyrins	630 - 800 nm	1200 -1400 nm	CUNYITE, Forsterite

Reference

1. W. Denk, J. H. Strickler, and W. W. Webb, Science **248**, 73 (1990).
2. W. Denk, Soc. Neurosci. Abstr. **19**, 91 (1993).
3. M. Gu and C. J. R. Sheppard, J. of Microsc. **177**, 128 (1994).
4. I. Gryczynski, H. Malak, and J. R. Lakowicz, Biospectroscopy **2**, 9 (1996).
5. H. Szmacinski, I. Gryczynski, and J. R. Lakowicz, Biophys, J. **70**, 547 (1996).
6. D. L. Wokosin, V. E. Centonze, J. G. White, S. N. Hird, S. Sepesenwol, G. P. S. Malcolm, G. T. Maker, and A. I. Ferguson, Proc. SPIE **2678**, 38 (1996).
7. C. Xu and W. W. Webb, J. Opt. Soc. Am. B **13**, 481 (1996).
8. D. W. Piston, M. S. Kirby, H. Chen, W. J. Lederer, and W. W. Webb, Appl. Opt. **33**, 662 (1994).
9. R. Yuste and W. Denk, Nature **375**, 682 (1995).
10. D. W. Piston, B. R. Masters, and W. W. Webb, J. of Microsc. **178**, 20 (1995).
11. B. R. Masters, P. T. C. So, and E. Gratton, Biophys. J. **72**, 2405 (1997).
12. S. Maiti, J. B. Shear, R. M. William, W. R. Zipfel, and Watt W. Webb Science **275**, 24 (1997).
13. J. Manni, Biophotonics International, Jan./Feb. Issue, 66 (1996).
14. P. T. So, T. French, W. M. Yu, K. M. Berland, C. Y. Dong, and E. Gratton, "*Fluorescence Imaging Spectroscopy and Microscopy*", Vol. 137, John Wiley & Sons, New York (1996).
15. R. R. Alfano, D. B. Tata, J. Cordero, P. Tomashefsky, F. W. Longo, and M. A. Alfano, IEEE J. Quant. Electron. QE-20, 1507 (1984).
16. R. R. Alfano, G. C. Tang, A. Pradhan, W. Lam, D. C. Choy, and E. Opher, IEEE J. Quant. Electron. QE-23, 1806 (1987).

17. R. R. Alfano, B. B. Das, J. B. Cleary, R. Prudente, and E. Celmer, Bull. New York Acad. Med., 2nd Series **67**, 143 (1991).

18. J. R. Lakowicz and I. Gryczynski, Biophys. Chem. **45**, 1 (1992).

19. J. R. Lackowicz, I. Gryczynski, E. Danielsen, and J. Frisoli, Chem. Phys. Lett. **194**, 282 (1992).

20. J. A. B. Ross, H. R. Wyssbrod, R. A. Porter, G. P. Schwartz, C. A. Michaels, and W. R. Laws, Biochem. **31**, 1585 (1992).

21. Ji Ji Cheng, *"Photo-biology Physics"*, Chinese Academic Publisher, Beijing (1987).

22. Yici Guo, Q. Z. Wang, N. Zhadin, Feng Liu, S. G. Demos, D. Calistru, A. Tirksliunas, A. Katz, Y. Budansky, P. P. Ho, and R. R. Alfano, Appl. Opt. **36**, 968 (1997).

Chapter Eight

Future Directions

The future work in NLO spectroscopy and microscopy can be divided into two main areas: (a) clinical applications using second or third harmonic generation and two or three photon fluorescence techniques to achieve noninvasive histological and histochemical evaluations; and (b) non-medical applications.

8.1 Clinical Testing of NLO Spectroscopy and Microscopy

In clinical testing, *in vivo* animal and human tissues will be investigated using NLO spectroscopy and microscopy. A prototype of a fiber probe based two photon spectroscopy instrument is shown in Fig. 8.1. The testing probe can be integrated into endoscopes to provide spectral pathology based on biochemical changes in aerodigestive, gastrointestinal and gynecological tracts. The excitation laser light is delivered through an optical fiber which also collects the returned TPF light. A spectrometer coupled with photomultiplier tube or spectrograph/CCD system is used to perform the on site spectral analysis. In order to photo-excite several key fluorescent chromophores, illumination from wavelength tunable laser or different lasers needs to be coupled into the optical fiber. The recently developed Ti:Sapphire, Forsterite and CUNYITE lasers can be used in conjunction with frequency doubling crystals and optical parametric oscillator to provide femtosecond and high peak energy pulses covering wide spectral ranges. In signal detection, sensitive photodetectors are required

in order to compensate for the low signal level due to fiber coupling and focusing/collection geometry.

For *in vivo* laser applications, one of the requirements is to adjust the incident laser power to a value below the safety standard. Figure 8.2 demonstrates a setup for direct NLO imaging using a time gated CCD camera. An electronic time gate is used to select pulses in a time window of excitation. The purpose of this time gate is to reduce the total amount of the laser energy irradiated on the sample and to increase the signal to noise ratio. In the detection module, synchronized time gate and a wavelength selector are used to pass the signal within a selected spectral region. The CCD camera will acquire direct lateral images of the sample within the time sliced interval. As the sample is moved along the lateral and axial directions, images at different tissue locations in the surface region can be obtained.

8.2 NLO Microscopy of Structures and Defects in Semiconductor and at Interfaces

Second harmonic and two photon imaging can be used to explore surfaces and microstructures in semiconductors, dielectric and other materials. Potential applications include 3-D failure analysis in integrated circuit (IC), interconnections, defect detection in structures. The NLO technique will provide the advantages in a deeper penetration depth and high spatial resolution. Information on defects inside the material is important to device application. Fig. 8.3 shows the experimental setup of two photon induced current and two photon induced fluorescence imaging in programmable random access memory (PRAM) chips, multilayered lasing medium and

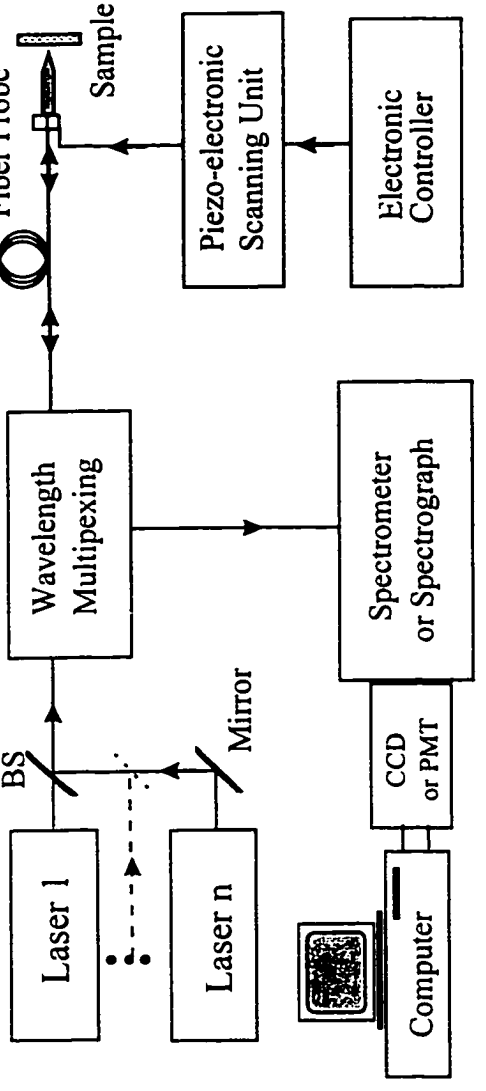

Fig. 8.1 Optical fiber based TPF spectroscopy measurement setup.

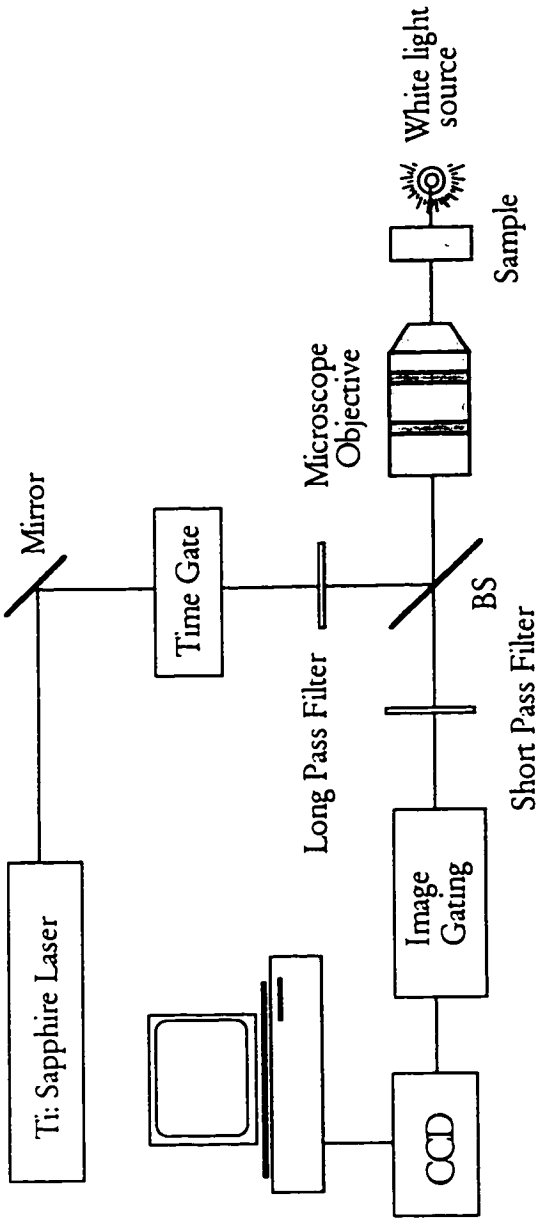

Fig. 8.2 Experimental setup for direct reflection nonlinear optical imaging using a CCD camera. An electronic gate synchronized with the CCD camera is used to select a time window to image the sample.

miniature optoelectronic devices. The wavelength of the excitation laser is adjusted to below the band gap energy of a particular material, thus signal generated from subsurface region can be obtained due to the deep penetration in a two photon excitation. In imaging of IC chips, the excitation wavelength is set to below the band gap energy of silicon substrate (<1.12 eV, $\lambda=1.25$ μm). The illumination will effectively transverse through the substrate up to several hundred microns below the back surface then focused onto the circuit. At the focal region, optically induced carrier pairs will contribute to a current which is conducted through the bond wire output. This two photon induced current (TPIC) will be amplified and detected to map a section in the IC chip for analysis. By changing the IC's external supply and bias voltage or current, optically induced switching in the circuit can be observed. The structure changes associated with defects are transformed into resistance or current changes and pinpointed by the laser beam that is scanned across the circuit.

When two or three photon fluorescence or second harmonic generation is used to image a sample, the excited fluorescence or harmonic signal will be collected by the microscope objective and detected by a photo-detector unit. The structure deformation and damage will be reflected by fluorescence signal intensity changes or second harmonic intensity changes resulted from dislocation of structure element or symmetry breakdown.

Fig. 8.4 shows the cross sectional diagram of silicon carbide. Using laser light below the band gap energy, TPF imaging can detect defects inside the medium down to sub millimeters. The achievable resolution in the lateral direction is on the order of 1 μm by using a high numerical aperture microscope objective lens ($NA \geq 1$) and a confocal pinhole. The axial resolution is on the order of 10 μm.

Fig. 8.5 displays a cross sectional diagram of a InGaN multiple quantum well laser diode which emits in the green and blue region. By applying laser scanning microscopy, two photon fluorescence signal can provide emission characteristics in different layers inside the laser diode. As the laser focus scanned through multiple layers of structures, different fluorescence spectra can be identified and used to image and explore substructures inside a particular layer. Interfaces between layers can be probed using second harmonic generation technique.

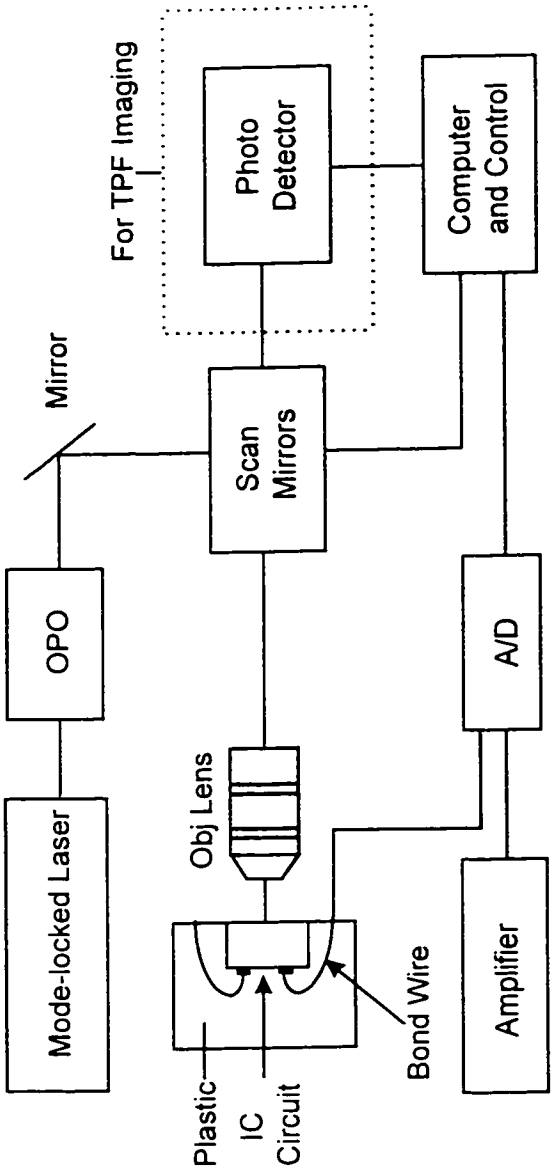

Fig. 8.3 Schematic diagram of two photon induced current and two photon excitation of fluorescence imaging for failure analysis in the integrated circuit. OPO: optical parametric amplifier, Obj: microscope objective, A/D analog to digital converter.

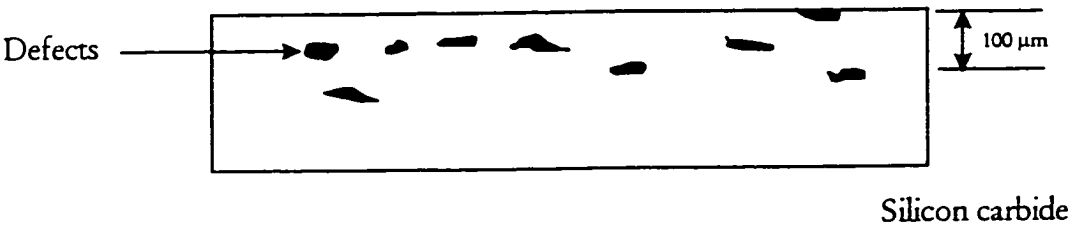

Fig. 8.4 Cross sectional diagram of silicon carbide with defects at various locations.

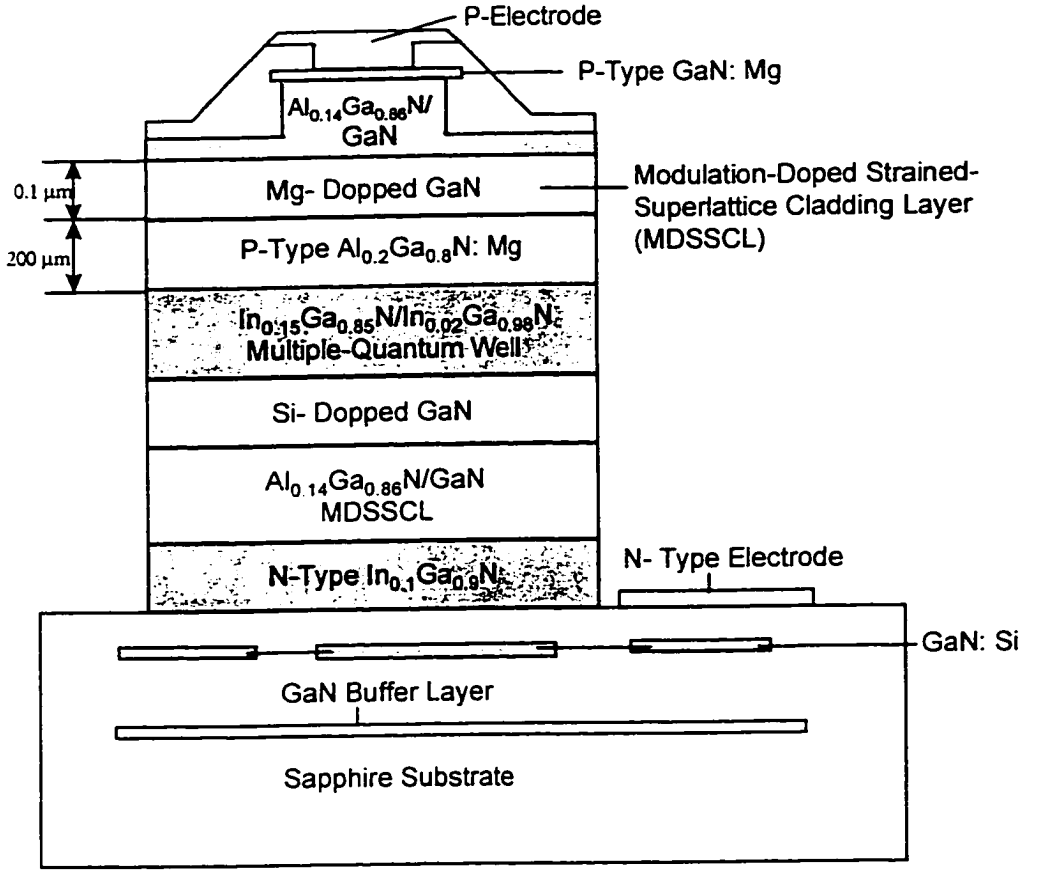

Fig. 8.5 Cross sectional diagram of InGaN multiple-quantum-well laser diode.

References

1. C. Xu and W. Denk, Appl. Phys. Lett. 71, 2578 (1997).
2. H. Komoda and K. Shimizu, Jpn. J. Appl. Phys. 33, 3393 (1994).
3. B. P. Richards and P. K. Footner, "*The role of Microscopy in Semiconductor Failure Analysis*", Oxford University Press, New York (1992).
4. S. Nakamura, Photonics Spectra, May Issue, 130 (1998).
5. S. Nakamura and G. Fasol, "*The Blue Laser Diode*", Springer-Verlag, New York (1997).

Bibliography

Chapter 1

1. P. A. Franken, A. E. Hill, C. W. Peters, and G. Weinreich, Phys. Rev. Lett. 7, 118 (1961).
2. N. Bloembergen, J. Ducuining, and P. S. Pershan, Phys. Rev. 127, 1918 (1962).
3. J. A. Giordmaine, Scientific American 210, 38 (1964).
4. Y. R. Shen, "*Principles of Nonlinear Optics*", John Wiley and Sons (1984), and the references therein.
5. M. D. Levenson and N. Bloembergen, J. Chem. Phys. 60, 1323 (1974).
6. J. L. Oudar and Y. R. Shen, Phys. Rev. A 22, 1141 (1980).
7. R. Hellwarth and P. Christiansen, Opt. Comm. 12, 318 (1974).
8. P. D. Maker and R. W. Terhune, Phys. Rev. B 6, 534 (1972).
9. J. Haung and A. Lewis, Biophys. J. 55, 835 (1989).
10. J. Huang, Z. Chen, and A. Lewis, J. Phys. Chem. 93, 3314 (1989).
11. S. Fine and W. P. Hansen, Appl. Opt. 10, 2350 (1971).
12. J. Gannaway and C. J. R. Sheppard, Opt. & Quant. Elect. 10, 435 (1978).
13. S. Roth and I. Freund, Biopolymers, 20, 1271 (1981).
14. I. Freund, M. Deutsch, and A. Sprecher, Biophys. J. 50, 693 (1986).
15. O. Bouevitch, A. Lewis, I. Pinevsky, J. P. Wuskell, and L. M. Loew, Biophys. J. 65, 672 (1993).
16. W. Denk, J. H. Strickler, and W. W. Webb, Science 248, 73 (1990).
17. P. E. Hanninen, E. Soini, and S. W. Hell, J. Microsc. 176, 222 (1994).

18. W. Denk, D. W. Piston, and W. W. Webb, "*Handbook of Biological Confocal Microscopy*", Plenum Press, New York (1995).

19. D. W. Piston, B. R. Masters, and W. W. Webb, J. of Microsrc. **178**, 20 (1995).

20. B. A. Rockwell, W. P. Roach, M. E. Rogers, M. W, Mayo, and C. A. Toth, Opt. Lett. **18**, 1792 (1993).

21. B. R. Masters, P. T. C. So, and E. Gratton, Biophys. J. **72**, 2405 (1997).

22. S. Maiti, J. B. Shear, R. M. Williams, W. R. Zipfel, and W. W. Webb, Science **275**, 530 (1997).

23. S. K. Kurtz and T. T. Perry, J. Appl. Phys. **39**, 3298 (1968).

24. V. E. Kravtsov, V. M. Agranovich, and K. I. Grigorishin, Phy. Rev. B, **44**, 4931 (1991).

25. K. M. Yoo, S. Lee, Y. Takiguchi, and R. R. Alfano, Opt. Lett. **14**, 800 (1989).

Chapter 2

1. A. E. Franken, C. Hill, W. Peters, and G. Weinreich, Phys. Rev. Lett. **7**, 118 (1961).

2. Yi Ji Guo, "*Nonlinear Optics*", Publisher of Northwestern Electronic Communication Engineering, China (1987).

3. N. Bloembergen, "*Nonlinear Optics*", Benjamin, New York (1965).

4. G. C. Baldwin, "*An Introduction to Nonlinear Optics*", Plenum Press, New York (1969).

5. Y. R. Shen, "*Principles of Nonlinear Optics*", John Wiley and Sons (1984), and the references therein.

6. D. C. Hanna, M. A. Yuratich, and D. C. Cotter, "*Nonlinear Optics of Free Atoms and Molecules*", Heidelberg, New York (1979).

7. S. K. Kurtz and T. T. Perry, J. Appl. Phys. **39**, 3798 (1968).

8. V. E. Kravtsov, V. M. Agranovich, and K. I. Grigorishin, Phy. Rev. B, **44**, 4931 (1991).

9. W. Denk, J. H. Strickler, and W. W. Webb, Science **248**, 73 (1990).

10. P. E. Hanninen, E. Soini, and S. W. Hell, J. Microsc. **176**, 222 (1994).

11. D. W. Piston, B. R. Masters, and W. W. Webb, J. of Microsc. **178**, 20 (1995).

12. Feng Liu, Ph. D Thesis, City College of New York (1993).

13. A. Ishimaru, "*Wave Propagation and Scattering Random Media*", Academic Press, New York (1978).

13. M. Lax, V. Nayaramamurti, and R. C. Fulton, "*Laser Optics of Condense Matters*", Plenum Press, New York (1987).

Chapter 3

1. J. M. Barrett, P. Abramoff, A. K. Kumaran, and W. F. Millington, "*Biology*", Prentice-Hall, Englewood Cliffs, N. J. (1985).

2. T. Ebe and S. Kobayashi, "*Fine Structure of Human Cells and Tissues*", John Wiley & Sons, New York, Igaku Shoin Ltd. Tokyo (1972).

3. I. Freund, M. Deutsch, and A. Sprecher, Biophys. J. **50**, 693 (1986).

4. Y. R. Shen, "*Principles of Nonlinear Optics*", John Wiley and Sons (1984), and the references therein.

5. J. J. Wynne and Bloembergen, Phys. Rev. **188**, 1211 (1969).

6. R. C. Miller and W. A. Nordland, Phys. Rev. **B2**, 4896 (1970).

7. S. K. Kurtz and T. T. Perry, J. Appl. Phys. **39**, 3298 (1968).

8. S. Fine and W. P. Hansen, Appl. Opt. **10**, 2350 (1971).

9. Y. Guo, P. P. Ho, A. Tirksliunas, F. Liu and R. R. Alfano, Appl. Opt. **35**, 6810 (1996).

10. O. Bouevitch, A. Lewis, I. Pinevsky, J. P. Wuskell, and L. M. Loew, Biophys. J. **65**, 672 (1993).

11. W. Denk, D. W. Piston, and W. W. Webb, "*Handbook of Biological Confocal Microscopy*", Plenum Press, New York (1995).

12. S. G. Schulman, "*Fluorescence and Phosphorescence Spectroscopy: Physiochemical Principles and Practice*", Pergamon Press, New York (1977).

13. R. F. Steiner and I. Weinryb, "*Excited State of Proteins and Nucleic Acids*", Plenum Press, New York (1971).

14. Dana Calistru, Phys. Dept. of CCNY, personal communication.

15. S. Bhagavantam, "*Scattering of Light and the Raman Effect*", Chemical Publishing Co., New York (1942).

16. K. M. Yoo, S. Lee, Y. Takiguchi, and R. R. Alfano, Opt. Lett. **14**, 800 (1989).

17. V. E. Kravtsov, V. M. Agranovich, and K. I. Grigorishin, Phy. Rev. B **44**, 4931 (1991).

Chapter 4

1. M. Göppert-Mayer, Ann. Phys. **9**, 273 (1931).

2. W. Kaiser and C. G. B. Garrett, Phys. Rev. Lett. 7, 229 (1961).

3. J. P. Hermmann and J. Ducuing, Phys. Rev. A 5, 2557 (1972).

4. H. Mahr, "*Two-photon Absorption Spectroscopy*", Chapter 4 in "*Quantum Electronics: A Treatise, Nonlinear optics, Part A*", Vol. 1, Academic Press, New York (1975).

5. Y. R. Shen, "*Principles of Nonlinear Optics*", Chapter 12, John Wiley and Sons, New York (1984).

6. H. Eyring, C. J. Christensen, and H. S. Johnston, "*Annual Review of Physical Chemistry*", Annual Reviews Inc. (1967).

7. W. L. Peticolas and K. E. Rieckhoff, J. Chem. Phys. 39, 1347 (1963).

8. D. J. Bradley, M. H. R. Hutchinson, and H. Koetser, Proc. R. Soc. London Ser. A 329, 105 (1972).

9. C. Xu and W. W. Webb, J. Opt. Soc. Am. B 3, 481 (1996).

10. C. Xu, W. Zipfel, J. B. Shear, R. M. Williams, and W. W. Webb, Proc. Natl. Acad. Sci. 93, 10763 (1996).

11. M. D. Galanin, B. P. Kirsanov, and Z. A. Chizhikova, Sov. Phys. JETP Lett. 9, 304 (1969).

12. A. Fischer, C. Cremer, and E. H. K. Stelzer, Appl. Opt. 34, 1989 (1995).

13. W. Denk, J. Biomed. Opt. 1(3), 296 (1996), and the references therein.

14. R. R. Alfano, D. B. Tata, J. Cordero, P. Tomashefsky, F. W. Longo, and M. A. Alfano, IEEE J. Quant. Electron. QE-20, 1507 (1984).

15. R. Richards-Kortum, R. P. Rava, R. E. Petras, M. Fitzmaurice, M. Sivak, and M. S. Feld, Photochem. Photobiol. 50, 777 (1991).

16. Y. Yang, L. D. Mitchell, and R. R. Alfano, J. Biomed. Opt. 2, 53 (1997).

17. Ji Ji Cheng, "*Photo-biology Physics*", Chinese Academic Publisher, Beijing, (1987).

18. R. R. Alfano, G. C. Tang, A. Pradhan, W. Lam, D. C. Choy, and E. Opher, IEEE J. Quant. Electron. QE-23, 1806 (1987).
19. Yici Guo, Q. Z. Wang, N. Zhadin, Feng Liu, S. G. Demos, D. Calistru, A. Tirksliunas, A. Katz, Y. Budansky, P. P. Ho, and R. R. Alfano, Appl. Opt. 36, 968 (1997).
20. S. A. Ahmed, Z. W. Zhang, K. M. Yoo, and R. R. Alfano Appl. Opt. 33, 2746 (1994).
21. M. S. Patterson and B. W. Pogue, Appl. Opt. 33, 1963 (1994).
22. A. E. Cerussi, J. S. Maier, S. Fantini, M. A. Franceschini, W. W. Mantulin, and E. Gratton, Appl. Opt. 36, 116 (1997).
23. N. N. Zhadin and R. R. Alfano, J. Biomed. Opt. 3(2), 171 (1998), and the references therein.

Chapter 5

1. C. J. R. Sheppard, J N. Gannaway, R. Kompfner, and D. Walsh, IEEE Trans. QD-13, 100D (1977).
2. I. Freund, M. Deutsch, and A. Sprecher. Biophys. J. 50, 693 (1986).
3. Min Gu and C. J. R. Sheppard, J. of Microsc. 177, 128 (1994).
4. J. Manni, Biophotonics International, Jan./Feb. Issue, 66 (1996).
5. D. R. Sandison and W. W. Webb, Appl. Opt. 33, 603 (1994).
6. Min Gu and C. J. R. Sheppard, J. Opt. Am. A. 9, 151 (1992).
7. P. T. C. So, T. French, W. M. Yu, K. M. Berland, C. Y. Dong, and E. Gratton, "*Fluorescence Imaging Spectroscopy and Microscopy*", Chapter 11, John Wiley & Sons, New York (1996).

8. Yici Guo, P. P. Ho, H. E. Savage, D. Harris, P. Sacks, S. Schantz, F. Liu, N. Zhadin, and R. R. Alfano, Opt. Lett. **22**, 1323 (1997).

9. Y. R. Shen, "*Principles of Nonlinear Optics*", Chapter 12, John Wiley and Sons, New York (1984).

10. R. A. Weinberg, Scientific American Sept., 62 (1996).

11. R. R. Alfano, D. B. Tata, J. Cordero, P. Tomashefsky, F. W. Longo, and M. Alfano, IEEE J. Quant. Electron. QE-**20**, 1507 (1984).

12. R. R. Alfano, G. C. Tang, A. Pradhan, W. Lam, D. C. Choy, and E. Opher, IEEE J. Quant. Electron. QE-**23**, 1806 (1987).

13. R. R. Alfano, A. Pradham, and G. C. Tang, J. of Opt. Soc. Am. B. **6**, 1015 (1989).

14. R. Richards-Kortum, R. P. Rava, R. E. Petras, M. Fitzmaurice, M. Sivak, and M. S. Feld, Photochem. Photobiol. **50**, 777 (1991).

15. J. Hung, S. Lam, J. C. Le Riche, and B. Palcic, Laser Surg. Med. **11**, 99 (1991).

16. Yuanlong Yang, G. C. Tang, M. Bessler, and R. R. Alfano, Laser in the Life Sci. 6(4), 259 (1995).

17. W. Denk, J. H. Strickler, and W. W. Webb, Science **248**, 73 (1990).

18. D. Huang, E. A. Swanson, C. P. Lin, J. S. Schuman, W. G. Stinson, W. Chang, M R. Hee, T. Flotte, K. Gregory, C. A. Puliafito, and J. G. Fujimoto, Science, **254**, 1178 (1991).

19. E. A. Swanson, J. A. Izatt, M. R. Hee, D. Huang, C. P. Lin, J. S. Schuman, D. A. Puliafito, and J. G. Fujimoto, Opt. Lett. **18**, 1864 (1993).

20. P. G. Sacks, H. E. Savage, J. Levine, V. R. Kolli, R. R. Alfano, and S. P. Schantz, Cancer Letts. **104**, 171 (1996).

21. M. L. Steinberg and V. Defendi, Proc. Natl. Acad. Sci. **76**, 801 (1979).

22. H. E. Savage, New York Eye and Ear Infirmary, personal communication.

23. J. J. Salley, J. D. Res. 33(2), 253 (1954).

24. H. E. Savage, New York Eye and Ear Infirmary, personal communication.

Yici Guo, Howard E. Savage, Feng Liu, Stimson P. Schantz, P. P. Ho, and R. R. Alfano, submitted to Cancer Research.

Chapter 6

1. Hardware Reference Manuel, Photometrics Ltd., 3440 East Britannnia Drive, Tucson, Arizona (1990).
2. E. L. Dereniak and D. Crowe, "*Optical Radiation Detectors*", John Wiley and Sons, New York (1984).
3. Yici Guo, P. P. Ho, H. Savage, D. Harris, P. Sacks, S. Shantz, F. Liu, N. Zhadin, and R. R. Alfano, Opt. Lett. **22**, 1323 (1997).
4. R. Cubeddu, A. Pifferi, P. Taroni, G. Valentin, and G. Canti, Opt. Lett. 20, 2553 (1995).
5. Q. Z. Wang, Yici Guo, R. Zuzolo, P. P. Ho, and R. R. Alfano, to be submitted to Opt. Lett.

Chapter 7

1. W. Denk, J. H. Strickler, and W. W. Webb, Science **248**, 73 (1990).
2. W. Denk, Soc. Neurosci. Abstr. **19**, 91 (1993).
3. M. Gu and C. J. R. Sheppard, J. of Microsc. 177, 128 (1994).
4. I. Gryczynski, H. Malak, and J. R. Lakowicz, Biospectroscopy **2**, 9 (1996).
5. H. Szmacinski, I. Gryczynski, and J. R. Lakowicz, Biophys, J. 70, 547 (1996).

6. D. L. Wokosin, V. E. Centonze, J. G. White, S. N. Hird, S. Sepesenwol, G. P. S. Malcolm, G. T. Maker, and A. I. Ferguson, Proc. SPIE **2678**, 38 (1996).

7. C. Xu and W. W. Webb, J. Opt. Soc. Am. B **13**, 481 (1996).

8. D. W. Piston, M. S. Kirby, H. Chen, W. J. Lederer, and W. W. Webb, Appl. Opt. **33**, 662 (1994).

9. R. Yuste and W. Denk, Nature **375**, 682 (1995).

10. D. W. Piston, B. R. Masters, and W. W. Webb, J. of Microsc. **178**, 20 (1995).

11. B. R. Masters, P. T. C. So, and E. Gratton, Biophys. J. **72**, 2405 (1997).

12. S. Maiti, J. B. Shear, R. M. William, W. R. Zipfel, and Watt W. Webb Science **275**, 24 (1997).

13. J. Manni, Biophotonics International, Jan./Feb. Issue, 66 (1996).

14. P. T. So, T. French, W. M. Yu, K. M. Berland, C. Y. Dong, and E. Gratton, "*Fluorescence Imaging Spectroscopy and Microscopy*", Vol. 137, John Wiley & Sons, New York (1996).

15. R. R. Alfano, D. B. Tata, J. Cordero, P. Tomashefsky, F. W. Longo, and M. A. Alfano, IEEE J. Quant. Electron. QE-20, 1507 (1984).

16. R. R. Alfano, G. C. Tang, A. Pradhan, W. Lam, D. C. Choy, and E. Opher, IEEE J. Quant. Electron. QE-23, 1806 (1987).

17. R. R. Alfano, B. B. Das, J. B. Cleary, R. Prudente, and E. Celmer, Bull. New York Acad. Med., 2nd Series **67**, 143 (1991).

18. J. R. Lakowicz and I. Gryczynski, Biophys. Chem. **45**, 1 (1992).

19. J. R. Lackowicz, I. Gryczynski, E. Danielsen, and J. Frisoli, Chem. Phys. Lett. **194**, 282 (1992).

20. J. A. B. Ross, H. R. Wyssbrod, R. A. Porter, G. P. Schwartz, C. A. Michaels, and W. R. Laws, Biochem. **31**, 1585 (1992).

21. Ji Ji Cheng, *"Photo-biology Physics"*, Chinese Academic Publisher, Beijing (1987).

22. Yici Guo, Q. Z. Wang, N. Zhadin, Feng Liu, S. G. Demos, D. Calistru, A. Tirksliunas, A. Katz, Y. Budansky, P. P. Ho, and R. R. Alfano, Appl. Opt. **36**, 968 (1997).

Chapter 8

1. C. Xu and W. Denk, Appl. Phys. Lett. **71**, 2578 (1997).

2. H. Komoda and K. Shimizu, Jpn. J. Appl. Phys. **33**, 3393 (1994).

3. B. P. Richards and P. K. Footner, *"The role of Microscopy in Semiconductor Failure Analysis"*, Oxford University Press, New York (1992).

4. S. Nakamura, Photonics Spectra, May Issue, 130 (1998).

5. S. Nakamura and G. Fasol, *"The Blue Laser Diode"*, Springer-Verlag, New York (1997).

IMAGE EVALUATION TEST TARGET (QA-3)

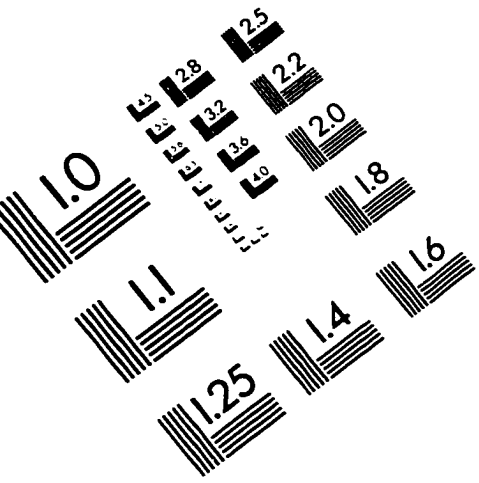

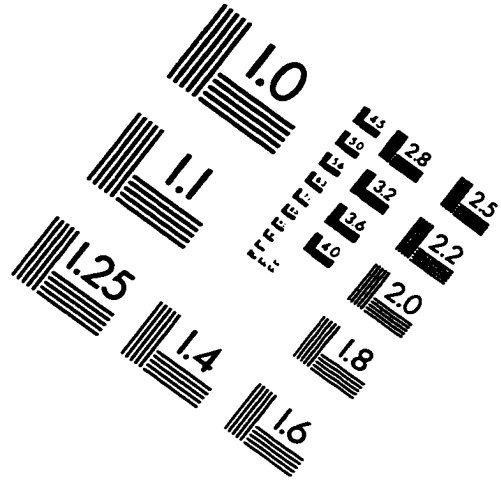

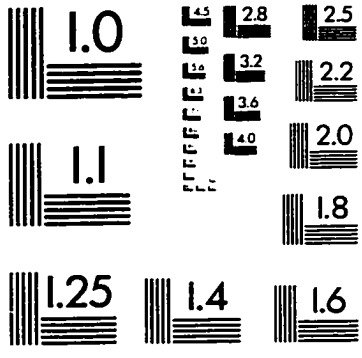

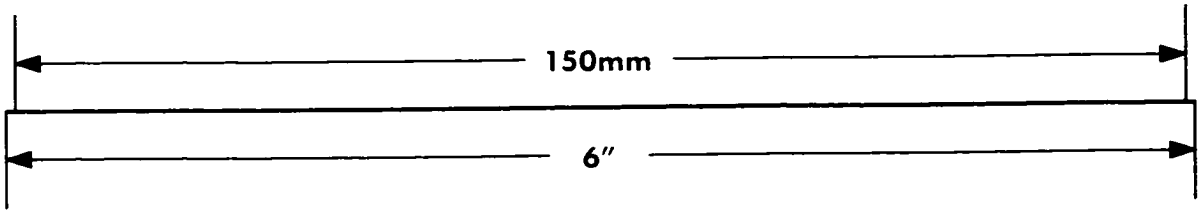

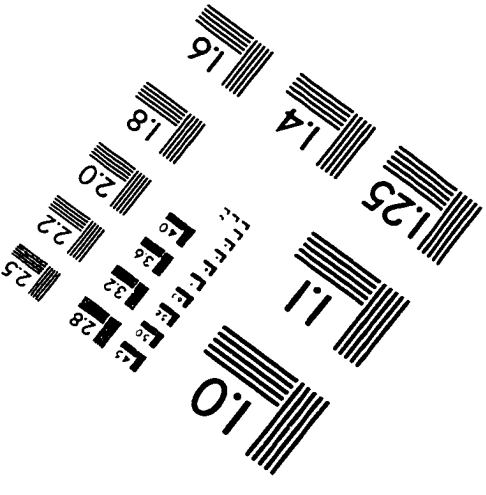

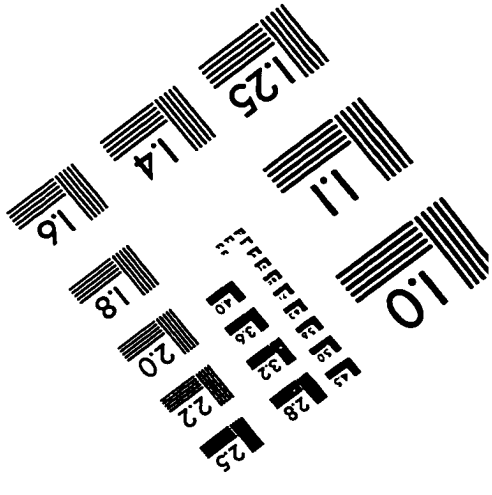

APPLIED IMAGE, Inc
1653 East Main Street
Rochester, NY 14609 USA
Phone: 716/482-0300
Fax: 716/288-5989